UNIVERSITA' DEGLI STUDI DI PADOVA

Sede Amministrativa: Università degli Studi di Padova

Centro Interdipartimentale di Studi e Attività Spaziali "G. Colombo" (CISAS)

Scuola di Dottorato di Ricerca in: SCIENZE TECNOLOGIE E MISURE SPAZIALI

Indirizzo: ASTRONAUTICA E SCIENZE DA SATELLITE

Ciclo: XXII

THERMAL EFFECTS REDUCTION TECHNIQUES FOR THE SIMBIO-SYS SCIENTIFIC SUITE OF BEPICOLOMBO MISSION

TECNICHE DI RIDUZIONE DEGLI EFFETTI TERMICI PER LA STRUMENTAZIONE SCIENTIFICA SIMBIO-SYS DELLA MISSIONE BEPICOLOMBO

Direttore della Scuola: Ch.mo Prof. Cesare Barbieri

Coordinatore dell'Indirizzo: Ch.mo Prof. Giampiero Naletto

Supervisori: Ch.mo Prof. Francesco Angrilli, Ch.mo Prof. Stefano Debei

Dottorando : Enrico Friso

Ai miei genitori

Abstract

This thesis work investigates reduction techniques of thermal effects for the SIMBIO-SYS scientific suite of BepiColombo mission. SIMBIO-SYS (Spectrometer and Imagers for MPO BepiColombo-Integrated Observatory SYStem) is an integrated suite of imaging instruments and it has been selected for the ESA BepiColombo mission to Mercury. It includes a stereo imaging system (STC), an high-resolution imager (HRIC) and a visible–near-infrared imaging spectrometer (VIHI). SIMBIO-SYS will have to operate in a very harsh environment, mainly from the thermal point of view. For this reason, state-of-art heat rejection baffles and filters have to be designed. To overcome this issue, a methodological approach has been followed.

Starting from the estimation of thermal environment encountered by the payload during mission led to a deep knowledge of the heat loads that the instrument will face during the BepiColombo mission operational phases and provided a framework to the design of the payload baffling system.

A mathematical model has been developed and simulations has been carried out to evaluate the incident fluxes on the front end of the payload during the orbiting of Mercury Planetary Orbiter (MPO) spacecraft around Mercury. The study allowed to identify the most critical cases from the thermal point of view. Furthermore the mathematical model assess the Sun aspect angle of the optical axes of the three channels (HRIC, VIHI, STC) and identifies the most critical conditions during the various phases of the mission, providing input data for the design of the baffles and constraints for the verification of their geometry. This model could be applied also to other planetary observation scientific missions.

The geometry of the present configuration of SIMBIO-SYS baffles have been verified against direct Sun illumination and dedicated ray-casting algorithms have been implemented to calculate the angular margin to direct entry of solar rays.

Thermal analyses of baffles have been afterwards carried out using lumped parameter thermal network method and implemented in ESARAD/ESATAN software. This allows to predict the main heat transfer mechanisms and temperature distribution and to estimate the performance of baffles in terms of heat rejection capability. A study on the appropriate implementation of the HRIC Stavroudis reflective baffle geometry, to avoid overestimation of absorbed fluxes, allows to effectively model this particular type of baffle; furthermore this study led to the definition of a criterion to evaluate the performance of the Stavroudis and to guide the design of the most appropriate test-bed to be used to evaluate its behaviour.

The lay-out of a Mercury thermal environment simulator facility has been designed on the basis of the studies carried out. The facility is under development at CISAS (University of Padova) an will be used as an experimental set-up for SIMBIO-SYS baffles and instrument thermal testing. It will consist of a thermal vacuum chamber with heating and cooling sources to simulate the thermal environment that the payload will face on orbit.

The design and analysis methods developed had contributed to the definition of an efficient system of thermal reduction effects for the SIMBIO-SYS scientific suite.

Sommario

Il progetto di ricerca della tesi di dottorato si colloca all'interno dello sviluppo e progettazione della strumentazione SIMBIO-SYS a bordo della sonda Mercury Planetary Orbiter (MPO) della missione ESA BepiColombo a Mercurio.

Mercurio è il pianeta con la maggiore variazione diurna di temperatura del sistema solare; le temperature massime della faccia del pianeta illuminata dal Sole variano da un massimo di circa 688K al perielio a 560K all'afelio circa, mentre la temperatura di corpo nero della faccia in ombra è di circa 100K. Data la vicinanza del pianeta al Sole, i flussi termici solari sono molto elevati con valori che variano da 14490 W/m^2 al perielio a 6290 W/m^2 all'afelio. Conseguenza immediata di queste considerazioni preliminari è che il controllo termico, in particolare del carico utile, assume una importanza cruciale. Si vedano a tal proposito la tabella e la figura che seguono.

	Costante solare [W/m^2]	**Temperatura massima sulla superficie di Mercurio [K]**
Perielio	14490	689
Equinozi	9969	627
Afelio	6291	559

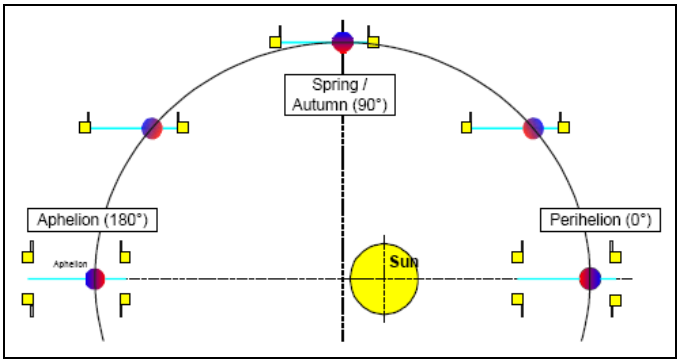

Vista normale al piano dell'orbita di Mercurio attorno al Sole. L'orbita di MPO è normale a tale piano e indicata con un in colore segmento azzuro

SIMBIO-SYS (Spectrometer and Imagers for MPO BepiColombo-Integrated Observatory SYStem) è una suite integrata di strumenti ottici costituita da tre canali: High Resolution Imaging Channel (HRIC), STereo Imaging Channel (STC), Visual and Infrared Hyperspectral Imager (VIHI).

Nell'approcciare il problema, inizialmente si è valutato l'ambiente termico che lo strumento incontrerà durante le fasi operative in orbita attorno a Mercurio. A tal fine è stato sviluppato un modello matematico che valuta i flussi incidenti su una superficie piana infinitesima orbitante attorno al pianeta secondo l'orbita e l'assetto nominali previsti dalla missione BepiColombo per il satellite

MPO. Le superfici considerate per il calcolo sono le normali agli assi ottici dei canali di SIMBIO-SYS: una superficie normale alla direzione di puntamento verso il nadir (canali HRIC e VIHI), le altre due superficie in avanti e indietro sul piano dell'orbita di MPO e nel verso del moto del satellite (canale STC). Si veda a proposito la figura seguente.

L'implementazione del modello matematico in ambiente Matlab ha permesso di valutare l'andamento dei flussi solare, di albedo e di emissione infrarossa provenienti da Mercurio. Nota la posizione di Mercurio rispetto al Sole, viene calcolata la distribuzione delle temperature sulla superficie del pianeta, secondo un modello di corpo nero e, dati i parametri orbitali e di assetto del satellite MPO, il modello calcola i flussi planetario, solare e di albedo incidenti sulla superficie orbitante considerata. Tramite le simulazioni si è ottenuto l'andamento dei flussi termici in funzione della anomalia vera del satellite e dell'anomalia vera del pianeta e ciò ha permesso di stimare l'ambiente termico nel quale lo strumento in volo si troverà ad operare, fornendo inoltre una visione qualitativa generale ed una migliore comprensione dei parametri maggiormente rilevanti dal punto di vista termico. I risultati ottenuti hanno inoltre permesso di individuare le orbite termicamente più critiche da utilizzare per le successive analisi di dettaglio e per i modelli termici dello strumento. ("hot cases" e "cold cases").

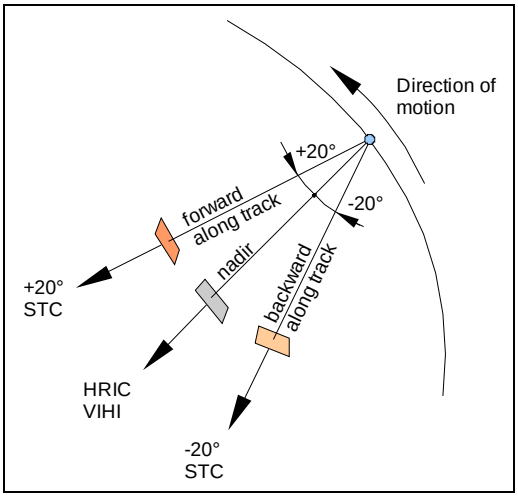

Orientamento in orbita degli assi ottici dei tre canali di SIMBIO-SYS

Oltre al calcolo dei flussi termici incidenti, il modello implementato calcola, per ogni tratto di traiettoria orbitale illuminato dal Sole, l'angolo di incidenza dei raggi solari con la normale alla superficie considerata (ovvero con gli assi ottici dei tre canali dello strumento). Successivamente, per ogni stagione di Mercurio, viene calcolato il valore minimo di tale angolo. Si è così potuto ottenere l'andamento dei valori minimi dell'angolo di incidenza solare in funzione delle stagioni di Mercurio. Questo calcolo è effettuato al fine di verificare che, durante la missione, la geometria dei baffle sia tale da impedire l'ingresso diretto di raggi solari nelle ottiche del telescopio. E'stato inoltre analizzato l'impatto sul valore dell'angolo minimo di incidenza solare, dell'evoluzione dei parametri orbitali durante la missione (dall'approccio al pianeta alla fine della missione estesa).

Le geometrie dei baffle di HRIC, VIHI e STC sono state poi verificate ed è stato valutato il margine angolare che la geometria della attuale configurazione prevista garantisce per evitare l'ingresso di raggi solari durante la missione. In particolare i baffle della stereo camera STC, i cui assi ottici sono inclinati in avanti e indietro di 20° rispetto alla direzione di nadir lungo la traiettoria del satellite attorno a Mercurio, presentano la maggiore criticità all'ingresso diretto di raggi solari in orbita a causa della suddetta vergenza angolare. Inoltre, data l'apertura rettangolare del baffle, la verifica è stata eseguita implementando algoritmi di ray-tracing per valutare il margine angolare.

Sono stati poi sviluppati modelli termici dei baffle utilizzando il software ESARAD/ESATAN. Lo schema utilizzato per i modelli dei baffle è indicato in figura seguente.

Il baffle è inserito all'interno di una cavità nera a temperatura di interfaccia costante, che rappresenta l'ambiente termico radiativo interno del satellite. Un secondo nodo a temperatura costante rappresenta l'interfaccia conduttiva del baffle con il satellite. Nella parte posteriore del baffle è posto un volume di controllo a rappresentare l'unità ottica. Internamente esso è una cavità nera, con foro di apertura corrispondente all'apertura del sistema ottico. Esternamente ha proprietà di multilayer isolante. La temperatura interna della cavità corrisponde alla temperatura media prevista dall'unità ottica per quell'orbita. E' stato possibile ottenere così modelli termici di dettaglio di diverse configurazioni dei baffle e valutare la capacità di reiezione del calore dei baffle attraverso bilanci termici del sottosistema, seguendo lo schema indicato in EID-A . Si è quindi ottenuto l'andamento delle temperature dei baffle e sono state stimate le potenze termiche scambiate dai baffle con le interfacce termiche del satellite.

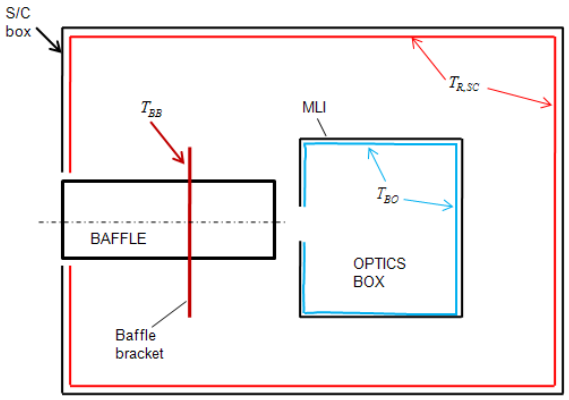

Schema utilizzato per la modellazione termica dei baffle

La camera ad alta risoluzione HRIC, a causa della maggiore apertura, è il canale sottoposto alla maggiore potenza termica proveniente dall'ambiente esterno. La configurazione prevista dal team di progetto dello strumento prevede l'uso di un baffle di tipo Stavroudis. La geometria di questo tipo di baffle riflettente consiste in una serie di ellissoidi ed iperboloidi aventi fuochi comuni e tali da riflettere, nel caso ideale, tutta la radiazione incidente esternamente al cono di "cut-off" del baffle stesso. Il comportamento termo-ottico di questo tipo di baffle riflettente dipende in modo sostanziale dalla sua peculiare geometria: è quindi necessaria una corretta modellazione della stessa per il calcolo dei fattori di vista e dei flussi assorbiti dai nodi termici del baffle. L'analisi dello scambio termico radiativo viene eseguito tramite il metodo Monte Carlo Ray Tracing, utilizzando il software commerciale ESARAD il quale tuttavia, come pure altri software di analisi termica attualmente disponibili, non consente l'implementazione in forma analitica delle superfici quadriche costituenti la peculiare geometria del baffle Stavroudis. Si è resa necessaria così una modellazione della geometria con forme elementari approssimanti che fossero il più possibile equivalenti dal punto di vista del comportamento termo-ottico del dispositivo e tali da evitare, in particolare, una eccessiva sovrastima dei flussi assorbiti ai nodi del baffle Stavroudis. Sono state confrontate diverse modalità di rappresentazione geometrica del baffle fino ad ottenere quella ottimale sia dal punto di vista della accuratezza del modello che dal punto di vista del costo computazionale.

I risultati delle simulazioni termiche mostrano che la configurazione attuale prevista per il baffle Stavroudis (HRIC) permette una reiezione fino al 90% del totale flusso di calore proveniente dall'ambiente esterno in orbita (solare, infrarosso planetario e di albedo).

L'attività è proseguita con il dimensionamento a livello preliminare di sistema, di un apparato sperimentale finalizzato a riprodurre a terra l'ambiente termico incontrato dallo strumento orbitante attorno a Mercurio. Tale apparato sperimentale è stato concepito per riprodurre all'interno di una camera termo-vuoto l'andamento durante l'orbita dei flussi solare e infrarosso incidenti sullo

strumento e le interfacce radiative e conduttive con il satellite, tenendo conto anche della relativa orientazione durante il moto orbitale, degli assi ottici dei tre canali rispetto alle sorgenti di radiazione. Tale apparato sperimentale consiste in un simulatore solare, con relativo sistema ottico, in grado di riprodurre la potenza radiante su Mercurio, pari a circa dieci volte la costante solare terrestre. Inoltre all'interno della camera saranno poste delle piastre riscaldanti controllate termicamente e tali da generare la sorgente di radiazione infrarossa proveniente dalla superficie di Mercurio.

I modelli matematici sviluppati e le analisi eseguite sono state utilizzate per definire le specifiche di progetto dell'apparato sperimentale ed hanno fornito dati numerici utili alla definizione del simulatore a livello di sistema.

Le attività future prevedono la caratterizzazione e calibrazione delle sorgenti di radiazione dell'apparato sperimentale, in particolare del simulatore solare, sia in termini di irradiazione totale, sia di distribuzione spettrale con metodi radiometrici. La attività sperimentale consisterà nel riprodurre le condizioni operative su prototipi termici e strutturali (STM) dei baffles ed è finalizzata in particolare alla validazione sperimentale dei modelli numerici sviluppati.

Table of contents

1 INTRODUCTION

This thesis work is related with the design activities of SIMBIO-SYS scientific suite on board the Mercury Planetary Orbiter (MPO) of the ESA mission BepiColombo.
Mercury, due to his 3/2 spin-orbit resonance, presents a very high temperature variation between the sun lighted and the dark side of the planet .
The maximum temperature on the sunlit side of the planet could reach 700 K at perihelion, whereas the dark side temperature has values of around 100 K. Furthermore, due to the proximity to the Sun, the solar fluxes are very high and could reach the value of 14000 W/m2 at perihelion. It follows that the thermal control design is a crucial activity within the development of the payload.
This thesis work would investigate possible reduction techniques of thermal effects for the SIMBIO-SYS scientific suite of BepiColombo mission.
SIMBIO-SYS (Spectrometer and Imagers for MPO BepiColombo-Integrated Observatory SYStem) is an integrated suite of imaging instruments and it has been selected for the ESA BepiColombo mission to Mercury, which includes a stereo imaging system (STC), an high-resolution imager (HRIC) and a visible–near-infrared imaging spectrometer (VIHI). A brief introduction and description of the instrument will be given in the next chapter. SIMBIO-SYS will have to operate in a very harsh environment, mainly from the thermal point of view and the presence of high- energy particles. For this reason, state-of-art heat rejection baffles and filters have to be designed ad hoc, produced and integrated; their qualification implies sophisticated test beds to reproduce environmental parameters such as solar and IR fluxes

In the first part of the thesis, ***Chapter 3***, it will be investigated the thermal environment encountered by the payload during mission in order to have a deep knowledge of the heat loads that the instrument will face during flight. A mathematical model is presented to evaluate the incident fluxes coming from the environment during orbiting of MPO spacecraft around Mercury. Planetary infrared, albedo and solar incident flux will be evaluated for all the possible orbits during mission and the most critical cases will be singled out.

In the frame of the developments for the BepiColombo mission, the design of baffle with high rejection performance is a demanding task. This thesis work will focus in particular on the design of efficient baffling for the SIMBIO-SYS instrumentation.
A baffle has the function to protect the entrance of the front optics of an instrument from direct light illumination (mostly from the Sun) reaching it from outside at a specified aspect angle with regard to the optical axis. The subsequent ***Chapter 4*** of the thesis will assess the Sun incidence angle during mission in order to provide design constraints for baffle dimensioning. In fact, given the very high values of solar irradiance, a direct Sun illumination of the detector would seriously compromise the overall experiment.
The geometry of the baffle of the three channel will be verified to Sun illumination and dedicated ray-casting algorithms will be implemented to verify the baffles of STC channel, which is the most critical since this channel have rectangular aperture baffles and it will point off-nadir, then the optical axes will see the Sun with a narrower aspect angle. These analysis will be presented in ***Chapter 5***.

Thermal analyses and models have been performed using ESARAD/ESATAN software to evaluate heat transfer paths and temperature distribution of the instrument orbiting Mercury. Analysis cases has been selected on the basis of the previously evaluation and knowledge of thermal environment. The analyses and simulations presented in the thesis focus on the thermal models of the baffle sub-system and are the topics of the ***Chapter 6***. In this thesis, thermal models of the current

configuration is presented. It must be underlined that the configuration herein analyzed and reported could be subjected to variation and modification in the future since the design process in ongoing. Data and results herein presented should not be taken as official of the BepiColombo mission.

A study on the implementation on ESARAD software of the HRIC Stavroudis baffle and a method for appropriate modeling this kind of geometry is presented. This study lead to the definition of a criterion to evaluate the performance of this type of baffles and to guide the design of the most appropriate test-bed to be used to evaluate its behaviour.

The last ***Chapter 7*** of the thesis describes an experimental set-up for SIMBIO-SYS instrument thermal testing under development at CISAS (University of Padova). It will consist of a thermal vacuum chamber with heating and cooling sources to simulate the thermal environment that the payload will face on orbit. The lay-out of the test bed has been conceived on the basis of the study performed and described in this thesis work. The facility will be used to thermal testing the STM and QM models of SIMBIO-SYS baffles. Activities foreseen in the next future are the characterization and calibration of the radiative heat sources of the facility and the validation of thermal mathematical models through experimental data.

2 MISSION AND INSTRUMENT DESCRIPTION

In the framework of the science programme of the European Space agency (ESA) , BepiColombo is an ESA mission [1] in cooperation with Japan, that will explore Mercury, the planet closest to the Sun. This mission is one of the 'cornerstones' in ESA's long-term science programme. Europe's space scientists have identified the mission as one of the most challenging long-term planetary projects, because Mercury's proximity to the Sun makes it difficult for a spacecraft to reach and survive in the harsh environment. The scientific interest to go to Mercury lies in the valuable clues that such a mission can provide in understanding the planet itself as well as the formation of our Solar System; clues which cannot be obtained with distant observations from Earth.

The first probe has visited Mercury was NASA's Mariner 10 which flew past three times in 1974-5 and returned the first close-up images of the planet. Recently, on January 14, 2008, more than three decades after the third Mariner 10 flyby, NASA's MESSENGER passed 200 kilometers above Mercury's surface. On September 29, 2009, the MESSENGER spacecraft passed by Mercury for the third time, flying 141.7 miles above the planet's rocky surface for a final gravity assist that will enable it to enter orbit about Mercury in 2011.

BepiColombo ESA mission is named after Prof. Giuseppe (Bepi) Colombo (1920-1984) a mathematician professor at the engineering faculty of the University of Padua. He was the first to see that an unsuspected resonance is responsible for Mercury's habit of rotating on its axis three times for every two revolutions it makes around the Sun. He also suggested to NASA how to use a gravity-assist swing-by of Venus to place the Mariner 10 spacecraft in a solar orbit that would allow it to fly by Mercury three times in 1974-5.

The information gleaned when BepiColombo arrives will throw light not only on the composition and history of Mercury, but also on the history and formation of the inner planets in general, including the Earth. Mercury is an extreme of our planetary system. It is the closest planet to the Sun and has the highest uncompressed density of all planets. Solar tides have influenced its rotational state. Its surface has been altered during the initial cooling phase and its chemical composition may have been modified by bombardment in its early history. Mercury therefore plays an important role in constraining and testing dynamical and compositional theories of planetary formation.

The main scientific objectives of the mission are:

- Origin and evolution of a planet close to the parent star
- Mercury as a planet: form, interior structure, geology, composition and craters
- Mercury's vestigial atmosphere (exosphere): composition and dynamics
- Mercury's magnetized envelope (magnetosphere): structure and dynamics
- Origin of Mercury's magnetic field
- Polar deposits: composition and origin
- Test of Einstein's theory of general relativity

BepiColombo will set off in 2014 on a journey lasting approximately 6 years. When it arrives at Mercury in mid 2020, it will endure temperatures as high as 350 °C and gather data during its 1 year nominal mission, with a possible 2-year extension.

The mission will consist of two separate spacecraft that will orbit the planet. ESA is building one of the main spacecraft, the Mercury Planetary Orbiter (MPO), and the Japanese space agency ISAS/JAXA will contribute the other, the Mercury Magnetospheric Orbiter (MMO).

The MPO will study the surface and internal composition of the planet, and the MMO will study Mercury's magnetosphere, the region of space around the planet that is dominated by its magnetic field.

Figure 2.1: Artist's impression of the Mercury Planetary Orbiter (MPO), that will be placed in a dedicated orbit around Mercury (image ESA Copyright [1])

An integrated suite of instruments, Spectrometer and Imagers for MPO BepiColombo-Integrated Observatory SYStem (**SIMBIO-SYS**), has been selected for the ESA BepiColombo mission to Mercury, which includes a stereo imaging system (STC), an high-resolution imager (HRIC) and a visible–near-infrared imaging spectrometer (VIHI). SIMBIO-SYS will scan the Mercury surface with the three channels and map the physical, morphological, tectonic and compositional properties of the entire planet. The availability of high-resolution images will unveil details of specific target.

The SIMBIO-SYS instrument architecture is based on three different channels Figure 2.2, with a common Main Electronics (ME) and power supply. The three channels form an Instrument Front End (IFE) as shown in Figure 2.3. Each channel is formed by its own optics, detector, thermal hardware, proximity electronics and electrical interface for power supply. The measurement strategy is based on the coordinated operations of the three channels forming SIMBIO-SYS. This has to be optimized in order to maximize the scientific return in each phase of the mission by suitably sharing the available resources in terms of power and data rate. A description of SIMBIO-SYS instrument, its main scientific objectives and performances along with technical characteristics are described in [2].

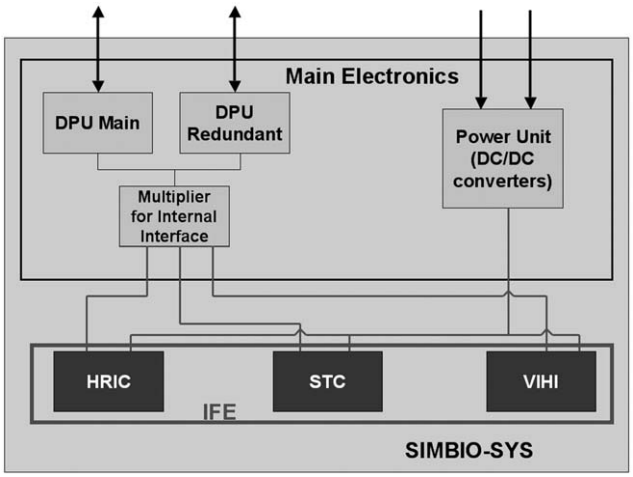

Figure 2.2: Overall scheme of the SIMBIO-SYS suite architecture showing the main sub- systems. IFE: instrument front end; DPU: digital processing unit

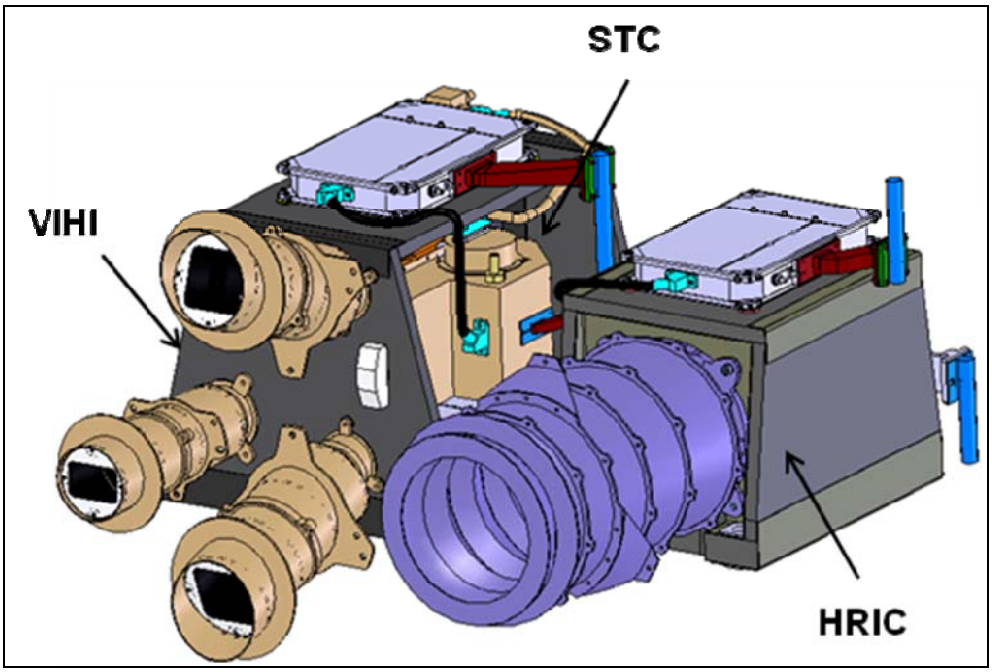

Figure 2.3: *Overall view of the SIMBIO-SYS instrument design. HRIC: high-resolution channel; STC: stereo channel; VIHI: hyperspectral vis–NIR channel.*

At present, SIMBIO-SYS is formed by :

- Main Electronics to be integrated on S/C
- HRIC to be integrated on the S/C Optical Bench; the unit hosts on the top surface its own Proximity Electronics. On its front surface the Thermal Infrared Rejection Device is hosted (see Figure 2.4)
- HRIC TIRS; HRIC Thermal Infrared Rejection System, a Stavroudis baffle (see Figure 2.4)
- STC+VIHI to be integrated on the S/C Optical Bench (see Figure 2.5, Figure 2.6)
- Two STC baffles (see Figure 2.5)
- VIHI baffle (see Figure 2.6)

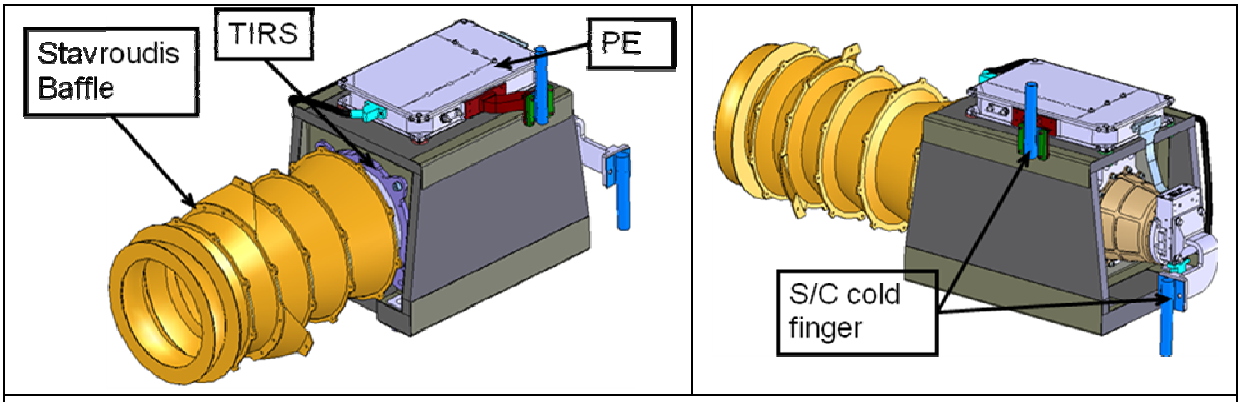

Figure 2.4: HRIC HIgh Resolution Camera

HRIC is based on a catadioptric Ritchey-Chretien configuration equipped with a dedicated refractive corrector camera. The camera is nadir looking and the field of view is of 1.47°.

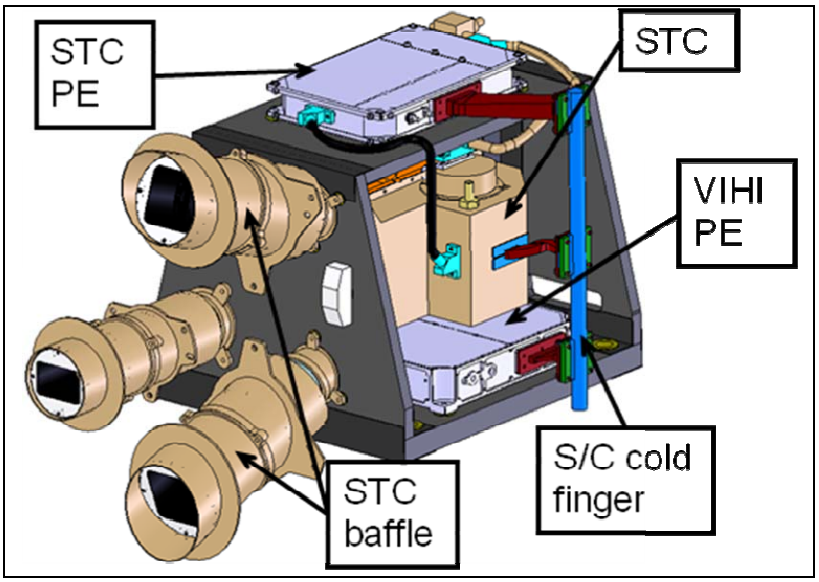

Figure 2.5: STC Stereo Camera

STC: it is composed by two channels with the orientation of +20° and -20° from nadir, adopting an original catadioptric optical design. The FoV is 5.3˚x 4.5˚ cross and along track respectively, and it works in the spectral range of 410-930 nm. The detector is the same of HRIC

VIHI: its optical design has been optimised for the wavelength band from 400 nm up to 2000 nm, its detector is constituted by a HgCdTe hybrid array.

SIMBIO-SYS will have to operate in a very harsh environment, mainly from the thermal point of view and the presence of high- energy particles. For this reason, state-of-art heat rejection baffles and filters have to be designed ad hoc, produced and integrated; their qualification implies sophisticated test beds to reproduce environmental parameters such as solar and IR fluxes.

STC and HRIC are able to perform their observations with detector sensitive area at room temperature, while requiring colder temperatures for calibration purposes. VIHI detector sensitive area is requested to be at about 223K to operate properly. To get the detector sensitive area temperature an active thermal control system has been foreseen: TEC elements are present in each camera detector. The thermal flux is removed from the cold finger provided by S/C.

The HRIC Stavroudis, VIHI and STC baffles will be conductively decoupled from the cameras and conductively coupled to the satellite bracket

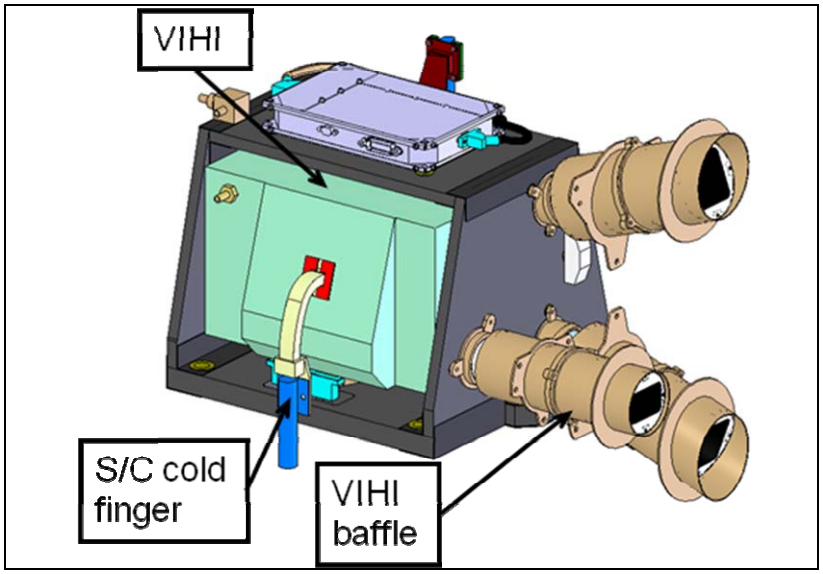

Figure 2.6

In the following figures the main dimensions of present configuration has been presented

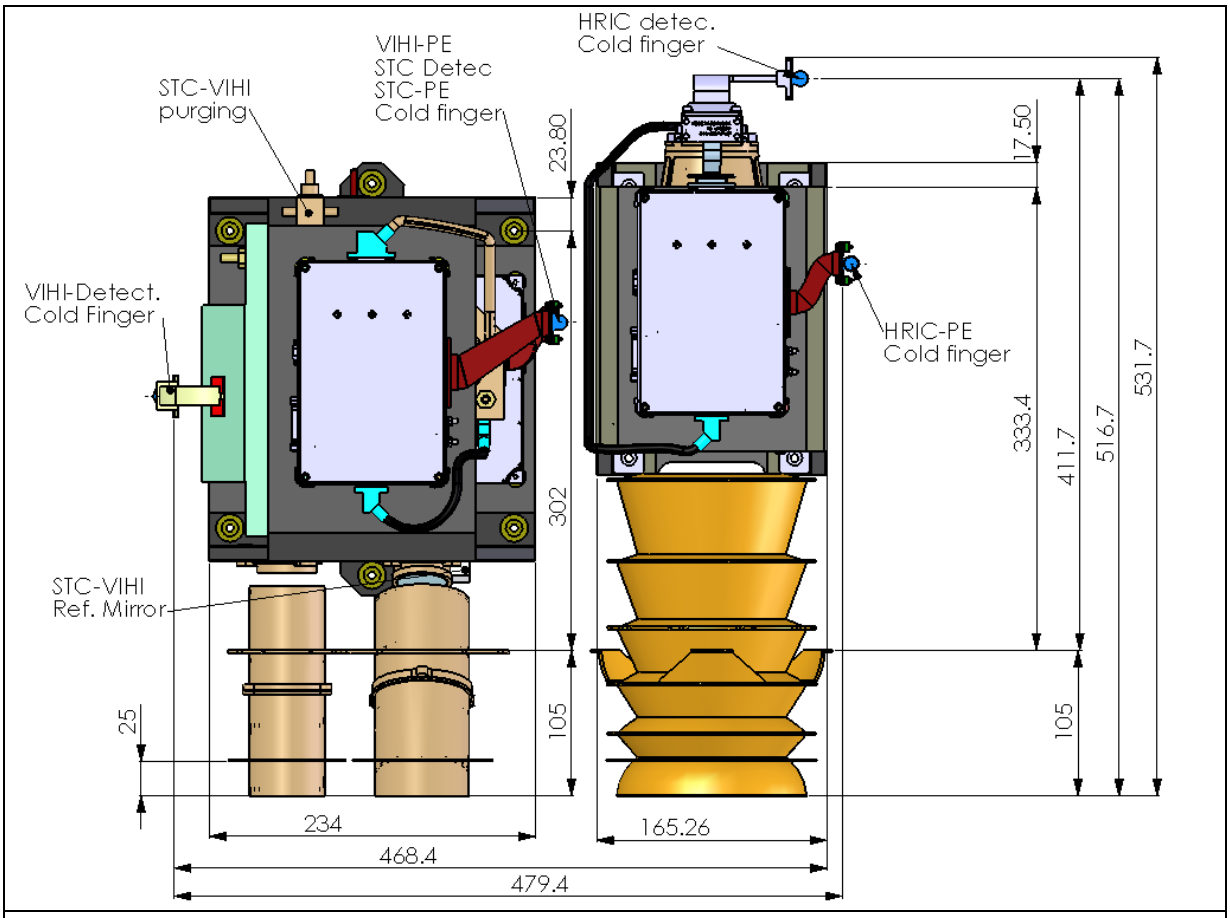

Figure 2.7: Simbio-Sys Main dimensions (upper view)

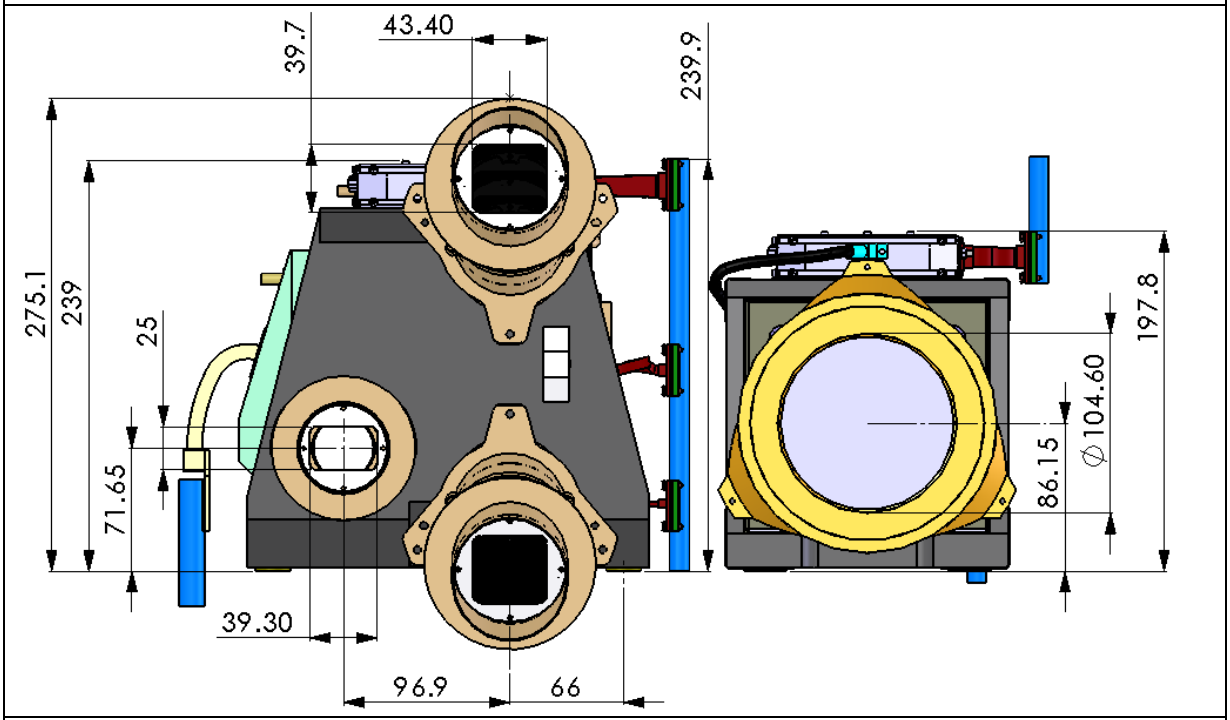

Figure 2.8: Simbio-Sys Main dimensions (front view)

3 MERCURY ORBITAL THERMAL ENVIRONMENT EVALUATION

3.1 Introduction and purpose

A mathematical model has been developed to evaluate the solar, albedo and IR planetary heat fluxes incident on a unitary surface grazing the entrance of the telescope. To get the actual incident irradiation seen by an experiment, a geometrical model has been developed, which can simulate the pointing in the orbit and the kinematics of the spacecraft.
The mathematical model herein developed is similar, in the approach, to that presented in [5], with some improvements. A reference frame, rigid with the spacecraft, has been added, allowing to analyze the effects of a variation of the attitude angles from the nominal condition of a nadir pointing spacecraft.
Furthermore, compared with [5], some improvements has been made on the computation of the eclipse terminator points: the model computes the eclipse terminator points and surface shadowing transition points independently by the number of time instants considered along the orbit. The effects of this on solar fluxes estimation has been also evaluated.
The program calculate also the Sun incidence angle on the surface, defined as the angle between the normal to the considered surface and the Sun rays direction. It is taken into account possible shadowing effects due to the planet or to the surface itself.
The amount of solar flux incoming the surface when parallel to the Sun directions is not taken into account in this model and the hypothesis of parallel Sun rays has been made.
The IR fluxes has been computed by numerical method. The planetary surface has been divided into a grid of parallel and meridian bands and the temperature distribution on the surface of the planet is automatically computed by considering the position of Mercury with respect to the Sun, using the simplified black-body model indicated in [4] and [7].
The albedo fluxes has also been calculated by numerical method, using the same grid on Mercury surface introduced for IR fluxes computation.
The mathematical model have been implemented in Matlab software and some simulations has been performed.
The orbiting surface considered for the simulations are the surfaces normal to the optical axes of the SIMBIO-SYS channels. These are: a surface normal pointing toward nadir, which corresponds to HRIC and VIHI channels, a surface normal pointing +20° forward along track (which corresponds to the axis of one of the eye of STC), a surface normal pointing -20° backward along track (which corresponds to the axis of the other eye of STC). The values of orbital parameters and physical data are taken from [1], [4], [7] .

The purpose of these simulations is to give an overview of the thermal environment encountered by the experiment and to show the most critical thermal cases. The results about minimum Sun incidence angle shall provide design constraints, for example, for the instrument baffles. The model should provide data useful for the design of a Mercury thermal environment simulator hardware. The model could also be used to perform subsequent sensitivity analyses of incident heat fluxes to spacecraft orbital parameters, spacecraft attitude angles, physical constants and planetary temperature distribution.

3.2 Description of the mathematical model

3.2.1 Definition of reference frames

In this chapter the reference frames used in the mathematical model will be defined and illustrated.

– **RF (0) : perifocal r. f.**
B orbit at A
inertial reference frame
origin @ Sun center
x_0 = from Sun to Mercury, at periherm
y_0 = on Mercury orbital plane
z_0 = orthogonal to Mercury's orbital plane

with:
ν_M = true anomaly of Mercury

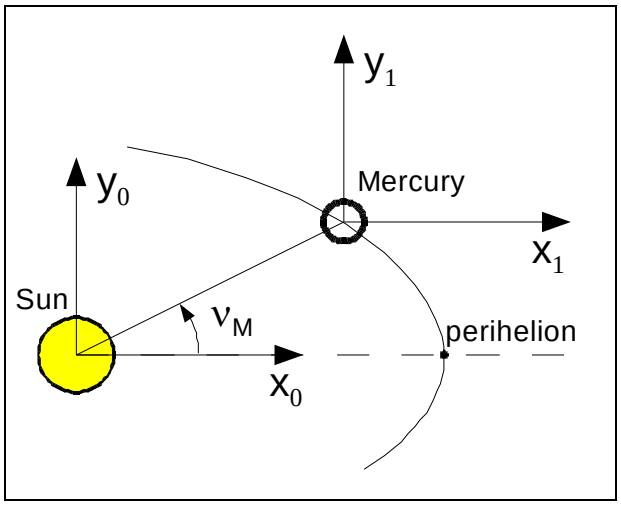

Figure 3.1

– **RF (1) : inertial, planet centered r. f.**
origin @ Mercury center
x_1 = from Sun to Mercury at perihelion
y_1 = on Mercury orbital plane
z_1 = orthogonal to Mercury's orbital plane

– **RF (2): perifocal r.f.**
S/C orbit at B
inertial reference frame
origin @ Mercury center
x_2 = from Mercury to periherm
y_2 = on S/C orbital plane
z_2 = orthogonal to S/C orbital plane
with:
Ω = Right Ascension of the Ascending Node (Sun-Mercury-Ascending Node)
i_0 = inclination of S/C orbit
ω_p = argument of periherm
ν = true anomaly of S/C

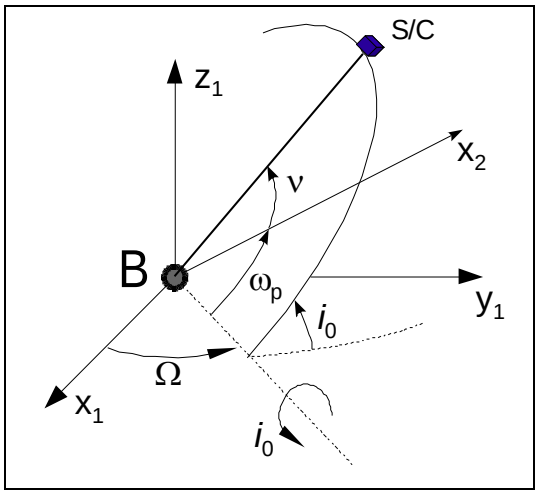

Figure 3.2

– **RF (3)- RPY r.f.**
(Roll Pitch Yaw) orbital r.f.
origin @ S/C
x_3 = lies on orbital plane, toward motion of S/C
y_3 = orthogonal to S/C's orbital plane
z_3 = nadir pointing

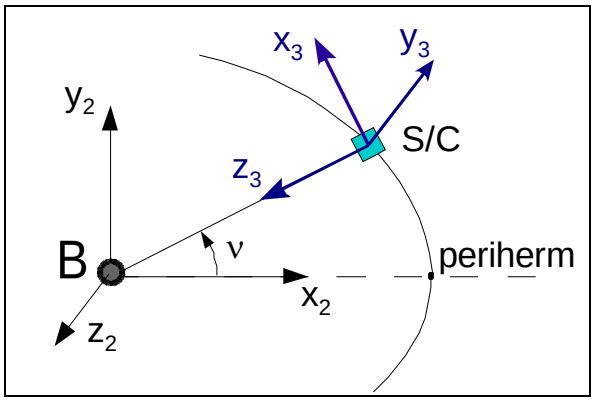

Figure 3.3

- **RF (4)- BODY fixed reference frame**
  origin @ S/C
  x_4 = toward motion of S/C (*roll* ϕ)
  y_4 = complete r.f. (*pitch* θ)
  z_4 = toward planet (*yaw* ψ)
  (see [9])

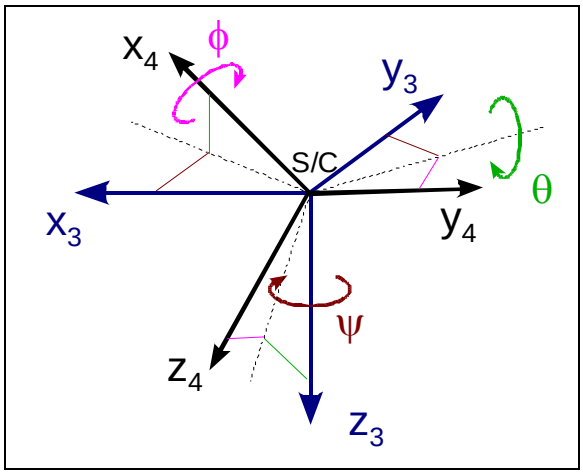

Figure 3.4

- **RF (sun)- Sun vector r.f.**
  origin @ Mercury center
  x_{sun} = toward Sun
  Ωs = Sun longitude
  δs = Sun declination

- **RF (5)- Planetary temperature r.f.**
  heliotropic
  origin @ Mercury center
  z_5 = toward Sun (T_{max})
  other axes such that:
  $x_5 = y_{sun}$
  $y_5 = z_{sun}$
  $z_5 = x_{sun}$

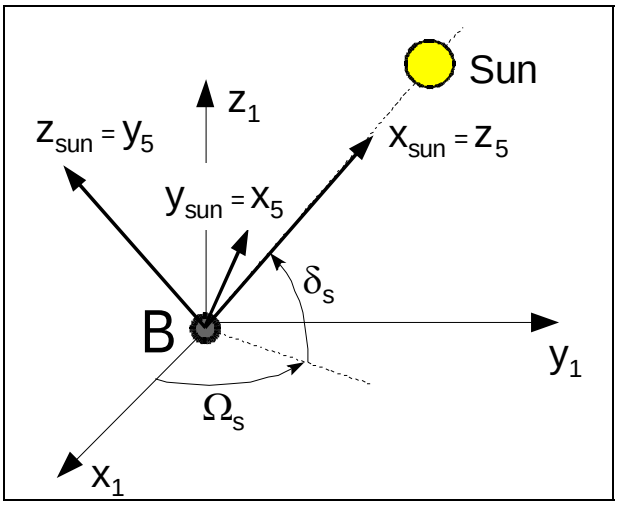

Figure 3.5

Reference frame **RF(0)** is the inertial reference frame, centered at the Sun; this is the perifocal reference frame of Mercury orbit around the Sun and will be used to calculate Mercury position with respect to Sun. The angle ν_M is the true anomaly of Mercury orbit.

Reference frame **RF(1)** has origin at Mercury and has axes parallel to RF(0), then the transformation matrix from RF(0) to RF(1) is the identity matrix.

Reference frame **RF(2)** has origin at Mercury and is the perifocal reference frame of S/C orbit around Mercury planet. It will be used to compute the position of the spacecraft in respect of Mercury. The orientation of RF(2) defines the orientation of the S/C orbital plane by using the angles Ω, i_0, ω_p. The Right Ascension of the Ascending Node Ω is calculated taking as reference axis the direction from Sun to Mercury, with Mercury at perihelion (i.e. X_1 axis, see Figure 3.1, Figure 3.2). The angle i_0 is the inclination of spacecraft orbit; the angle ω_p is the argument of periherm. The angle ν is the true anomaly of S/C orbit around the planet.

Reference frame **RF(3)** is the RPY reference frame [9], having Z and X axes lying on S/C orbital plane, Z nadir pointing (see Figure 3.3). It is related on the one hand to perifocal RF(2) by true anomaly ν and on the other hand to body fixed RF(4) by yaw, pitch and roll angles .
It must be pointed out that, if the attitude of the spacecraft would be perfectly nadir pointing, the RF(3) coincide with RF(4).

Reference frame **RF(4)** is the body fixed reference frame, rigid with spacecraft. It is related to RF(3) by yaw (ψ), pitch (θ) and roll (ϕ) angles. If the S/C is nadir pointing, the corresponding yaw, pitch and roll angles are all equal to zero; the angles ψ, θ, ϕ are to be intended as deviation from nominal attitude nadir pointing condition (see Figure 3.4).

The coordinates of the versor $\mathbf{n}_T$ normal to the surface considered are known in RF(4), being the spacecraft fixed reference frame.

It must be noticed that the introduction of RF(4) allows to analyze the effects of a variation of the attitude angles from the nominal condition of nadir pointing spacecraft.

Reference frame **RF(sun)** has origin at Mercury and its X axis is always pointing toward the Sun (Figure 3.5). It is related to RF(1) by Sun longitude Ω_s and by Sun declination δ_s. These two angles can be expressed as functions of Mercury true anomaly ν_M (see equations (23)).

Reference frame **RF(5)** is the reference frame fixed with planetary temperature distribution; it has Z axis toward maximum planetary temperature (i.e. toward the Sun). The RF(5) is used to easily express the temperature distribution on planetary surface as function of grid spherical coordinates ξ_k and η_k (see Figure 3.6).

All vectors will be projected in this reference frame to calculate the expression of IR, albedo and solar fluxes.

3.2.2 Transformation matrices between reference frames:

In the following are calculated and reported the transformation matrices that will be used in the mathematical model. **RF(i)** stands for " i-th Reference Frame".

From RF (1) to RF (2)

$$\begin{bmatrix} x_1 \\ y_1 \\ z_1 \end{bmatrix} = \begin{bmatrix} \cos\Omega & -\sin\Omega & 0 \\ \sin\Omega & \cos\Omega & 0 \\ 0 & 0 & 1 \end{bmatrix} \begin{bmatrix} 1 & 0 & 0 \\ 0 & \cos i_0 & -\sin i_0 \\ 0 & \sin i_0 & \cos i_0 \end{bmatrix} \begin{bmatrix} \cos\omega_p & -\sin\omega_p & 0 \\ \sin\omega_p & \cos\omega_p & 0 \\ 0 & 0 & 1 \end{bmatrix} \begin{bmatrix} x_2 \\ y_2 \\ z_2 \end{bmatrix} \tag{1}$$

$$\mathbf{X}^{(1)} = \mathbf{R}(\Omega)\mathbf{R}(i_0)\mathbf{R}(\omega_p)\mathbf{X}^{(2)} = \mathbf{R}_2^1\mathbf{X}^{(2)} \tag{2}$$

From RF (2) to RF (3)

$$\mathbf{X}^{(2)} = \mathbf{R}_3^2\mathbf{X}^{(3)} \tag{3}$$

$$\mathbf{R}_3^2 = \begin{bmatrix} \cos\nu & -\sin\nu & 0 \\ \sin\nu & \cos\nu & 0 \\ 0 & 0 & 1 \end{bmatrix} \begin{bmatrix} 1 & 0 & 0 \\ 0 & 0 & 1 \\ 0 & -1 & 0 \end{bmatrix} \begin{bmatrix} 0 & 0 & -1 \\ 0 & 1 & 0 \\ 1 & 0 & 0 \end{bmatrix} = \begin{bmatrix} -\sin\nu & 0 & -\cos\nu \\ \cos\nu & 0 & -\sin\nu \\ 0 & -1 & 0 \end{bmatrix} \tag{4}$$

From RF (3) to RF (4)

sequence: Euler 3-2-1

3 – yaw ψ

$$\mathbf{R}(\psi) = \begin{bmatrix} \cos\psi & -\sin\psi & 0 \\ \sin\psi & \cos\psi & 0 \\ 0 & 0 & 1 \end{bmatrix} \tag{5}$$

2 – pitch θ

$$\mathbf{R}(\theta) = \begin{bmatrix} \cos\theta & 0 & \sin\theta \\ 0 & 1 & 0 \\ -\sin\theta & 0 & \cos\theta \end{bmatrix} \tag{6}$$

1 – roll ϕ

$$\mathbf{R}(\phi)=\begin{bmatrix}1 & 0 & 0\\ 0 & \cos\phi & -\sin\phi\\ 0 & \sin\phi & \cos\phi\end{bmatrix} \tag{7}$$

$$\mathbf{X}^{(3)}=\mathbf{R}(\psi)\mathbf{R}(\theta)\mathbf{R}(\phi)=\mathbf{R}_4^3\mathbf{X}^{(4)} \tag{8}$$

$$\mathbf{R}_4^3=\begin{bmatrix}\cos\psi\cos\theta & \cos\psi\sin\theta\sin\phi-\sin\psi\cos\phi & \cos\psi\sin\theta\cos\phi+\sin\psi\sin\phi\\ \sin\psi\cos\theta & \sin\psi\sin\theta\sin\phi+\cos\psi\cos\phi & \sin\psi\sin\theta\cos\phi-\cos\psi\sin\phi\\ -\sin\theta & \cos\theta\sin\phi & \cos\theta\cos\phi\end{bmatrix} \tag{9}$$

From RF (5) to RF (1)

$$\mathbf{X}^{(1)}=\mathbf{R}_{sun}^1\mathbf{X}^{(sun)} \tag{10}$$

$$\begin{aligned}\mathbf{R}_{sun}^1&=\begin{bmatrix}\cos\Omega_s & -\sin\Omega_s & 0\\ \sin\Omega_s & \cos\Omega_s & 0\\ 0 & 0 & 1\end{bmatrix}\begin{bmatrix}\cos\delta_s & 0 & -\sin\delta_s\\ 0 & 1 & 0\\ \sin\delta_s & 0 & \cos\delta_s\end{bmatrix}\\ &=\begin{bmatrix}\cos\Omega_s\cos\delta_s & -\sin\Omega_s & -\cos\Omega_s\sin\delta_s\\ \sin\Omega_s\cos\delta_s & \cos\Omega_s & -\sin\Omega_s\sin\delta_s\\ \sin\delta_s & 0 & \cos\delta_s\end{bmatrix}\end{aligned} \tag{11}$$

$$\mathbf{X}^{(sun)}=\mathbf{R}_5^{sun}\mathbf{X}^{(5)} \tag{12}$$

$$\mathbf{R}_5^{sun}=\begin{bmatrix}0 & 0 & 1\\ 1 & 0 & 0\\ 0 & 1 & 0\end{bmatrix} \tag{13}$$

Then:

$$\mathbf{X}^{(1)}=\mathbf{R}_{sun}^1\mathbf{R}_5^{sun}\mathbf{X}^{(5)}=\mathbf{R}_5^1\mathbf{X}^{(5)} \tag{14}$$

with:

$$\mathbf{R}_5^1=\mathbf{R}_{sun}^1\mathbf{R}_5^{sun}=\begin{bmatrix}\cos\Omega_s\cos\delta_s & -\sin\Omega_s & -\cos\Omega_s\sin\delta_s\\ \sin\Omega_s\cos\delta_s & \cos\Omega_s & -\sin\Omega_s\sin\delta_s\\ \sin\delta_s & 0 & \cos\delta_s\end{bmatrix}\begin{bmatrix}0 & 0 & 1\\ 1 & 0 & 0\\ 0 & 1 & 0\end{bmatrix} \tag{15}$$

$$\mathbf{R}_5^1=\begin{bmatrix}-\sin\Omega_s & -\cos\Omega_s\sin\delta_s & \cos\Omega_s\cos\delta_s\\ \cos\Omega_s & -\sin\Omega_s\sin\delta_s & \sin\Omega_s\cos\delta_s\\ 0 & \cos\delta_s & \sin\delta_s\end{bmatrix} \tag{16}$$

from the definition of RF(1), RF(0) and RF(sun) we have:

$$\delta_s=0 \tag{17}$$

and also

$$\mathbf{X}^{(1)}(Sun)=-\mathbf{X}^{(1)}(Merc)=-\mathbf{X}^{(0)}(Merc) \tag{18}$$

$$\mathbf{X}^{(0)}(Merc)=r_M\begin{bmatrix}\cos\nu_M\\ \sin\nu_M\\ 0\end{bmatrix} \tag{19}$$

$$\mathbf{X}^{(1)}(Sun)=\mathbf{R}_5^1\ \mathbf{X}^{(5)}(Sun) \tag{20}$$

$$\mathbf{X}^{(5)}\left(Sun\right) = r_M \begin{bmatrix} 0 \\ 0 \\ 1 \end{bmatrix} \tag{21}$$

$$\mathbf{X}^{(1)}(Sun) = r_M \begin{bmatrix} -\sin\Omega_s & -\cos\Omega_s \sin\delta_s & \cos\Omega_s \cos\delta_s \\ \cos\Omega_s & -\sin\Omega_s \sin\delta_s & \sin\Omega_s \cos\delta_s \\ 0 & \cos\delta_s & \sin\delta_s \end{bmatrix} \begin{bmatrix} 0 \\ 0 \\ 1 \end{bmatrix} = r_M \begin{bmatrix} \cos\Omega_s \cos\delta_s \\ \sin\Omega_s \cos\delta_s \\ \sin\delta_s \end{bmatrix} \tag{22}$$

then:

$$\begin{aligned} &\delta_s = 0 \\ &\cos\Omega_s = -\cos\nu_M \\ &\sin\Omega_s = -\sin\nu_M \end{aligned} \tag{23}$$

Substituting in the expression of $\mathbf{R}_5^1$ we obtain the matrix as a function of Mercury's true anomaly:

$$\mathbf{R}_5^1 = \begin{bmatrix} -\sin\Omega_s & 0 & \cos\Omega_s \\ \cos\Omega_s & 0 & \sin\Omega_s \\ 0 & 1 & 0 \end{bmatrix} = \begin{bmatrix} \sin\nu_M & 0 & -\cos\nu_M \\ -\cos\nu_M & 0 & -\sin\nu_M \\ 0 & 1 & 0 \end{bmatrix} \tag{24}$$

and the inverse:

$$\mathbf{R}_1^5 = \mathbf{R}_5^{1T} = \begin{bmatrix} \sin\nu_M & -\cos\nu_M & 0 \\ 0 & 0 & 1 \\ -\cos\nu_M & -\sin\nu_M & 0 \end{bmatrix} \tag{25}$$

3.2.3 Planetary IR irradiance computation

Some preliminary definitions are given (see Figure 3.6):

$\mathbf{n}_T$ = versor normal to the infinitesimal surface $d\mathbf{A}_T$ of the telescope T

$\mathbf{X}(T) = \mathbf{T} - \mathbf{O}_{Merc}$ = position vector of the telescope **T** from the center of the planet $\mathbf{O}_{Merc}$

$\mathbf{n}_P$ = versor normal to the surface of the planet at generic point **P**

$\mathbf{X}(P) = \mathbf{P} - \mathbf{O}_{Merc}$ = position vector of generic point **P** on the surface of the planet from the center of the planet $\mathbf{O}_{Merc}$

$\mathbf{s} = \mathbf{X}(T) - \mathbf{X}(P)$ = distance of **T** from **P**

$s = |\mathbf{s}|$ = norm of ***s***

$\mathbf{n}_s = \dfrac{\mathbf{s}}{s}$ = versor of ***s***

$\cos\left(\theta_P\right) = \mathbf{n}_P \cdot \mathbf{n}_s$

$\cos\left(\theta_T\right) = \mathbf{n}_T \cdot \left(-\mathbf{n}_s\right) = -\mathbf{n}_T \cdot \mathbf{n}_s$

T_P = temperature of the surface of the planet at point P

S_P = surface of the planet

σ = Stefan-Boltzmann constant

Then the IR irradiance from the planet to a telescope's surface $d\mathbf{A}_T$ is given by [8] :

$$q\left(IR\right)_{S_P \to dA_T} = \int_{S_P} \sigma T_P^4 \frac{\cos\left(\theta_P\right)\cos\left(\theta_T\right)}{\pi s^2} dS_P \quad [\mathrm{W/m^2}] \tag{26}$$

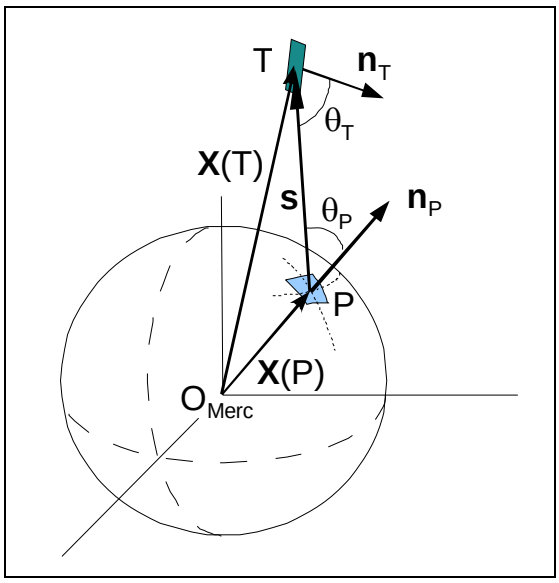

Figure 3.6

The integral is calculated by numerical method. The planetary surface is divided in two polar caps and a grid of meridians and parallel bands. Angles along longitude are indicated with ξ while angle along latitude are indicate with η , as shown in Figure 3.7.
Then we have the approximation:

$$q(IR)_{S_P \to dA_T} = \sum_{k_\eta=1}^{2N_\eta} \sum_{k_\xi=1}^{N_\xi} \sigma T_{P_k}^4 \frac{\cos(\theta_{P_k})\cos(\theta_{T_k})}{\pi s_k^2} S_{P_k} + \Delta q_{IR,POL} \quad [\text{W/m}^2] \qquad (27)$$

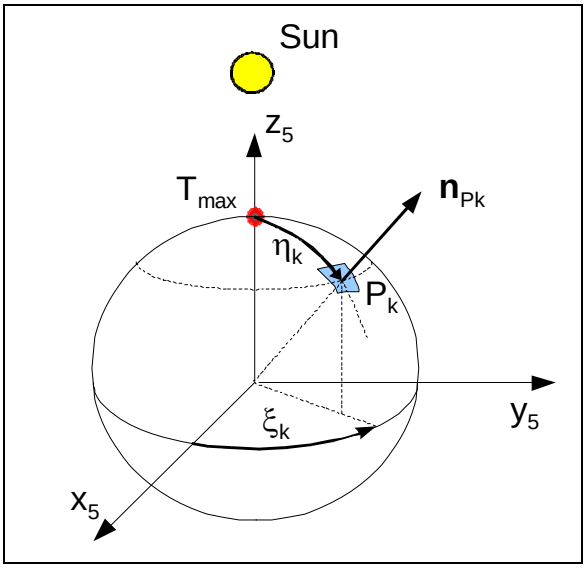

Figure 3.7

3.2.4 Temperature distribution on planetary surface

In order to compute the IR radiation incident on a surface that orbits the planet, a temperature distribution over the planet must be assumed. The temperature distribution is taken as suggested in [4] and [7]. A simplified planet black-body temperature distribution, that is suitable for thermal analyses of orbiting elements, is given by the following function (see Figure 3.7):

$$T_P(\eta) = T_{\max}\left[\cos(\eta)\right]^{1/4} \qquad (28)$$

The equation (28) holds until the minimum temperature T_{min} = 100K is reached. For higher values of η , the temperature is assumed constant and equal to T_{min}.

In equation (28), η is the zenith angle of the Sun and $T_{\max}$ is the maximum black-body *equilibrium* temperature occurring at the sub-solar point computed as:

$$T_{\max} = T_{\max}\left(\nu_M\right) = \sqrt[4]{SC_M \frac{\left(1-a\right)}{\sigma}} \tag{29}$$

where:

$'M'$ subscript refers to Mercury orbital parameters
SC = solar constant = 1370 W/m^2
ν_M = true anomaly of Mercury orbiting the Sun

$r_M = r\left(\nu_M\right) = \dfrac{p_M}{1+e_M \cos\left(\nu_M\right)}$ = distance Mercury-Sun

$d_{AU} = \dfrac{r_M}{r_{Earth}}$ [AU]

$SC_M = \dfrac{SC}{d_{AU}^2}$ [W/m^2] = Solar constant at Mercury

a = Mercury albedo coefficient = 0.12 (see: [7])
σ = Stefan-Boltzmann constant
$T_{\max}\left(0\right)$ = 688.6 K (planet's maximum temperature, perihelion case)
$T_{\max}\left(\pi\right)$ = 559.0 K (aphelion case)

The variation of $T_{\max}$ as a function of the Mercury true anomaly ν_M is derived from the previous equation (29) and is given with a good approximation by:

$$\frac{T_{\max}\left(\nu_M\right)}{T_{\max}\left(0\right)} = \sqrt{\frac{r\left(0\right)}{r\left(\nu_M\right)}} = \sqrt{\frac{1+e_M \cos\left(\nu_M\right)}{1+e_M}} \tag{30}$$

All temperatures calculated above are black-body temperatures.
Now it is possible to calculate the temperature distribution at Mercury surface, given the Mercury true anomaly ν_M , with the following procedure.

Evaluate the angle η_0 such that:

$$T_{\min} = T_{\max}\left[\cos\left(\eta_0\right)\right]^4 \tag{31}$$

then

$$\begin{aligned} T_{P_k} = T_P\left(\eta_k\right) = T_{\max}\left[\cos\left(\eta_k\right)\right]^{1/4} \qquad & if\ 0 \le \eta_k \le \eta_0 \\ T_{P_k} = T_P\left(\eta_k\right) = T_{\min} \qquad & if\ \eta_0 \le \eta_k \le \pi \end{aligned} \tag{32}$$

For example, the numerical values obtained at perihelion are (see [4]):

$T_{\max} = 688.8K \;\; T_{\min} = 100K \;\; \Rightarrow \eta_0 = 89.97°$

Temperature calculation at polar caps:

$$T_{POL,sunlit} = T_{\max}\left(\frac{1+\cos\Delta\eta_{POL}}{2}\right)^{1/4} \tag{33}$$

$$T_{POL,shadow} = T_{\min} \tag{34}$$

Calculation of cosines in the following formulas:

$$\cos\left(\theta_{P_k}\right) = \mathbf{n}_{P_k} \cdot \mathbf{n}_{S_k} = \mathbf{n}_{P_k}^{(5)T} \cdot \mathbf{n}_{S_k}^{(5)} \tag{35}$$

$$\cos\left(\theta_T\right) = -\mathbf{n}_T \cdot \mathbf{n}_{S_k} = -\mathbf{n}_T^{(5)T} \cdot \mathbf{n}_{S_k}^{(5)} \tag{36}$$

Versor normal to the surface of the planet

The components in RF(5) of the versor $\mathbf{n}_{P_k}$, normal to the point P_k on the planetary surface, are given by:

$$\mathbf{n}_{P_k}^{(5)} = \begin{bmatrix} \sin\eta_k \cdot \cos\xi_k \\ \sin\eta_k \cdot \sin\xi_k \\ \cos\eta_k \end{bmatrix} \tag{37}$$

Versor normal to a surface of the telescope dA_T

The components of the versor normal to a surface of the telescope are given in RF(4) and can be chosen for example as:

$$\mathbf{n}_T^{(4)} = \begin{bmatrix} 0 \\ 0 \\ 1 \end{bmatrix} \tag{38}$$

It must be projected in RF(5) using the following:

$$\mathbf{n}_T^{(5)} = \mathbf{R}_4^5 \cdot \mathbf{n}_T^{(4)} \tag{39}$$

$$\mathbf{R}_4^5 = \mathbf{R}_3^5 \cdot \mathbf{R}_4^3 = \mathbf{R}_1^5 \cdot \mathbf{R}_2^1 \cdot \mathbf{R}_3^2 \cdot \mathbf{R}_4^3 \tag{40}$$

Versor of the vector $\mathbf{s}_k$

Computation of components of vector $\boldsymbol{s}$: $\mathbf{s} = \mathbf{X}(T) - \mathbf{X}(P)$

Position vector $\mathbf{X}(P_k)$ of point P_k on the surface of the planet in RF(5) :

$$\mathbf{X}^{(5)}\left(P_k\right) = \begin{bmatrix} R_P \sin\eta_k \cos\xi_k \\ R_P \sin\eta_k \sin\xi_k \\ R_P \cos\eta_k \end{bmatrix} \tag{41}$$

Position vector of telescope $\mathbf{X}(T)$ in RF(2):

$$\mathbf{X}^{(2)}(T) = \begin{bmatrix} r\cos\nu \\ r\sin\nu \\ 0 \end{bmatrix} \tag{42}$$

with:

$$r = \frac{p}{1 + e \cdot \cos\nu} \tag{43}$$

where:

p = semi-latus rectum

e = eccentricity of S/C orbit

ν = true anomaly of S/C in orbit at Mercury

The position vector of telescope $\mathbf{X}(T)$ projected in RF(5) is given by:

$$\mathbf{X}^{(5)}(T) = \mathbf{R}_2^5\, \mathbf{X}^{(2)}(T) = \mathbf{R}_1^5\, \mathbf{R}_2^1\, \mathbf{X}^{(2)}(T) \tag{44}$$

Then the ***s*** vector can be expressed as:

$$\Rightarrow \mathbf{s}_k^{(5)} = \mathbf{X}^{(5)}(T) - \mathbf{X}^{(5)}(P_k) \tag{45}$$

And the norm of ***s*** is given by:

$$s_k = \left|\mathbf{s}_k^{(5)}\right| = \mathbf{s}_k^{(5)T} \cdot \mathbf{s}_k^{(5)} \tag{46}$$

Then the versor is:

$$\mathbf{n}_{S_k}^{(5)} = \frac{\mathbf{s}_k^{(5)}}{s_k} \tag{47}$$

To calculate the cosine terms of the equation (27) , we will use the equations (37), (39), (47) and substitute the versor values in the following algorithm:

$$\begin{aligned} \cos\left(\theta_{P_k}\right) &= \mathbf{n}_{P_k}^{(5)T} \cdot \mathbf{n}_{S_k}^{(5)} \quad if \left(\mathbf{n}_{P_k}^{(5)T} \cdot \mathbf{n}_{S_k}^{(5)}\right) > 0 \\ \cos\left(\theta_{P_k}\right) &= 0 \qquad\qquad else \end{aligned} \tag{48}$$

$$\begin{aligned} \cos\left(\theta_{T_k}\right) &= -\mathbf{n}_T^{(5)T} \cdot \mathbf{n}_{S_k}^{(5)} \quad if \left(-\mathbf{n}_T^{(5)T} \cdot \mathbf{n}_{S_k}^{(5)}\right) > 0 \\ \cos\left(\theta_{T_k}\right) &= 0 \qquad\qquad else \end{aligned} \tag{49}$$

3.2.5 Meshing the surface of the planet

The surface of the planet is assumed to be spherical and is divided in two polar caps and a grid of parallel and meridians bands.

The angular extension of polar caps is $\Delta\eta_{POL}$ from sub-solar point (see Figure 3.10, Figure 3.11).

These caps are not the physical poles of the planet, they are spherical caps bound with RF(5) and corresponding to the maximum (minimum) temperature of the planet.

The angular extension $\Delta\eta_{POL}$ is taken equal to *1°*, thus the caps have been considered as planar surfaces with regards to fluxes computation.

Let us define:

- Number of meridians bands: N_ξ
- Number of latitude bands: N_η
- Angular extension of meridian bands: (see Figure 3.8)

$$\Delta\xi = \frac{2\pi}{N_\xi} \tag{50}$$

- Angular extension of latitude bands: (see Figure 3.8)

$$\Delta\eta = \frac{\left(\pi/2 - \Delta\eta_{POL}\right)}{N_\eta} \tag{51}$$

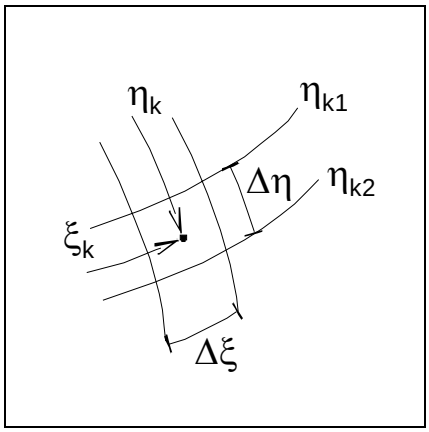

Figure 3.8

Grid coordinates (see Figure 3.8):

$$\begin{aligned} \eta_k &= \Delta\eta_{POL} + \Delta\eta/2 + (k_\eta - 1)\Delta\eta \\ \xi_k &= \Delta\xi/2 + (k_\xi - 1)\Delta\xi \end{aligned} \quad \text{with:} \quad \begin{aligned} k_\eta &= 1,\ldots,N_\eta \\ k_\xi &= 1,\ldots,N_\xi \end{aligned} \tag{52}$$

Area of grid elements S_{P_k} (see Figure 3.8):

$$\begin{aligned} \eta_{k1} &= \Delta\eta_{POL} + (k_\eta - 1)\Delta\eta = \eta_k - \Delta\eta/2 \\ \eta_{k2} &= \Delta\eta_{POL} + k_\eta\,\Delta\eta = \eta_k + \Delta\eta/2 \end{aligned} \tag{53}$$

defining (see Figure 3.9)

$$\begin{aligned} R_1 &= R_P \sin\eta_{k1} \\ R_2 &= R_P \sin\eta_{k2} \\ H &= R_P(\cos\eta_{k1} - \cos\eta_{k2}) \\ L &= \sqrt{(R_2 - R_1)^2 + H^2} \end{aligned} \tag{54}$$

then:

$$S_{P_k} = \frac{R_1 + R_2}{2} \cdot \Delta\xi \cdot L \tag{55}$$

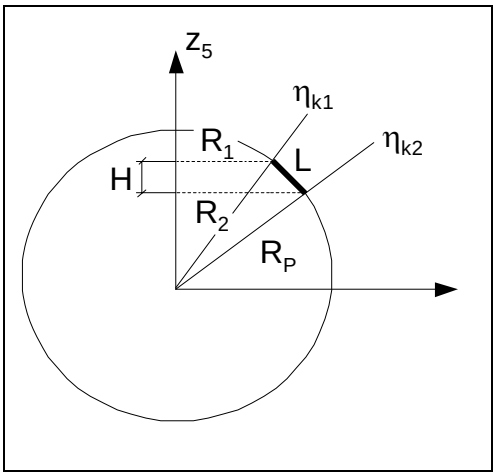

Figure 3.9

Computation of IR flux due to spherical caps $\Delta q_{IR,POL}$: (see Figure 3.10, Figure 3.11)

$$\mathbf{n}^{(5)}_{POL,sunlit} = \begin{bmatrix} 0 \\ 0 \\ 1 \end{bmatrix}; \quad \mathbf{n}^{(5)}_{POL,shadow} = \begin{bmatrix} 0 \\ 0 \\ -1 \end{bmatrix} \tag{56}$$

$$X_{POL} = R_P \frac{\left(1+\cos\Delta\eta_{POL}\right)}{2} \tag{57}$$

$$\begin{aligned} \mathbf{X}^{(5)}\left(POL, sunlit\right) &= X_{POL} \cdot \mathbf{n}^{(5)}_{POL,sunlit} \\ \mathbf{X}^{(5)}\left(POL, shadow\right) &= X_{POL} \cdot \mathbf{n}^{(5)}_{POL,shadow} \end{aligned} \tag{58}$$

$$\mathbf{s}^{(5)}_{POL} = \mathbf{X}^{(5)}\left(T\right) - \mathbf{X}^{(5)}\left(POL\right) \tag{59}$$

$$s_{POL} = \left|\mathbf{s}^{(5)}_{POL}\right| \tag{60}$$

$$\mathbf{n}^{(5)}_{S_{POL}} = \frac{\mathbf{s}^{(5)}_{POL}}{s_{POL}} \tag{61}$$

cosines computation:

$$\begin{aligned} \cos\left(\theta_{POL}\right) &= \mathbf{n}^{(5)\ T}_{POL} \cdot \mathbf{n}^{(5)}_{S_{POL}} \quad IF\left(\mathbf{n}^{(5)\ T}_{POL} \cdot \mathbf{n}^{(5)}_{S_{POL}}\right) > 0 \\ \cos\left(\theta_{POL}\right) &= 0 \quad ELSE \end{aligned} \tag{62}$$

$$\begin{aligned} \cos\left(\theta_{T}\right) &= -\mathbf{n}^{(5)T}_{T} \cdot \mathbf{n}^{(5)}_{S_{POL}} \quad IF\left(-\mathbf{n}^{(5)T}_{T} \cdot \mathbf{n}^{(5)}_{S_{POL}}\right) > 0 \\ \cos\left(\theta_{T}\right) &= 0 \quad ELSE \end{aligned} \tag{63}$$

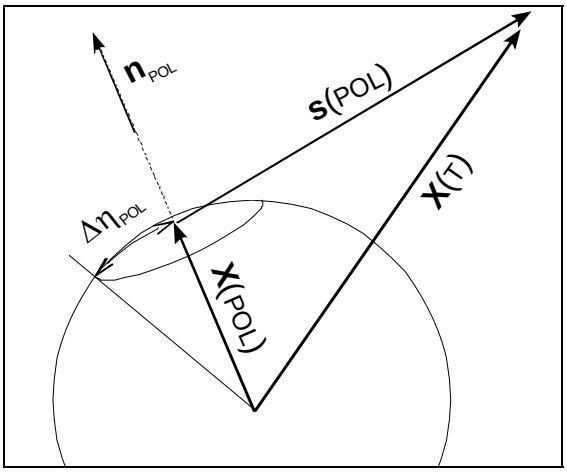

Figure 3.10

Spherical cap surface:

$$S_{POL} = 2\pi R_P^2\left(1-\cos\Delta\eta_{POL}\right) \tag{64}$$

IR flux due to spherical caps

$$\Delta q_{IR,POL} = \sigma T_{POL}^4 \frac{\cos\left(\theta_T\right)\cos\left(\theta_{POL}\right)}{\pi s_{POL}^2} S_{POL} \tag{65}$$

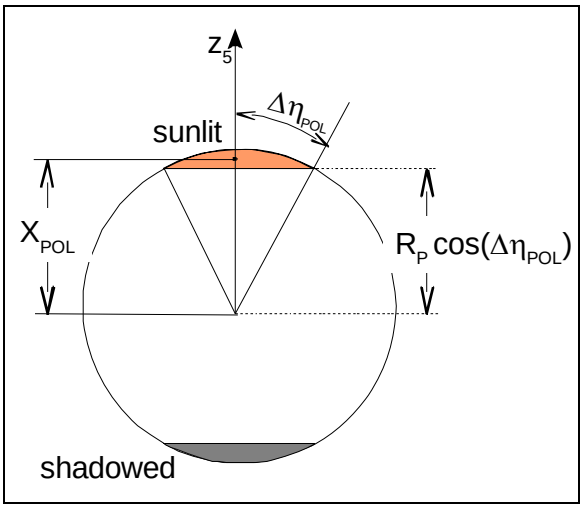

Figure 3.11

Now we can substitute into equation (27) and calculate the value of IR flux from Mercury surface.

3.2.6 Albedo irradiance computation

In order to compute the albedo flux incident on a surface that orbits the planet, it is necessary to introduce some preliminary definitions: (see Figure 3.12)

$\mathbf{n}_T$ = versor normal to the infinitesimal surface $d\mathbf{A}_T$ of the telescope T

$\mathbf{n}_P$ = versor normal to the surface of the planet at generic point P

$\mathbf{n}_s = \frac{\mathbf{s}}{s}$ = versor of **s** (distance of T from P)

$\mathbf{n}_{SUN}$ = versor towards the Sun direction

$SC_M = \frac{SC}{d_{AU}^2}$ [AU] = solar constant at season ν_M

a = Mercury albedo coefficient = 0.12 (see: [7])

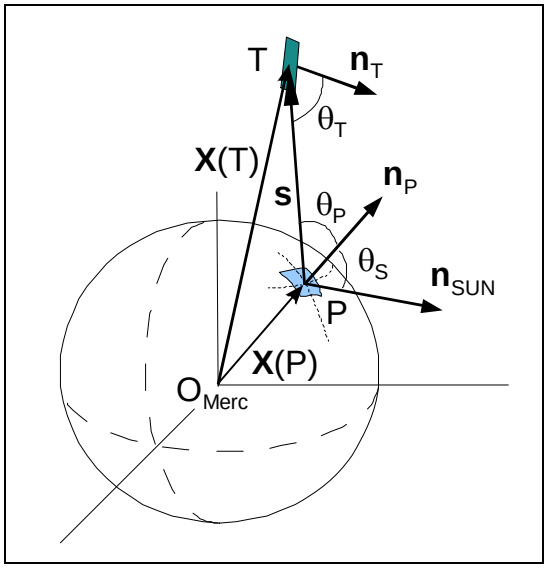

Figure 3.12

directional cosines are computed as follows: (see Figure 3.12)

$$\cos\left(\theta_P\right) = \mathbf{n}_P \cdot \mathbf{n}_s \tag{66}$$

$$\cos\left(\theta_T\right) = \mathbf{n}_T \cdot \left(-\mathbf{n}_s\right) = -\mathbf{n}_T \cdot \mathbf{n}_s \tag{67}$$

$$\cos\left(\theta_S\right) = \mathbf{n}_{SUN} \cdot \mathbf{n}_P \tag{68}$$

To compute the albedo fluxes, it will be used the same grid of Mercury surface introduced for IR fluxes computation.

Solar irradiation: the incident solar radiation on elementary surface S_{P_k} :

$$SC_M \cdot \cos\left(\theta_S\right) \tag{69}$$

Then the albedo flux on a surface T orbiting Mercury is given by:

$$q\left(ALBEDO\right)_{S_P \to dA_T} = \sum_{k_\eta=1}^{2N_\eta} \sum_{k_\xi=1}^{N_\xi} a \cdot SC_M \cdot \cos\left(\theta_{S_k}\right) \cdot \frac{\cos\left(\theta_{P_k}\right)\cos\left(\theta_{T_k}\right)}{\pi s_k^2} S_{P_k} + \Delta q_{A,POL} \tag{70}$$

To calculate the cosine terms, the following equations are used:

$$\begin{aligned} \cos\left(\theta_{P_k}\right) &= \mathbf{n}_{P_k}^{(5)T} \cdot \mathbf{n}_{S_k}^{(5)} \quad if\ \left(\mathbf{n}_{P_k}^{(5)T} \cdot \mathbf{n}_{S_k}^{(5)}\right) > 0 \\ \cos\left(\theta_{P_k}\right) &= 0 \qquad\qquad else \end{aligned} \tag{71}$$

$$\begin{aligned} \cos\left(\theta_{T_k}\right) &= -\mathbf{n}_T^{(5)T} \cdot \mathbf{n}_{S_k}^{(5)} \quad if\ \left(-\mathbf{n}_T^{(5)T} \cdot \mathbf{n}_{S_k}^{(5)}\right) > 0 \\ \cos\left(\theta_{T_k}\right) &= 0 \qquad\qquad else \end{aligned} \tag{72}$$

$$\begin{aligned} \cos\left(\theta_{S_k}\right) &= \mathbf{n}_{SUN}^{(5)\ T} \cdot \mathbf{n}_{P_k}^{(5)} \quad if\ \left(\mathbf{n}_{SUN}^{(5)\ T} \cdot \mathbf{n}_{P_k}^{(5)}\right) > 0 \\ \cos\left(\theta_{S_k}\right) &= 0 \qquad\qquad else \end{aligned} \quad \text{with: } \mathbf{n}_{SUN}^{(5)} = \begin{bmatrix} 0 \\ 0 \\ 1 \end{bmatrix} \tag{73}$$

To calculate the albedo flux due to polar caps, we will use a similar approach used in IR flux computation. Then we have:

$$\Delta q_{A,POL} = a \cdot SC_M \cdot \cos\left(\theta_{S_{POL}}\right) \frac{\cos\left(\theta_T\right)\cos\left(\theta_{POL}\right)}{\pi s_{POL}^2} S_{POL} \tag{74}$$

Now we can substitute into equation (70) and calculate the value of albedo irradiance from the Mercury surface.

3.2.7 Solar irradiance and Sun Incidence Angle computation

In order to compute the solar radiation incident on a surface that orbits the planet, we recall some definitions. We have:

$\mathbf{n}_T$ = versor normal to the infinitesimal surface d$\mathbf{A}_T$ of the telescope T

$\mathbf{n}_{SUN}$ = versor towards the Sun direction, such that: $\mathbf{n}_{SUN}^{(5)} = \begin{bmatrix} 0 \\ 0 \\ 1 \end{bmatrix}$

To distinguish the case in which the Sun lights up the back side of the surface d$\mathbf{A}_T$, the direction cosine function is defined as:

$$\begin{array}{ll} \cos(\theta_{SUN}) = \mathbf{n}_T \cdot \mathbf{n}_{SUN} & IF\ (\mathbf{n}_T \cdot \mathbf{n}_{SUN}) > 0 \\ \cos(\theta_{SUN}) = 0 & ELSE \end{array} \tag{75}$$

An eclipse function f_{ecl} will be defined as follows:

$$\begin{array}{l} f_{ecl} = 0 \quad IF\ S/C\ full\ shadowed \\ f_{ecl} = 1 \quad IF\ S/C\ sun\ lighted \end{array} \tag{76}$$

This function takes into account the shadowing occurrence of S/C during orbit and will be afterwards described in details. In this model the eclipse is computed assuming a cylindrical shadow.
Given the previous definitions, the solar irradiance is given by:

$$q_{SOLAR} = SC_M \cdot \cos(\theta_{SUN}) \cdot f_{ecl} \quad [\mathrm{W/m^2}] \tag{77}$$

with:

$SC_M = \dfrac{SC}{d_{AU}^2}$ [W/m^2] = solar radiation at season corresponding to Mercury's anomaly ν_M

SC = solar constant = 1370 [W/m^2]

$d_{AU} = \dfrac{r_M}{r_{Earth}}$ [AU] = distance Mercury - Sun

$\mathbf{X}(T) = \mathbf{T} - \mathbf{O}_{Merc}$ = position vector of the telescope T from the centre of the planet O_{Merc}

Detailed description of the **eclipse function** f_{ecl}

Referring to Figure 3.13, the following quantities are considered:

$\mathbf{X}(T) = \mathbf{T} - \mathbf{O}_{Merc}$ = position vector of the telescope T from the centre of the planet O_{Merc}
it lies on S/C orbital plane.

$\mathbf{n}_{SUN}$ = versor that points toward the Sun; could be out of S/C orbital plane

The two vectors $\mathbf{X}(T)$ and $\mathbf{n}_{SUN}$ produces a new plane, called Σ.

The vector $\mathbf{X}(T)$ can be expressed with the two components in the Σ-plane :

- parallel to $\mathbf{n}_{SUN}$: $\mathbf{X}(T)_{sun} = \mathbf{X}(T) \cdot \mathbf{n}_{SUN}$ (78)
- orthogonal to $\mathbf{n}_{SUN}$: $\mathbf{X}(T)_{orth} = \mathbf{X}(T) - \mathbf{X}(T)_{sun}$ (79)

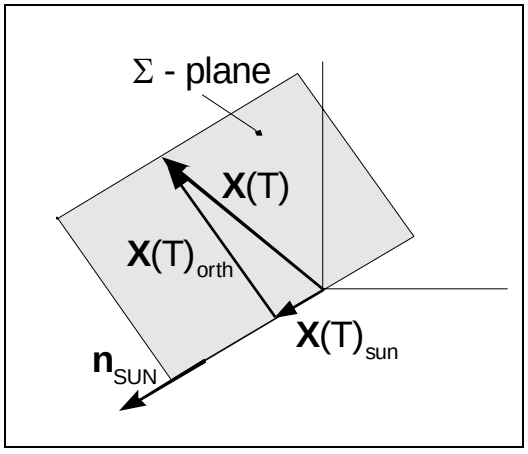

Figure 3.13

Referring to the Σ-plane we can have three different cases, as shown in Figure 3.14, then it is possible to calculate the eclipse function f_{ecl} by using the algorithm:

IF $\left\|\mathbf{X}(T)_{sun}\right\| \geq 0$

$f_{ecl} = 1$

ELSE

IF $\left\|\mathbf{X}(T)_{orth}\right\| \geq R_P$

$f_{ecl} = 1$

ELSE

$f_{ecl} = 0$

END

END

Then substituting in equation (77) we can calculate the solar flux incident on the surface dA_T.

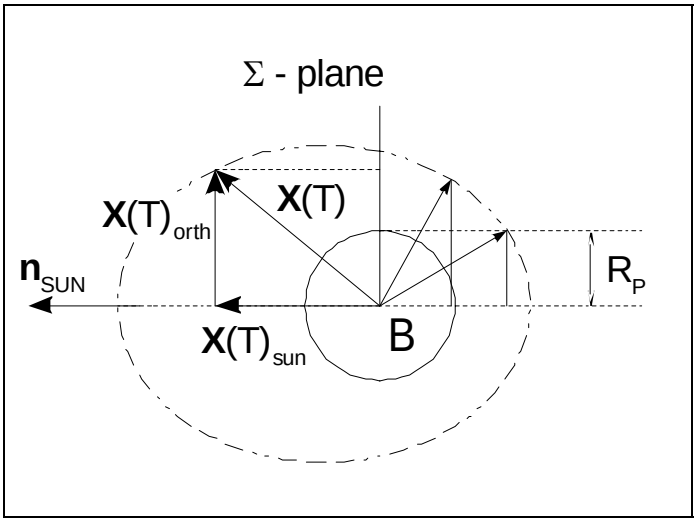

Figure 3.14

It should be also underlined that the plane Σ in general, is not coplanar to the orbital plane; in fact, both $\mathbf{n}_{SUN}$ and $\mathbf{n}_T$ could not lies on S/C orbital plane.

The ***SUN INCIDENCE ANGLE*** is defined as the angle between the normal to the considered surface $d\boldsymbol{A}_T$ and the Sun direction and it is given by (see **Figure 3.15**):

$$\theta_{SUN} = \arccos\left(\mathbf{n}_T \cdot \mathbf{n}_{SUN}\right) \tag{80}$$

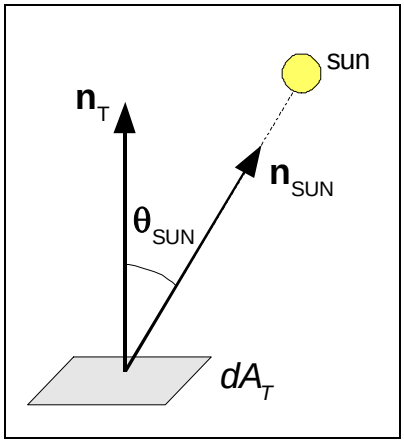

Figure 3.15

It follows that, during the sunlit phases, the solar incidence angle θ_{SUN} value must belong to the interval $0° \le \theta_{SUN} \le 90°$.

Regarding to the evaluation of the Sun incidence angle θ_{SUN} , in this analysis the surface d$\mathbf{A}_T$ is taken as a surface normal to the instrument optical axis, thus the versor $\mathbf{n}_T$ is aligned to the instrument axis.

Then, for the case herein considered, the critical values of the Sun incidence angle θ_{SUN} are the minima, for which a direct Sun illumination of the focal plane could occur.

3.2.8 Computation of True Anomaly as a function of Time and vice versa:

True anomaly as a function of time :

$\boxed{t \to M \to E \to \nu}$

Choose:

N_{time} = Number of instant among half orbit (from periherm to apoherm)

T_0 = S/C orbital period

$\Delta t = T_0 / N_{time}$ = time interval

Given t, calculate *Mean motion*:

$$n_0 = \sqrt{\frac{\mu_M}{a^3}} \tag{81}$$

with:

a = semi-major axis of S/C orbit

μ_M = Mercury gravitational constant

mean anomaly:

$$M = n_0 t \tag{82}$$

Find eccentric anomaly E value such that:

$$M = E - e \cdot \sin(E) \tag{83}$$

$$\tan\left(\frac{\nu}{2}\right) = \sqrt{\frac{1+e}{1-e}} \cdot \tan\left(\frac{E}{2}\right) \tag{84}$$

Then can be calculated the true anomaly:

$$\nu = 2 \cdot \arctan\left(\sqrt{\frac{1+e}{1-e}} \cdot \tan\left(\frac{E}{2}\right)\right) = 2 \cdot \arctan\left(\frac{\sqrt{\frac{1+e}{1-e}} \cdot \sin\left(\frac{E}{2}\right)}{\cos\left(\frac{E}{2}\right)}\right) \tag{85}$$

Time as a function of true anomaly

$\boxed{\nu \to E \to M \to t}$

Given ν , calculate:

$$\tan\left(\frac{E}{2}\right) = \sqrt{\frac{1-e}{1+e}} \cdot \tan\left(\frac{\nu}{2}\right) \tag{86}$$

then calculate the eccentric anomaly E :

$$E = 2 \cdot \arctan\left(\sqrt{\frac{1-e}{1+e}} \cdot \tan\left(\frac{\nu}{2}\right)\right) = 2 \cdot \arctan\left(\frac{\sqrt{\frac{1-e}{1+e}} \cdot \sin\left(\frac{\nu}{2}\right)}{\cos\left(\frac{\nu}{2}\right)}\right) \tag{87}$$

find mean anomaly M :

$$M = E - e \cdot \sin(E) \tag{88}$$

then

$$t = \frac{M}{n_0} \tag{89}$$

3.2.9 Eclipse Terminator Calculation and effects on solar irradiance estimation

In this model a number of equidistant time instants, at which the heat fluxes will be evaluated, is stated at the beginning of the code.

As previously explained, to evaluate the solar fluxes, the function f_{ecl} of equation (76) is computed at each point along orbit and then substituted into equation (77).

Then, at positions of the S/C crossing the eclipse entry/exit (see points **1** and **2** in Figure 3.16), the eclipse function will not show a trend similar to a step-like function, as expected, because the eclipse terminator points have not been yet evaluated. It must be pointed out that, in this model, the planet's shadow is assumed to be cylindrical.

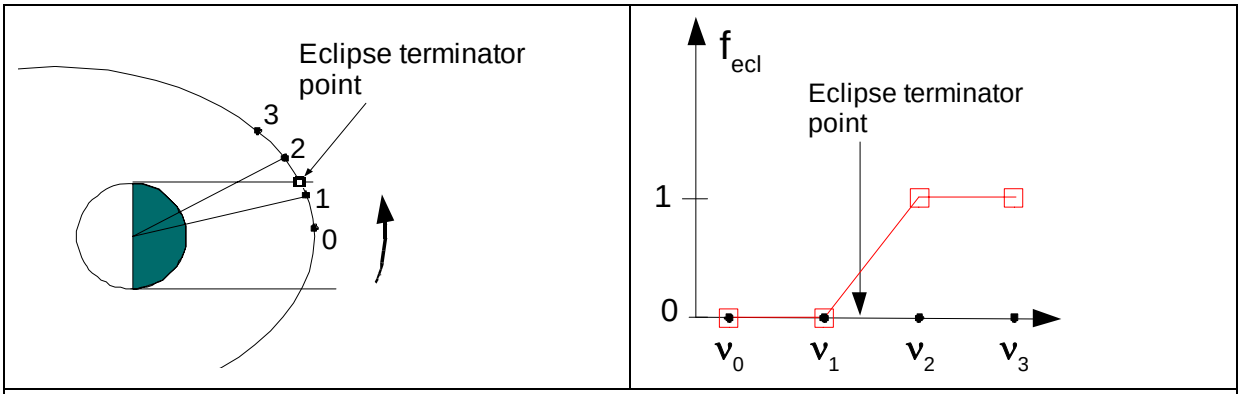

Figure 3.16: eclipse terminator point not computed

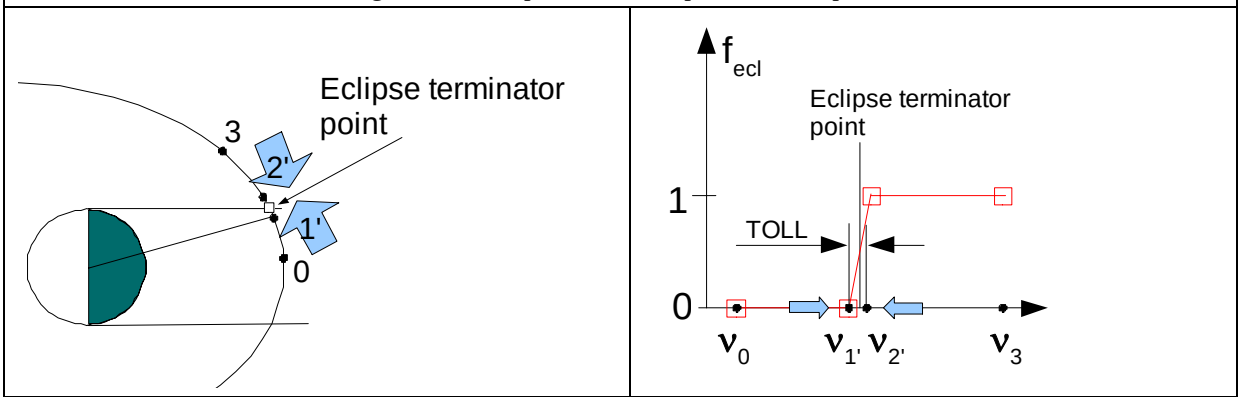

Figure 3.17: eclipse terminator point computation

This could yield to a considerable underestimation of solar flux, which often reaches the peak value at eclipse terminator positions (i.e. at point **2'** in Figure 3.17). In Figure 3.18 this numerical error could be better understood and is named $\Delta q_{SUN,\max}$.

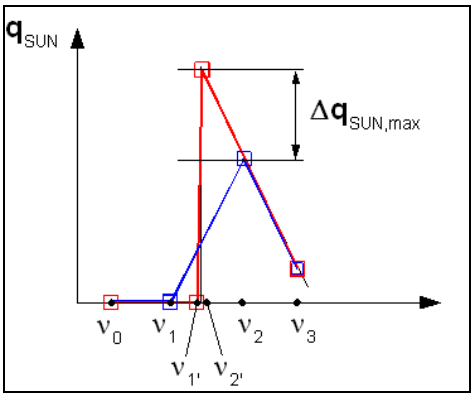

Figure 3.18

To avoid this, it has been implemented a subroutine that computes the S/C eclipse terminator points and/or the telescope surface shadowed/lighten transition points.
The eclipse terminator points are computed by considering the two sequential points in orbit 'crossing' the eclipse terminator (points **1** and **2** in Figure 3.16) and shifting their values of true anomaly ν along orbit such that the difference between them would be less than a tolerance value TOLL imposed (see points **1'** and **2'** of Figure 3.17).
In this model the default value of TOLL is taken equal to: TOLL = 10^{-8} rad.

This approach leads to considerably reduce the numerical error in incident fluxes computation without increasing the number of position on the orbit and then the number of heat fluxes evaluation.

The implemented code can also compute the true anomaly values corresponding to eclipse entry/exit and display if eclipse does occur. The code can also compute and display the S/C eclipse occurrence and/or the shadowing of the considered surface by the S/C (back illumination).

A quantitative example of the effects of S/C eclipse terminator calculation is reported in [10], where it is shown that for the case of perihelion orbit, using a number of 20 points among half orbit, the value of $\Delta q_{SUN,\max}$, which is the difference between peak value of solar flux calculated with and without eclipse computation, is about equal to $\Delta q_{SUN,\max}$ = 1300 W/m^2.

3.2.10 The orbiting surfaces

The previously described mathematical model can be used to estimate the incident heat fluxes on a surface of a S/C orbiting a planet and the Sun incidence angle with the surface normal.
In this contest the orbiting surface considered for the simulation are the surfaces normal to the optical axes of the SIMBIO-SYS channels on board MPO spacecraft of the BepiColombo mission at Mercury (see Figure 3.19).

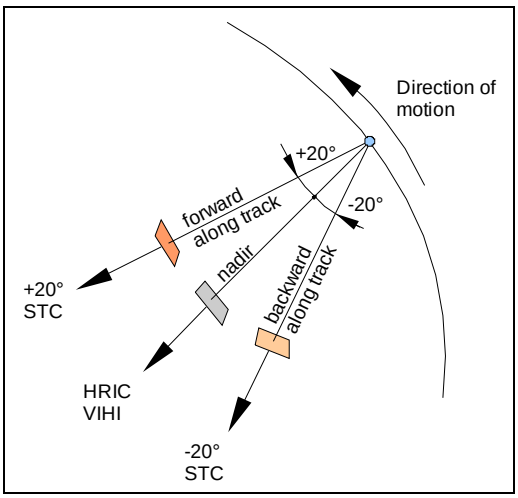

Figure 3.19

The surface are described with the components of the normal $\mathbf{n}_T^{(4)}$ in the RF(4) – Body fixed reference frame, as defined in Figure 3.4. To make easier the input of the components of $\mathbf{n}_T^{(4)}$ for the simulation, an angle α_{INSTR} has been introduced (see Figure 3.20), then the components of the normal are given by:

$$\mathbf{n}_T^{(4)} = \begin{bmatrix} \sin(\alpha_{INSTR}) \\ 0 \\ \cos(\alpha_{INSTR}) \end{bmatrix} \tag{90}$$

and the orbiting surface considered are:

Surface normal /	α_{INSTR} [deg]
Nadir / HRIC, VIHI	0°
Forward along track / STC + 20°	+ 20°
Backward along track / STC – 20 °	- 20 °

Table 3.1

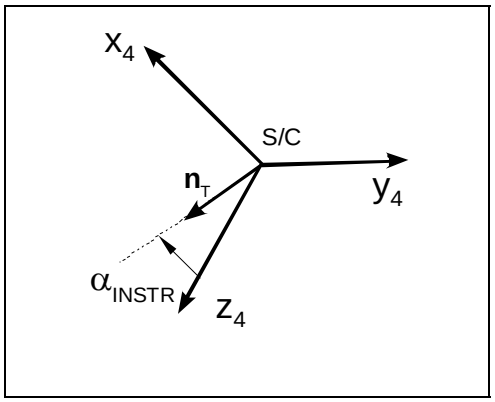

Figure 3.20

3.2.11 Input parameters

The parameters given in the following Table 3.2 and Table 3.3 will be taken as ***reference*** input parameters for the simulations. These *input* data corresponds to Mercury planet at perihelion, S/C attitude nadir pointing and the orbiting surface is chosen within one of the three indicated. Orbital parameters and physical data are taken from [1] and [7].

INPUT PARAMETERS	
N_{time} = 50	Number of time points among half orbit
ν_M = 0°(PERIHELION)	season: true anomaly of the planet
$T_{\min}$ = 100 K	minimum Mercury surface temperature - shadowed face of the planet
$T_{\max}(0)$= 688.6 K	maximum Mercury surface temperature at perihelion
a = 0.12	Albedo coefficient
INPUT DATA - S/C ORBIT AROUND MERCURY	
Ω = 0°	RAAN
i_0 = 90°	Inclination
ω_P = 0°	argument of perigee
h_a = 1508 km	apoherm altitude ha
h_p = 400 km	periherm altitude hp
INPUT DATA - S/C attitude	
ψ = 0°	yaw angle
θ = 0°	pitch angle
ϕ = 0°	roll angle
INPUT DATA – orbiting surface	
α_{INSTR} = 0°	Toward Nadir (HRIC, VIHI)
α_{INSTR} = +20°	Forward along track (STC +20°)
α_{INSTR} = -20°	Backward along track (STC -20°)
INPUT DATA - Mesh size on Mercury surface	
N_{ξ} = 60	Mesh size on Mercury surface Number of meridian bands
N_{η} = 24	Mesh size on Mercury surface Number of latitude bands
$\Delta\eta_{POL}$ = 1°	Mesh size on Mercury surface Angular amplitude of polar caps
TOLL = 10^-8 radian	Tolerance in eclipse position calculation

Table 3.2

OTHER PHYSICAL CONSTANTS USED	
AU = 149.6*10^6 km	Astronomical Unit
R_p = 2439.99 km	Mercury radius RM [km]
μ_M = 22032.080 [km^3/s^2];	Mercury gravitational constant
e_M = 0.20563	Mercury orbit eccentricity
r_{pM} = 46*10^6; km	Mercury perihelion distance
σ = 5.670400e-008 [W/(m^2*K^4)]	Stefan-Boltzmann constant
SC = 1370 [W/m^2]	Solar Constant

Table 3.3

3.3 Simulations and Results

3.3.1 Thermal environment scenario during Mercury orbit around the Sun

In this set of simulations solar, albedo and IR planetary heat fluxes are calculated as a function of both true anomaly of spacecraft orbiting around Mercury and Mercury season (i.e. true anomaly of Mercury orbiting the Sun). The results reported are graphs that give an overview of the thermal environment encountered by the orbiting surfaces considered.
The cases analyzed in this set of simulations are summarized in the following Table 3.4.

Thermal environment scenario during half Mercury orbit around the Sun			
Case #	**Surface normal**		**Season**
1	Nadir (HRIC, VIHI)	$\alpha_{INSTR} = 0°$	ν_M from 0° to 180°
2	Forward along track +20° (STC /H)	$\alpha_{INSTR} = +20°$	ν_M from 0° to 180°
3	Backward along track -20° (STC /L)	$\alpha_{INSTR} = -20°$	ν_M from 0° to 180°
All parameters other than ν_M *and* α_{INSTR} *are those reported in* Table 3.2 and Table 3.3.			

Table 3.4

Case 1: surface normal pointing toward nadir (HRIC, VIHI)

In the following Figure 3.21, Figure 3.22, Figure 3.23 the graphs of the incident fluxes on a surface grazing the HRIC and VIHI entrance are reported. The orbital and attitude parameters of the spacecraft are the nominal values reported in Table 3.2 and Table 3.3. The colored bar on the left of the figures is proportional to incident heat fluxes [W/m^2]

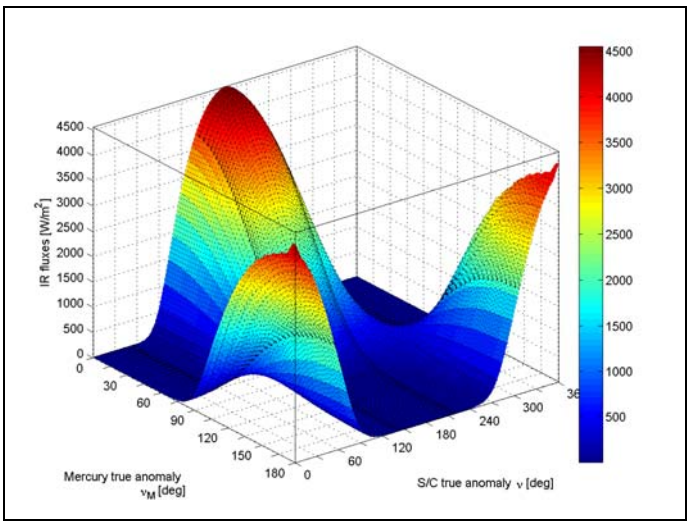

Figure 3.21: *The IR planetary fluxes incident on a surface with normal pointing toward nadir as a function of the true anomaly of the S/C orbit around Mercury and of the true anomaly of Mercury planet around the Sun.*

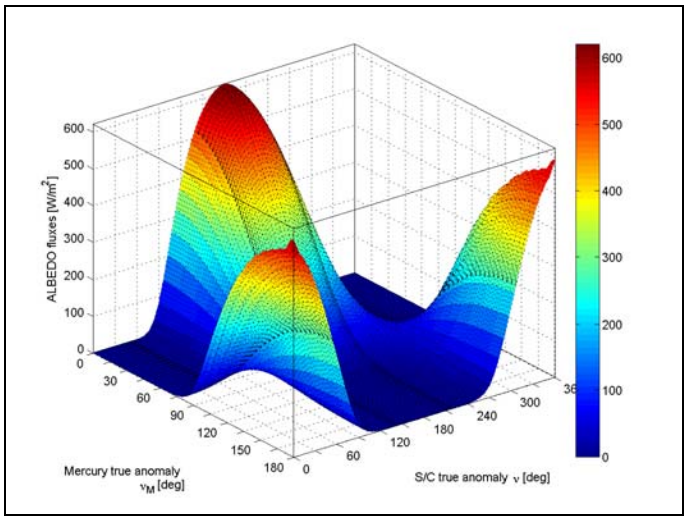

Figure 3.22: The ALBEDO fluxes incident on a surface with normal pointing toward nadir as a function of the true anomaly of the S/C orbit around Mercury and of the true anomaly of Mercury planet around the Sun.

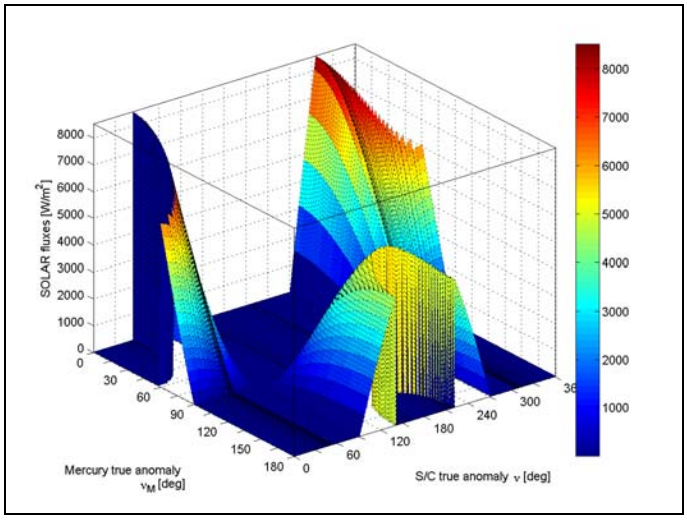

Figure 3.23: The SOLAR fluxes incident on a surface with normal pointing toward nadir as a function of the true anomaly of the S/C orbit around Mercury and of the true anomaly of Mercury planet around the Sun. The hollows of the surface corresponds to eclipses occurrence.

Case 2: surface normal pointing forward along track (STC +20°)

In the following Figure 3.24, Figure 3.25, Figure 3.26 the graphs of the incident fluxes on a surface normal to the axis of the STC optic pointing +20° forward along track are reported.
The orbital and attitude parameters of the spacecraft are the nominal values reported in Table 3.2 and Table 3.3. The colored bar on the left of the figures is proportional to incident heat fluxes [W/m^2]

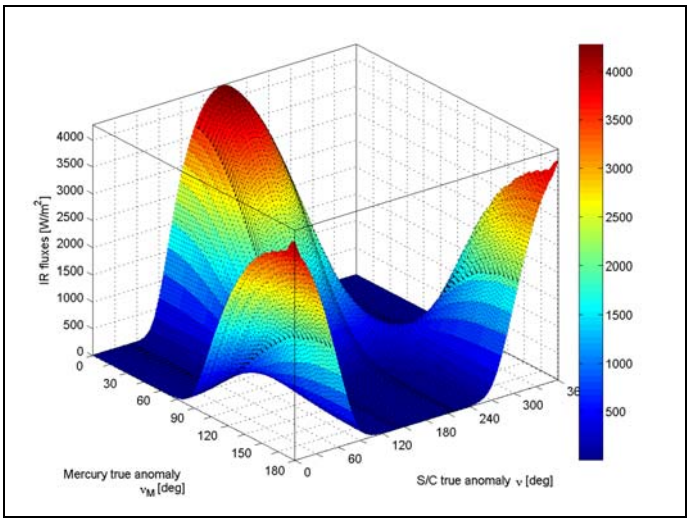

Figure 3.24: The IR planetary fluxes incident on a surface with normal pointing +20° forward along track as a function of the true anomaly of the S/C orbit around Mercury and of the true anomaly of Mercury planet around the Sun.

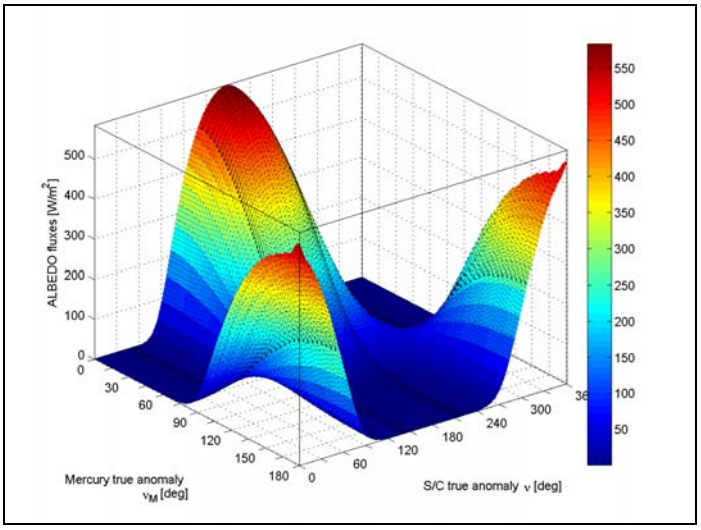

Figure 3.25: The ALBEDO fluxes incident on a surface with normal pointing +20° forward along track as a function of the true anomaly of the S/C orbit around Mercury and of the true anomaly of Mercury planet around the Sun.

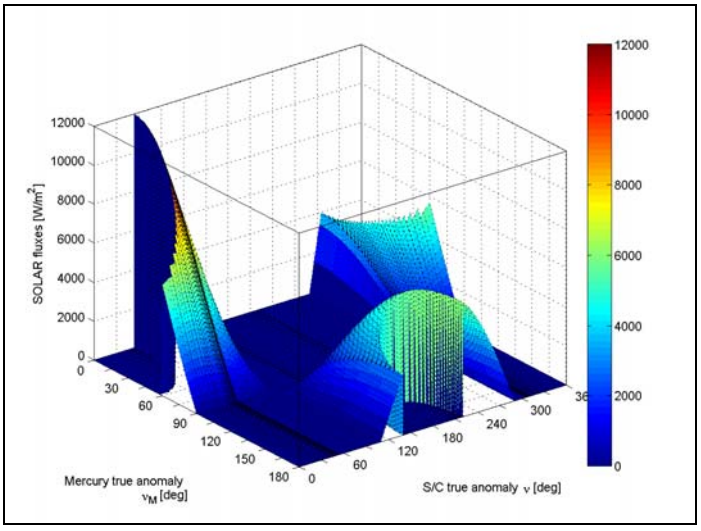

Figure 3.26: The SOLAR fluxes incident on a surface with normal pointing +20° forward along track as a function of the true anomaly of the S/C orbit around Mercury and of the true anomaly of Mercury planet around the Sun.The hollows of the surface corresponds to eclipses occurrence.

Case 3: surface normal pointing backward along track (STC -20°)

In the following Figure 3.27, Figure 3.28, Figure 3.29, the graphs of the incident fluxes on a surface normal to the axis of the STC optic pointing +20° forward along track are reported.
The orbital and attitude parameters of the spacecraft are the nominal values reported in Table 3.2 and Table 3.3. The coloured bar on the left of the figures is proportional to heat fluxes [W/m^2]

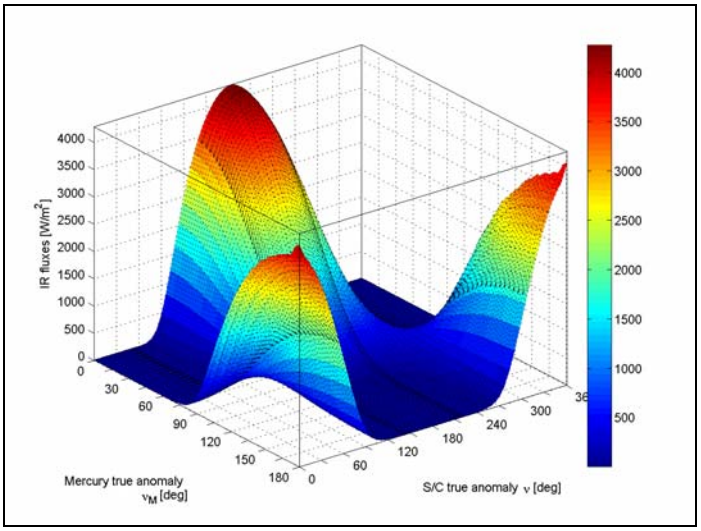

Figure 3.27: The IR planetary fluxes incident on a surface with normal pointing -20° backward along track as a function of the true anomaly of the S/C orbit around Mercury and of the true anomaly of Mercury planet around the Sun.

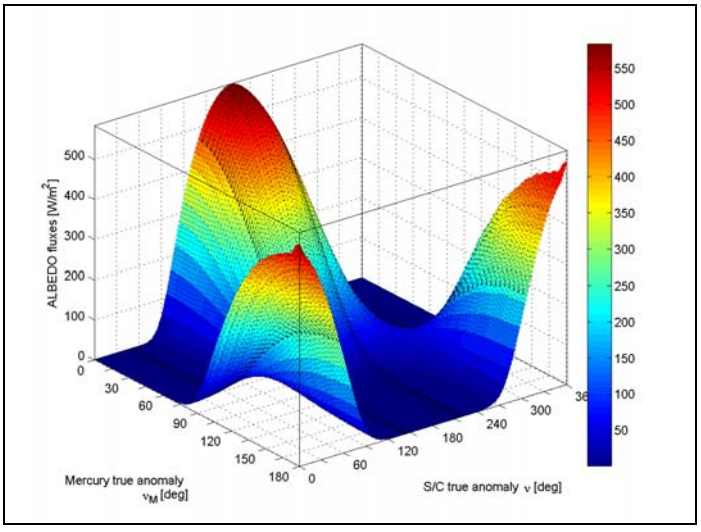

Figure 3.28: The ALBEDO fluxes incident on a surface with normal pointing -20° backward along track as a function of the true anomaly of the S/C orbit around Mercury and of the true anomaly of Mercury planet around the Sun.

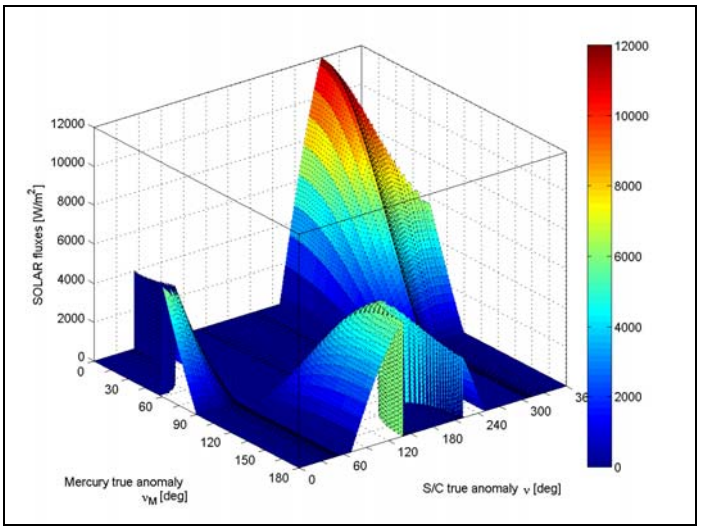

Figure 3.29: The SOLAR fluxes incident on a surface with normal pointing -20° backward along track as a function of the true anomaly of the S/C orbit around Mercury and of the true anomaly of Mercury planet around the Sun. The hollows of the surface corresponds to eclipses occurrence.

From these simulations it shall be acknowledged that the hot cases occurs at Mercury ***perihelion*** ($\nu_M = 0°$) and ***aphelion*** ($\nu_M = 180°$) and that the cold case occurs at Mercury ***autumn/spring*** ($\nu_M = 90°$). These cases will be analysed more in detail in the following chapter.

3.3.2 Heat fluxes at specific Mercury seasons

In the following paragraph will be presented the results of computation of the incident heat fluxes (solar, albedo and planetary IR) at some specific Mercury season. The unitary orbiting surface interested in the analysis are, as previously specified, orthogonal to the axes of the aperture of the SIMBIO-SYS optical channels (see paragraph 3.2.10 and Figure 3.19).
The Mercury seasons chosen for the analysis are the crucial thermal cases identified in the analysis and simulations previously performed (see paragraph 3.3.1): they are perihelion, aphelion and equinox orbits. The cases analyzed are summarized in the following table:

chapter	Surface normal pointing (channel)	Mercury season	Mercury true anomaly
3.3.2.1	Toward nadir (HRIC, VIHI)	PERIHELION	$\nu_M = 0°$
3.3.2.2	Forward along track (+20° STC)		
3.3.2.3	Backward along track (-20° STC)		
3.3.2.4	Toward nadir (HRIC, VIHI)	APHELION	$\nu_M = 180°$
3.3.2.5	Forward along track (+20° STC)		
3.3.2.6	Backward along track (-20° STC)		
3.3.2.7	Toward nadir (HRIC, VIHI)	AUTUMN/SPRING	$\nu_M = 90°$
3.3.2.8	Forward along track (+20° STC)		
3.3.2.9	Backward along track (-20° STC)		

Table 3.5

The most significant graphs and numerical results are reported in the following paragraphs. More detailed results and other analysis cases can be found in [10].

3.3.2.1 PERIHELION – surface normal pointing toward nadir (HRIC, VIHI)

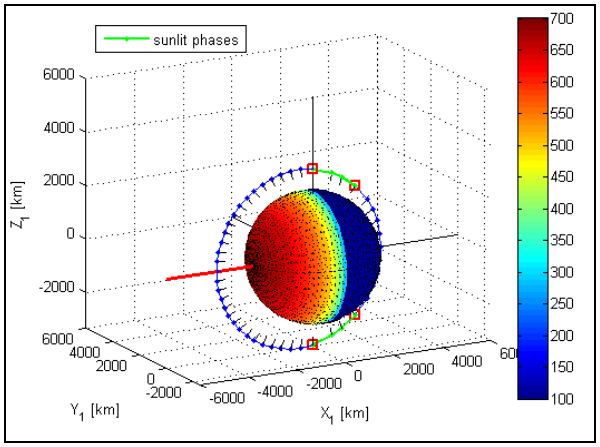

Figure 3.30: *A 3D view of the planet at **perihelion** and the orbit of the S/C. In the bar on the right the relationship between the colors and the temperature of the planet [K]. The green lines plots the portion of the orbit during which the surface (nadir pointing) is illuminated by the Sun. The red line shows the vector from the planet toward the Sun.*

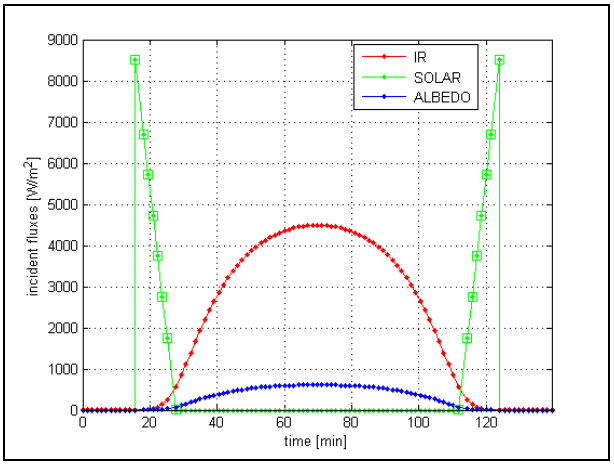

Figure 3.31: *The solar, albedo and IR planetary fluxes incident on a nadir pointing surface (HRIC, VIHI) are plotted as a function of time (S/C orbit). A green box indicates non zero values of solar flux. Mercury is at **perihelion***

The most significant data are reported in the following table:

Solar Constant = 14490.0 W/m^2 @ $\nu_M = 0°$ (Perihelion)				
Max Mercury surface Temperature = 688.6 K				
SOLAR FLUX – SUNLIT PHASE 1				
		time t	Sun incidence angle θ_{SUN}	S/C true anomaly ν
Start at		15.5 min	54.0°	54.0°
End at		27.7 min	90.0°	90.0°
Sunlit duration Δt		12.2 min		
Max of solar flux	**8509.5 W/m^2**			
SOLAR FLUX – SUNLIT PHASE 2				
		time t	Sun incidence angle θ_{SUN}	S/C true anomaly ν
Start at		111.8 min	90.0°	270.0°
End at		124.0 min	54.0°	306.0°
Sunlit duration Δt		12.2 min		
Max of solar flux	**8509.5 W/m^2**			
IR PLANETARY FLUX				
	Heat flux	time t	Sun incidence angle θ_{SUN}	S/C true anomaly ν
Max of IR planetary flux	**4496.1 W/m^2**	69.8 min	180.0° (no sunlit)	180.0° (no sunlit)
ALBEDO FLUX				
	Heat flux	time t	Sun incidence angle θ_{SUN}	S/C true anomaly ν
Maximum albedo flux	**613.2 W/m^2**	69.8 min	180.0° (no sunlit)	180.0° (no sunlit)

Table 3.6

3.3.2.2 PERIHELION – surface normal pointing +20° forward along track (STC/H)

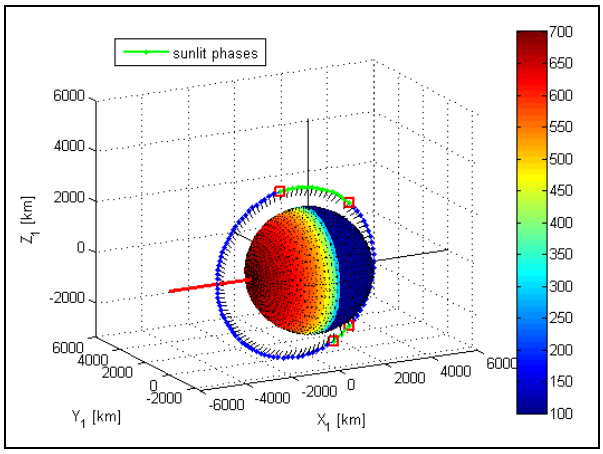

Figure 3.32: *A 3D view of the planet at **perihelion** and the orbit of the S/C. In the bar on the right the relationship between the colors and the temperature of the planet [K]. The green lines plots the portion of the orbit during which the surface (forward pointing) is illuminated by the Sun. The red line shows the vector from the planet toward the Sun.*

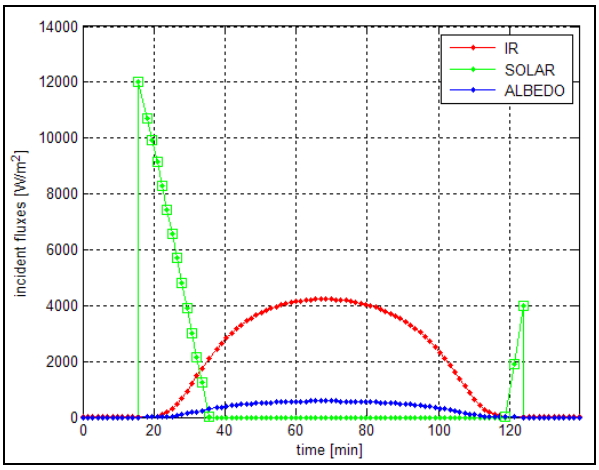

Figure 3.33: *The solar, albedo and IR planetary fluxes incident on a surface pointing +20° forward along track (STC) are plotted as a function of time (S/C orbit). A green box indicates non zero values of solar flux. Mercury is at **perihelion**.*

The most significant data are reported in the following table:

Solar Constant = 14490.0 W/m^2 @ $\nu_M = 0°$ (Perihelion)				
Max Mercury surface Temperature = 688.6 K				
SOLAR FLUX – SUNLIT PHASE 1				
		time t	Sun incidence angle θ_{SUN}	S/C true anomaly ν
Start at		15.5 min	34.0°	54.0°
End at		35.5 min	90°	110.0°
Sunlit duration Δt		20.1 min		
Max of solar flux	**12007.5 W/m^2**			
SOLAR FLUX – SUNLIT PHASE 2				
		time t	Sun incidence angle θ_{SUN}	S/C true anomaly ν
Start at		118.9 min	90.0°	290.0°
End at		124.0 min	74.0°	306.0°
Sunlit duration Δt		5.1 min		
Max of solar flux	**3985.0 W/m^2**			
IR PLANETARY FLUX				
	Heat flux	time t	Sun incidence angle θ_{SUN}	S/C true anomaly ν
Max of IR planetary flux	**4230.2 W/m^2**	68.4 min	157.4° (no sunlit)	177.4°
ALBEDO FLUX				
	Heat flux	time t	Sun incidence angle θ_{SUN}	S/C true anomaly ν
Maximum albedo flux	**576.9 W/m^2**	68.4 min	157.4° (no sunlit)	177.4°

Table 3.7

3.3.2.3 PERIHELION – surface normal pointing -20° backward along track (STC/L)

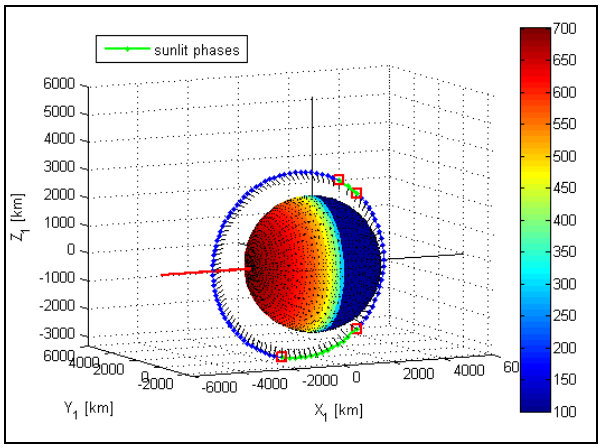

Figure 3.34: *A 3D view of the planet at **perihelion** and the orbit of the S/C. In the bar on the right the relationship between the colors and the temperature of the planet [K]. The green lines plots the portion of the orbit during which the surface (backward pointing) is illuminated by the Sun. The red line shows the vector from the planet toward the Sun.*

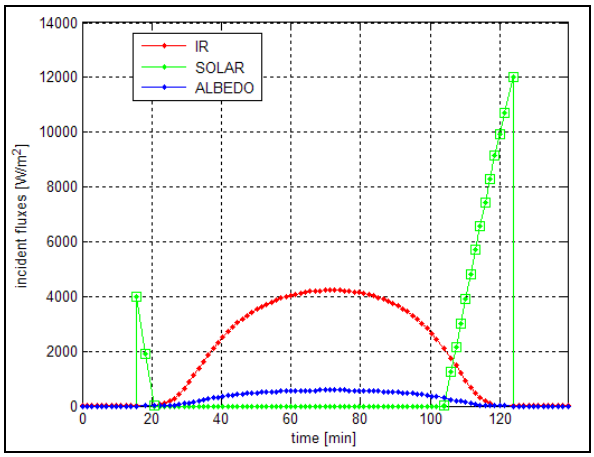

Figure 3.35: *The solar, albedo and IR planetary fluxes incident on a surface pointing -20° backward along track (STC) are plotted as a function of time (S/C orbit). A green box indicates non zero values of solar flux. Mercury is at **perihelion**.*

The most significant data are reported in the following table:

Solar Constant = 14490.0 W/m^2 @ $\nu_M = 0°$ (Perihelion)				
Max Mercury surface Temperature = 688.6 K				
SOLAR FLUX – SUNLIT PHASE 1				
		time t	Sun incidence angle θ_{SUN}	S/C true anomaly ν
Start at		15.5 min	74.0°	54.0°
End at		20.6 min	90.0°	90.0°
Sunlit duration Δt		5.1 min		
Max of solar flux	**3985.0 W/m^2**			
SOLAR FLUX – SUNLIT PHASE 2				
		time t	Sun incidence angle θ_{SUN}	S/C true anomaly ν
Start at		104.0 min	90.0°	250.0°
End at		124.0 min	34.0°	306.0°
Sunlit duration Δt		20.1 min		
Max of solar flux	**12007.5 W/m^2**			
IR PLANETARY FLUX				
	Heat flux	time t	Sun incidence angle θ_{SUN}	S/C true anomaly ν
Max of IR planetary flux	**4230.2 W/m^2**	71.1 min	157.4° (no sunlit)	182.6°
ALBEDO FLUX				
	Heat flux	time t	Sun incidence angle θ_{SUN}	S/C true anomaly ν
Maximum albedo flux	**576.9 W/m^2**	71.1 min	157.4° (no sunlit)	182.6°

Table 3.8

3.3.2.4 APHELION – surface normal pointing toward nadir (HRIC, VIHI)

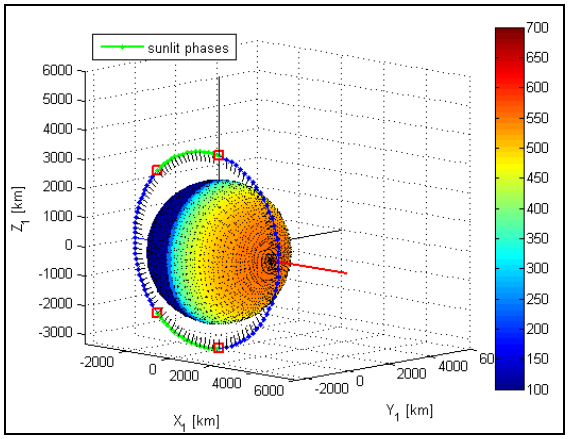

Figure 3.36: *A 3D view of the planet at* ***aphelion*** *and the orbit of the S/C. In the bar on the right the relationship between the colors and the temperature of the planet [K]. The green lines plots the portion of the orbit during which the surface (nadir pointing) is illuminated by the Sun. The red line shows the vector from the planet toward the Sun.*

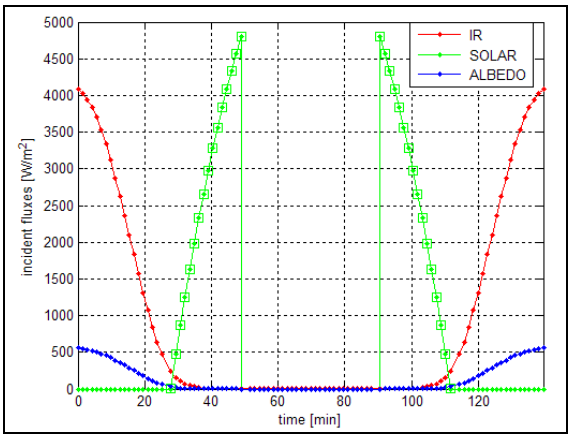

Figure 3.37: *The solar, albedo and IR planetary fluxes incident on a nadir pointing surface (HRIC, VIHI) are plotted as a function of time (S/C orbit). A green box indicates non zero values of solar flux. Mercury is at* ***aphelion***

The most significant data are reported in the following table:

Solar Constant = 6290.5 W/m^2 @ $\nu_M = 180°$ (Aphelion)				
Max Mercury surface Temperature = 559.0 K				
SOLAR FLUX – SUNLIT PHASE 1				
		time t	Sun incidence angle θ_{SUN}	S/C true anomaly ν
Start at		27.7 min	90.0°	90.0°
End at		49.0 min	40.3°	139.7°
Sunlit duration Δt		21.3 min		
Max of solar flux	**4798.4 W/m^2**			
SOLAR FLUX – SUNLIT PHASE 2				
		time t	Sun incidence angle θ_{SUN}	S/C true anomaly ν
Start at		90.5 min	40.3°	220.3°
End at		111.9 min	90.0°	270.0°
Sunlit duration Δt		21.3 min		
Max of solar flux	**4798.4 W/m^2**			
IR PLANETARY FLUX				
	Heat flux	time t	Sun incidence angle θ_{SUN}	S/C true anomaly ν
Max of IR planetary flux	**4087.4 W/m^2**	0 min (139.5 min)	180.0° (no sunlit)	0° (360°)
ALBEDO FLUX				
	Heat flux	time t	Sun incidence angle θ_{SUN}	S/C true anomaly ν
Maximum albedo flux	**557.5 W/m^2**	0 min (139.5 min)	180° (no sunlit)	0° (360°)

Table 3.9

3.3.2.5 APHELION – surface normal pointing +20° forward along track (STC/H)

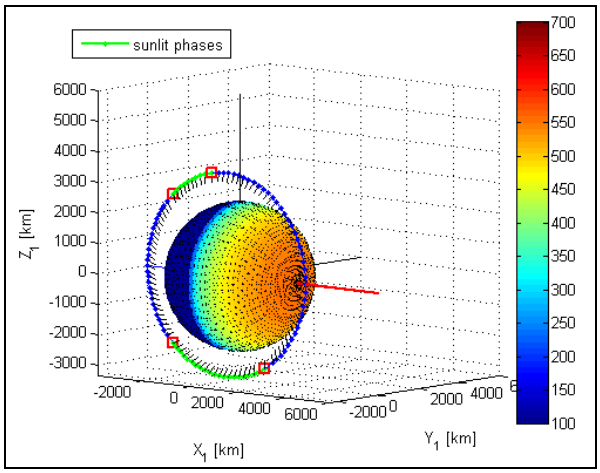

Figure 3.38: *A 3D view of the planet at* ***aphelion*** *and the orbit of the S/C. In the bar on the right the relationship between the colors and the temperature of the planet [K]. The green lines plots the portion of the orbit during which the surface (forward pointing) is illuminated by the Sun. The red line shows the vector from the planet toward the Sun.*

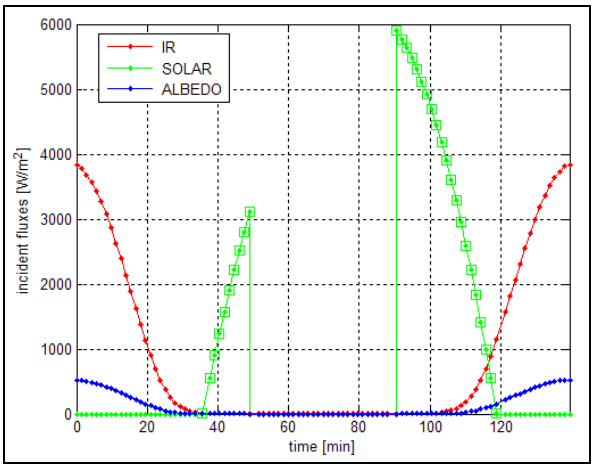

Figure 3.39: *The solar, albedo and IR planetary fluxes incident on a surface pointing +20° forward along track (STC) are plotted as a function of time (S/C orbit). A green box indicates non zero values of solar flux. Mercury is at* ***aphelion****.*

The most significant data are reported in the following table:

Solar Constant = 6290.5 W/m^2 @ $\nu_M = 180°$ (Aphelion)				
Max Mercury surface Temperature = 559.0 K				
SOLAR FLUX – SUNLIT PHASE 1				
		time t	Sun incidence angle θ_{SUN}	S/C true anomaly ν
Start at		35.6 min	90.0°	110.0°
End at		49.0 min	60.3°	139.7°
Sunlit duration Δt		13.4 min		
Max of solar flux	**3117.8 W/m^2**			
SOLAR FLUX – SUNLIT PHASE 2				
		time t	Sun incidence angle θ_{SUN}	S/C true anomaly ν
Start at		90.5 min	20.3°	220.3°
End at		118.9 min	90.0°	290.0°
Sunlit duration Δt		28.4 min		
Max of solar flux	**5900.3 W/m^2**			
IR PLANETARY FLUX				
	Heat flux	time t	Sun incidence angle θ_{SUN}	S/C true anomaly ν
Max of IR planetary flux	**3840.9 W/m^2**	0 min (139.5 min)	160° (no sunlit)	0° (360°)
ALBEDO FLUX				
	Heat flux	time t	Sun incidence angle θ_{SUN}	S/C true anomaly ν
Maximum albedo flux	**523.8 W/m^2**	0 min (139.5 min)	160° (no sunlit)	0° (360°)

Table 3.10

3.3.2.6 APHELION – surface normal pointing -20° backward along track (STC/L)

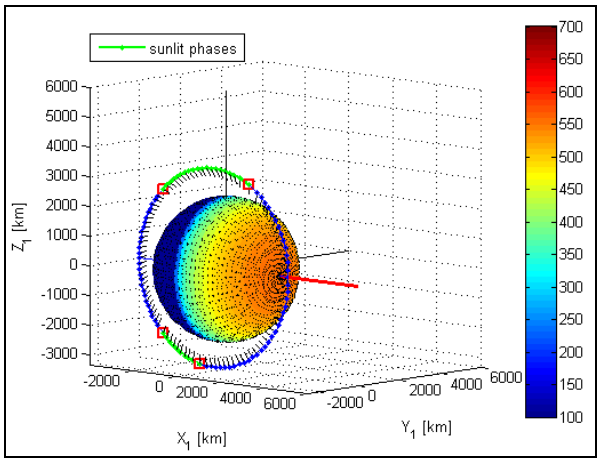

Figure 3.40: *A 3D view of the planet at* ***aphelion*** *and the orbit of the S/C. In the bar on the right the relationship between the colors and the temperature of the planet [K]. The green lines plots the portion of the orbit during which the surface (backward pointing) is illuminated by the Sun. The red line shows the vector from the planet toward the Sun.*

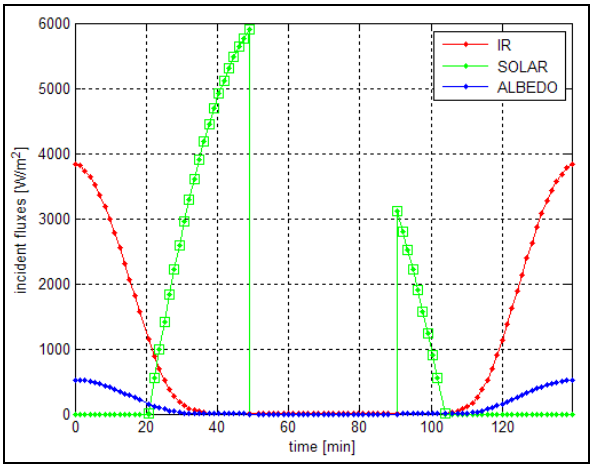

Figure 3.41: *The solar, albedo and IR planetary fluxes incident on a surface pointing -20° backward along track (STC) are plotted as a function of time (S/C orbit). A green box indicates non zero values of solar flux. Mercury is at* ***aphelion****.*

The most significant data are reported in the following table:

Solar Constant = 6290.5 W/m^2 @ $\nu_M = 180°$ (Aphelion)				
Max Mercury surface Temperature = 559.0 K				
SOLAR FLUX – SUNLIT PHASE 1				
		time t	Sun incidence angle θ_{SUN}	S/C true anomaly ν
Start at		20.6 min	90.0°	90.0°
End at		49.0 min	20.3°	139.7°
Sunlit duration Δt		28.4 min		
Max of solar flux	**5900.3 W/m^2**			
SOLAR FLUX – SUNLIT PHASE 2				
		time t	Sun incidence angle θ_{SUN}	S/C true anomaly ν
Start at		90.5 min	60.3°	220.3°
End at		104.0 min	90.0°	250.0°
Sunlit duration Δt		13.5 min		
Max of solar flux	**3117.8 W/m^2**			
IR PLANETARY FLUX				
	Heat flux	time t	Sun incidence angle θ_{SUN}	S/C true anomaly ν
Max of IR planetary flux	**3840.9 W/m^2**	0 min (139.5 min)	160° (no sunlit)	0° (360°)
ALBEDO FLUX				
	Heat flux	time t	Sun incidence angle θ_{SUN}	S/C true anomaly ν
Maximum albedo flux	**523.8 W/m^2**	0 min (139.5 min)	160° (no sunlit)	0° (360°)

Table 3.11

3.3.2.7 AUTUMN/SPRING – surface normal pointing toward nadir (HRIC, VIHI)

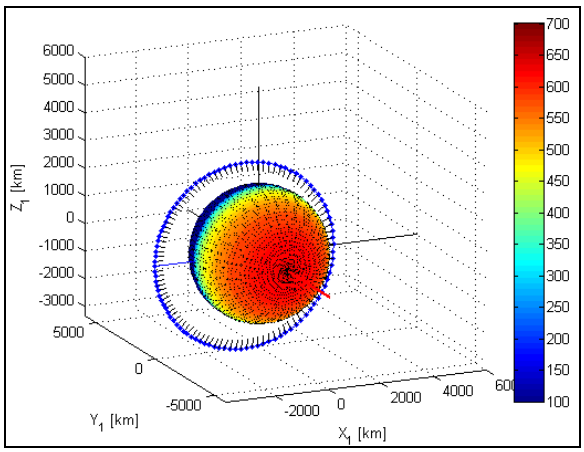

Figure 3.42: *A 3D view of the planet at **autumn/spring** and the orbit of the S/C. In the bar on the right the relationship between the colours and the temperature of the planet [K]. It must be noticed that no S/C eclipse transition nor telescope shadowing occurs. The red line shows the vector from the planet toward the Sun.*

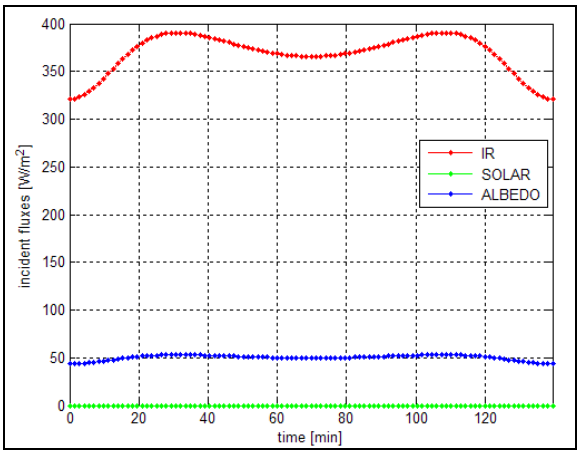

Figure 3.43: *The solar, albedo and IR planetary fluxes incident on a nadir pointing surface (HRIC/VIHI) are plotted as a function of time (S/C orbit). Mercury is at **autumn/spring**. It must be noticed that there are no incident solar fluxes throughout the orbit because the Sun direction is perpendicular to the S/C orbital plane.*

The most significant data are reported in the following table:

Solar Constant = 9968.7 W/m^2 @ $\nu_M = 90°$ (Autumn/Spring)				
Max Mercury surface Temperature = 627.1 K				
SOLAR FLUXES				
There are NO incident solar fluxes throughout the orbit				
No S/C eclipse transition; Sun vector perpendicular to the S/C orbital plane				
IR PLANETARY FLUX				
	Heat flux	time t	Sun incidence angle θ_{SUN}	S/C true anomaly ν
Max of IR planetary flux	**390.6 W/m^2**	32.1 min (107.4 min)	90.0° (no sunlit)	101.5° (258.5°)
ALBEDO FLUX				
	Heat flux	time t	Sun incidence angle θ_{SUN}	S/C true anomaly ν
Maximum albedo flux	**53.1 W/m^2**	32.1 min (107.4 min)	90.0° (no sunlit)	101.5° (258.5°)

Table 3.12

3.3.2.8 AUTUMN/SPRING – surface normal pointing +20° forward along track (STC/H)

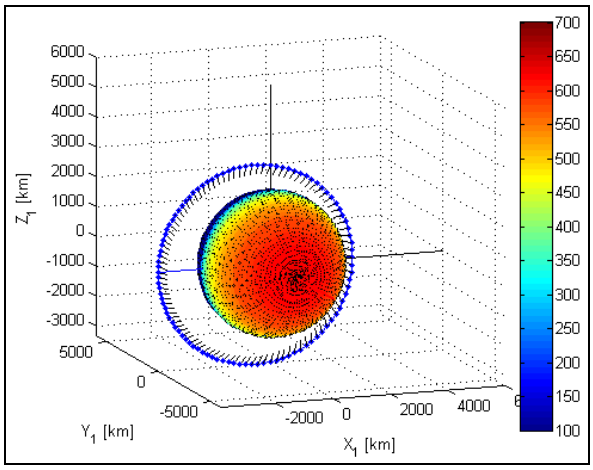

Figure 3.44: *A 3D view of the planet at **autumn/spring** and the orbit of the S/C. In the bar on the right the relationship between the colors and the temperature of the planet [K]. It must be noticed that no S/C eclipse transition nor telescope shadowing occurs. The red line shows the vector from the planet toward the Sun.*

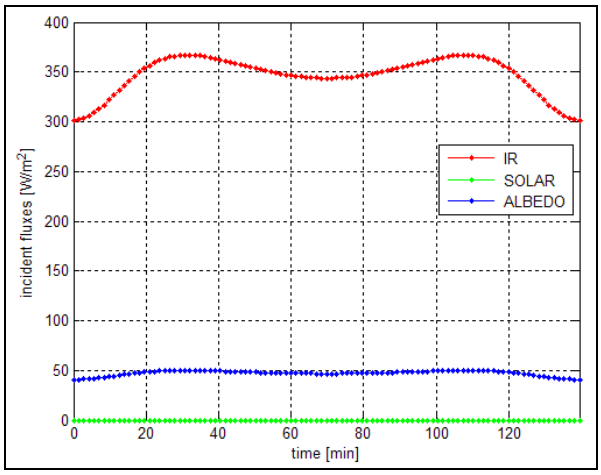

Figure 3.45: *The solar, albedo and IR planetary fluxes incident on a surface pointing +20° forward along track (STC) are plotted as a function of time. Mercury is at **autumn/spring**. It must be noticed that there are no incident solar fluxes throughout the orbit because the Sun direction is perpendicular to the S/C orbital plane.*

The most significant data are reported in the following table:

Solar Constant = 9968.7 W/m^2 @ $\nu_M = 90°$ (Autumn/Spring)				
Max Mercury surface Temperature = 627.1 K				
SOLAR FLUXES				
There are NO incident solar fluxes throughout the orbit				
No S/C eclipse transition; Sun vector perpendicular to the S/C orbital plane				
IR PLANETARY FLUX				
	Heat flux	time t	Sun incidence angle θ_{SUN}	S/C true anomaly ν
Max of IR planetary flux	**367.1 W/m^2**	32.1 min (107.4 min)	90.0° (no sunlit)	101.5° (258.5°)
ALBEDO FLUX				
	Heat flux	time t	Sun incidence angle θ_{SUN}	S/C true anomaly ν
Maximum albedo flux	**49.9 W/m^2**	32.1 min (107.4 min)	90.0°	101.5° (258.5°)

Table 3.13

3.3.2.9 AUTUMN/SPRING – surface normal pointing -20° backward along track (STC/L)

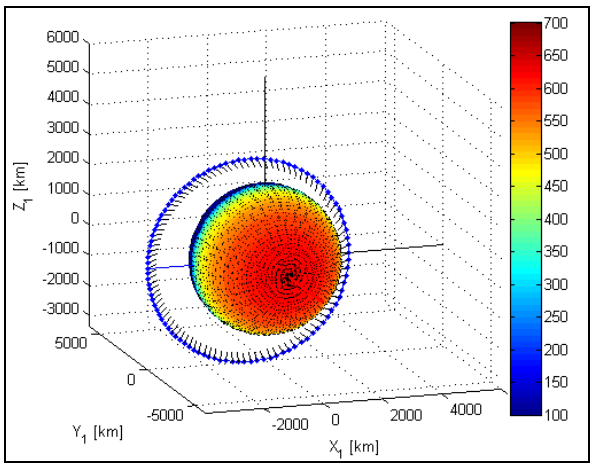

Figure 3.46: *A 3D view of the planet at **autumn/spring** and the orbit of the S/C. In the bar on the right the relationship between the colors and the temperature of the planet [K]. It must be noticed that no S/C eclipse transition nor telescope shadowing occurs. The red line shows the vector from the planet toward the Sun.*

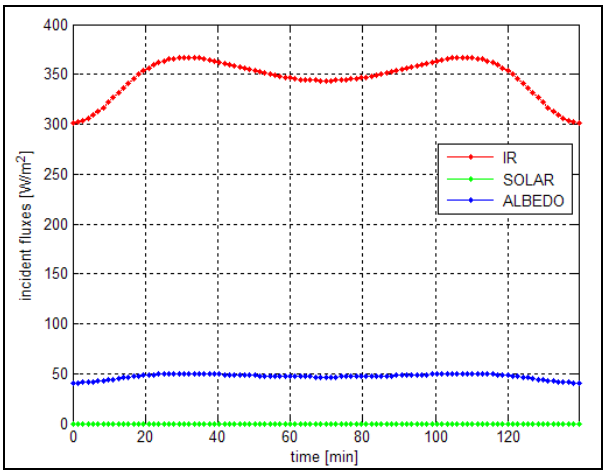

Figure 3.47: *The solar, albedo and IR planetary fluxes incident on a surface pointing +20° forward along track (STC) are plotted as a function of time. Mercury is at **autumn/spring**. It must be noticed that there are no incident solar fluxes throughout the orbit because the Sun direction is perpendicular to the S/C orbital plane.*

The most significant data are reported in the following table:

Solar Constant = 9968.7 W/m^2 @ $\nu_M = 90°$ (Autumn/Spring)				
Max Mercury surface Temperature = 627.1 K				
SOLAR FLUXES				
There are NO incident solar fluxes throughout the orbit				
No S/C eclipse transition; Sun vector perpendicular to the S/C orbital plane				
IR PLANETARY FLUX				
	Heat flux	time t	Sun incidence angle θ_{SUN}	S/C true anomaly ν
Max of IR planetary flux	**367.1 W/m^2**	32.1 min (107.4 min)	90.0° (no sunlit)	101.5° (258.5°)
ALBEDO FLUX				
	Heat flux	time t	Sun incidence angle θ_{SUN}	S/C true anomaly ν
Maximum albedo flux	**49.9 W/m^2**	32.1 min (107.4 min)	90.0°	101.5° (258.5°)

Table 3.14

4 SUN INCIDENCE ANGLE ASSESSMENT DURING BEPICOLOMBO MISSION

In this chapter will be presented some results regarding the evaluation of the Sun incidence angle θ_{SUN} during BepiColombo mission. The purpose of this analysis is to evaluate how the Sun rays are seen by the instruments orbiting around Mercury. Furthermore, by calculating the minimum of the Sun incidence angle , it could be computed the limit angle at which the instrument will see directly the Sun rays.

Let us recall that the Sun incidence angle is defined as the angle between the normal $\mathbf{n}_T$ to the considered surface $d\mathbf{A}_T$ and the Sun rays direction $\mathbf{n}_{SUN}$, as defined by equation (80) and illustrated in Figure 3.15 , hereafter reported for simplicity of reading.

$$\theta_{SUN} = \arccos\left(\mathbf{n}_T \cdot \mathbf{n}_{SUN}\right) \tag{80}$$

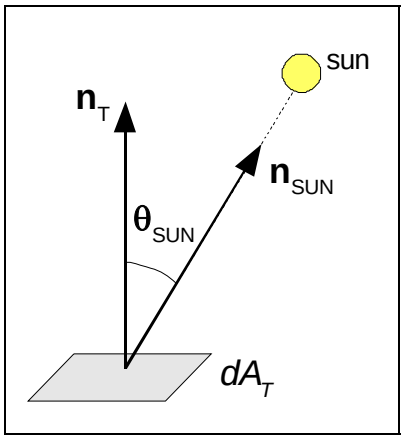

Figure 3.15

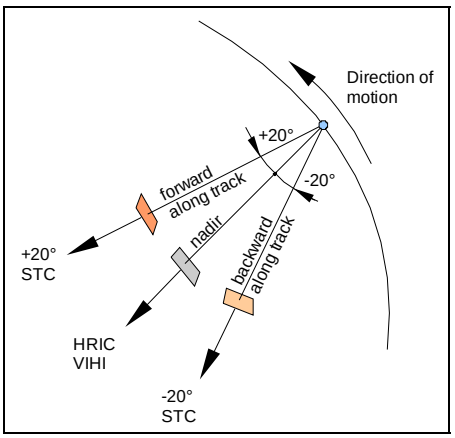

Figure 3.19

For the design of the SIMBIO-SYS optical instruments orbiting around Mercury, it is important to evaluate the minima values of the Sun incidence angle θ_{SUN} for which a direct Sun illumination of the focal plane could occur. Furthermore the knowledge of the behavior of the angle θ_{SUN} during mission is an important input parameter for the design of the instrument baffles.

In this contest, the interest is focused on evaluating the angle between the Sun direction and the optical axes of the instruments, as in Figure 3.19. The versors $\mathbf{n}_T$ used for the analysis are therefore:

- a surface normal nadir pointing, which corresponds to the HRIC and VIHI optical axes
- a surface normal pointing +20° forward along track, which corresponds to one of the eyes of STC
- a surface normal pointing -20° backward along track, which corresponds to the other eye of STC

To evaluate the criticality of direct Sun illumination it has been calculated the minimum angle between the Sun direction and the channel's axis as a function of Mercury season.

For each value of Mercury position with respect to the Sun (Mercury anomaly ν_M), the minimum value of the Sun incidence angle among the sunlit phases of the S/C orbit has been calculated and plotted as a function of ν_M (***Figure 4.1***). Then the minimum value of these minima, called $\theta_{SUN,\min}$ is calculated and the corresponding Mercury season ν_M is computed. This values corresponds to the most critical condition for the Sun incidence angle during the whole mission.

During the sunlit phases, the value of the solar incidence angle θ_{SUN} must belong to the interval $0° \le \theta_{SUN} \le 90°$. If solar illumination does not occur, this value is set to 90°. The orbital parameters used in the simulation are reported in Table 4.1 , which corresponds to reference orbit (see [1]).

INPUT DATA	
MERCURY ORBIT AROUND MERCURY	
ν_M **= from 0° to 180° (increment = 0.5°)**	**position of the planet: true anomaly of Mercury (season)**
S/C ORBIT AROUND MERCURY	
N_{time} **= 100**	**time among half S/C orbit (from perigee to apogee)**
Ω **= 0°**	**RAAN**
i_0 **= 90°**	**inclination**
ω_p = 0° (ref. orbit)	argument of periherm
h_a = 1508 km	apoherm altitude ha
h_p = 400 km	periherm altitude hp
S/C attitude (NADIR pointing)	
ψ **= 0°**	**yaw angle**
θ **= 0°**	**pitch angle**
ϕ **= 0°**	**roll angle**
OPTICAL AXIS	
α_{INSTR} = 0°	HRIC/VIHI, nadir pointing
α_{INSTR} = +20°	STC , +20° forward along track
α_{INSTR} = -20°	STC , -20° backward along track

Table 4.1

The simulation lead to the graph reported in Figure 4.1 from which it can be find out the most critical condition with regard to direct Sun illumination of the instrument axes among the overall mission. The numerical data are reported in Table 4.2 .

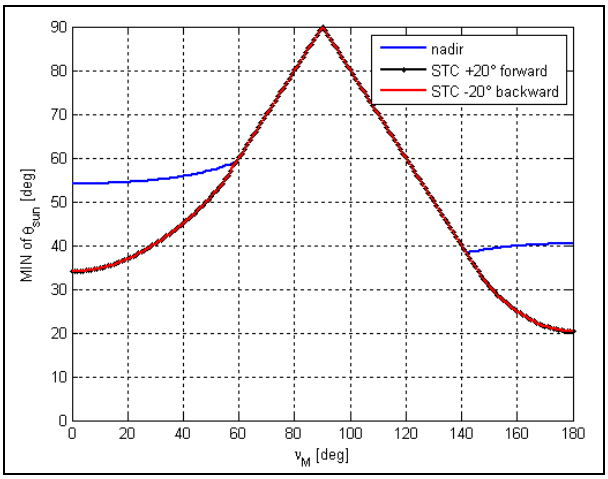

Figure 4.1: the minimum of Sun incidence angle θ_{SUN} is plotted as a function of Mercury seasons ν_M

Instrument	**Minimum Sun incidence angle $\theta_{SUN,\min}$**	**Mercury season $\nu_{M,\min}$**	**Notes**
HRIC, VIHI (nadir pointing)	38.2°	141.8°	Transition to eclipse season
STC /H (+20° forward along track)	20.3°	180.0°	Aphelion
STC /L (-20° back along track)	20.3	180.0°	Aphelion

Table 4.2: minimum values of Sun incidence angle for SIMBIO-SYS channels and the corresponding season at which the critical condition occurs (reference S/C orbit)

From Figure 4.1 and Table 4.2 table it must be acknowledged that, for nadir pointing instruments (HRIC and VIHI), the minimum Sun incidence occurs at the Mercury position corresponding to the transition to apoherm eclipse seasons ($\nu_M = 141.8°$) that corresponds to the cusp point of blue line in Figure 4.1. On the other hand, for instruments pointing off-nadir in the orbit plane (i.e. STC +/-20° along track) the minimum Sun incidence occurs at aphelion. The former (HRIC, VIHI) will see directly the Sun rays with incidence greater than 38.4°, the latter (STC) will see directly the Sun rays with incidence greater than 20.2°.

4.1 Analysis of the effect of orbit evolution on Sun Incidence angle

Due to the J2 perturbation, the argument of periherm ω_p is moving during the operational phases around Mercury with time at a rate of 33º/year for J2 =60 10^{-6} from the time of arrival at Mercury up-to the end of mission [7]. The reference orbit value of ω_p = 0° , analyzed in the previous chapter, shall be crossed during the first year of the mission.

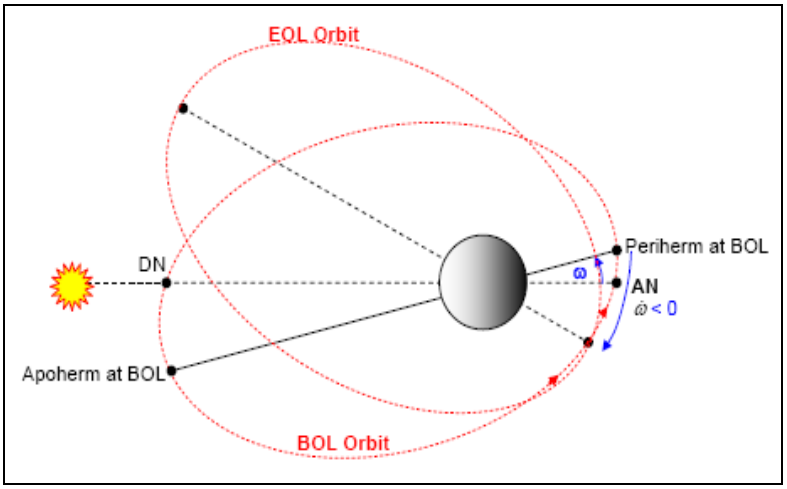

Figure 4.2: outline of orbit evolution due to J2 (from [7].)

To evaluate the effects of orbit evolution on Sun incidence angle, the following cases (Table 4.3) has been analyzed, as indicated in [7]. The orbital and physical parameters other than those indicated in Table 4.3 are taken from Table 3.2, Table 3.3 and Table 4.1.

	BOL	**REF**	**J2_nom**	**J2_25m**
	Mercury approach	Reference orbit	End of nominal mission	End of extended mission
h_a [km]	1508	1508	1506	1475
h_p [km]	400	400	402	433
i_0 [deg]	90	90	90	90
ω_p [deg]	+16	0	-20	-53

Table 4.3:Analysis cases to evaluate the J2 effects on orbital parameters during mission

The results of the analysis are reported in the following paragraphs.

4.1.1 Sun incidence angle on HRIC and VIHI channels

The cases indicated in *Table 4.3* have been analyzed in order to estimate the effect of orbit evolution during BepiColombo mission on minimum value of Sun incidence angle. The results of simulations for the nadir pointing channels HRIC and VIHI are reported in Figure 4.3 and Table 4.4.

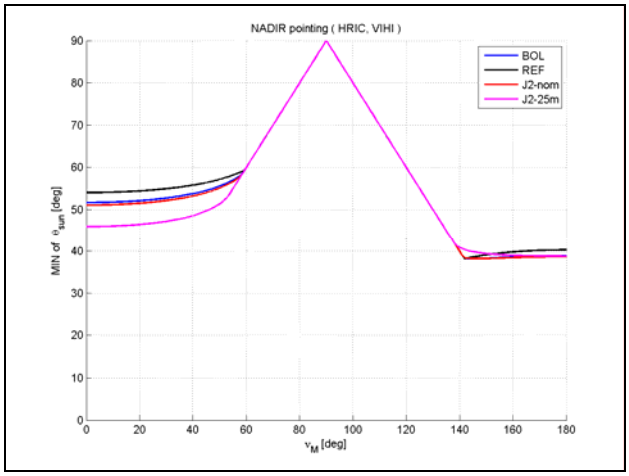

Figure 4.3: *effect of S/C orbit evolution due to J2 on minimum Sun incidence angle as function of Mercury seasons. HRIC and VIHI nadir pointing channels.*

Minimum values of Sun incidence angle HRIC, VIHI nadir pointing α_{INSTR} = 0°				
	BOL Mercury approach	**REF** Reference orbit	**J2_nom** End of nominal mission	**J2_25m** End of extended mission
$\theta_{SUN,\min}$	38.2°	38.2°	38.2°	38.8°
$\nu_{M,\min}$	144.9°	141.8°	146.8°	180.0°

Table 4.4: *effect of S/C orbit evolution due to J2 on minimum Sun incidence angle. HRIC and VIHI nadir pointing channels.*

It could be seen from Table 4.4 that, for HRIC and VIHI channels, the S/C orbit evolution during mission does not worsen the critical value of the Sun incidence angle.

A value of $\theta_{SUN,\min} = 38.2°$ can be taken as the input design constraint value for the design and sizing of HRIC and VIHI baffles.

4.1.2 Sun incidence angle on STC +20° forward along track sub-channel

The cases indicated in *Table 4.3* have been analyzed in order to estimate the effect of orbit evolution during BepiColombo mission on minimum value of Sun incidence angle. The results of simulations for the STC sub-channel pointing forward along track are reported in Figure 4.4 and Table 4.5.

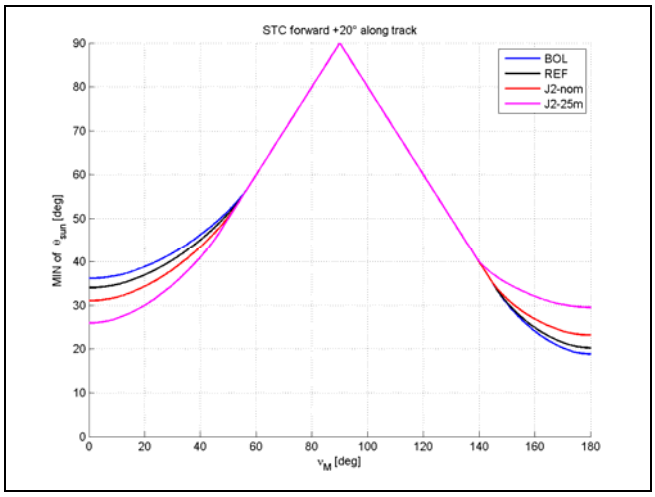

Figure 4.4: *effect of S/C orbit evolution due to J2 on minimum Sun incidence angle as function of Mercury seasons. STC subchannel pointing +20° forward along track*

Minimum values of Sun incidence angle STC forward along track α_{INSTR} = + 20°				
	BOL Mercury approach	**REF** Reference orbit	**J2_nom** End of nominal mission	**J2_25m** End of extended mission, 25 months
$\theta_{SUN,\min}$	18.9°	20.3°	23.2°	25.9°
$\nu_{M,\min}$	180°	180°	180°	0°

Table 4.5: effect of S/C orbit evolution due to J2 on minimum Sun incidence angle. STC subchannel pointing +20° forward along track

It could be seen from ***Table 4.5*** and **Figure 4.4** that, for the STC sub-channel, the S/C orbit evolution during mission affect the critical value of the Sun incidence angle and a new, worse critical value is found out at the beginning of operative mission (BOL).

4.1.3 Sun incidence angle on STC -20° backward along track sub-channel

The cases indicated in *Table 4.3* have been analyzed in order to estimate the effect of orbit evolution during BepiColombo mission on minimum value of Sun incidence angle. The results of simulations for the STC sub-channel pointing backward along track are reported in Figure 4.5 and Table 4.6.

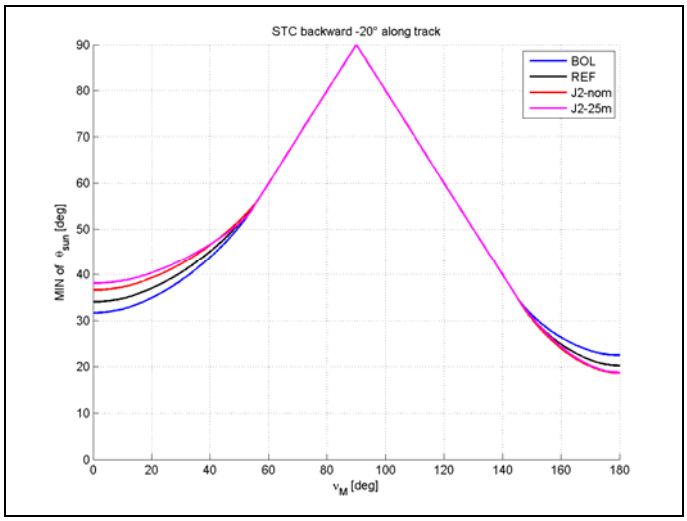

Figure 4.5: *effect of S/C orbit evolution due to J2 on minimum Sun incidence angle as function of Mercury seasons. STC subchannel pointing -20° backward along track*

Minimum values of Sun incidence angle STC backward along track α_{INSTR} = - 20°				
	BOL Mercury approach	**REF** Reference orbit	**J2_nom** End of nominal mission	**J2_25m** End of extended mission, 25 months
$\theta_{SUN,\min}$	22.5°	20.3°	18.7°	18.8°
$\nu_{M,\min}$	180°	180°	180°	180°

Table 4.6: *effect of S/C orbit evolution due to J2 on minimum Sun incidence angle. STC subchannel pointing -20° backward along track*

It could be seen in Figure 4.5 and Table 4.6 that, for the STC sub-channel, the S/C orbit evolution during mission affect the critical value of the Sun incidence angle and new, worse critical values are found out at the end of nominal mission (J2_nom) and at the end of the extended mission (J2_25m).

4.2 Solar disk subtended angle

Let us recall that the mathematical model developed in this thesis work, it has been made the hypothesis that the Sun rays have direction parallel to the direction from the Sun to the position of the considered surface, then the finite spherical shape of the Sun has not been taken into account.

It must be underlined that the mathematical model used herein (see chapter 3.2) does not takes into account the finite size dimension of the Sun. Because of the finite size of the Sun and due to the vicinity of Mercury to the Sun, the Sun's rays at Mercury are not quite parallel. In fact the solar disk subtends and angle that varies along the Mercury orbit within perihelion and aphelion extremes [7].

The solar disc subtended angle has been calculated as follows.
At perihelion the distance Mercury-Sun is equal to:

$$r_{M\_PH} = r\left(\nu_M = 0°\right) = 4.60 \cdot 10^7 \; km \tag{91}$$

at aphelion the distance Mercury-Sun is equal to:

$$r_{M\_AH} = r\left(\nu_M = 180°\right) = 6.98 \cdot 10^7 \; km \tag{92}$$

The radius of the Sun is:

$$R_{SUN} = 6.96 \cdot 10^5 \; km \tag{93}$$

Then the solar disc subtended angle varies within the following extremes:

$$\alpha_{SUN\_PH} = \arcsin\left(\frac{R_{SUN}}{r_{M\_PH}}\right) = 0.87° \tag{94}$$

$$\alpha_{SUN\_AH} = \arcsin\left(\frac{R_{SUN}}{r_{M\_AH}}\right) = 0.57° \tag{95}$$

Then we have [7]:

Solar disk subtended angle at Mercury aphelion:	1.14°
Solar disk subtended angle at Mercury perihelion:	1.73°

The angle α_{SUN} can be computed also for intermediate Mercury season and will be used for baffle verification to direct Sun illumination.

5 DIRECT SUN ILLUMINATION ANALYSIS AND VERIFICATION OF SIMBIO-SYS BAFFLES GEOMETRY

5.1 HRIC Stavroudis Baffle Geometry Verification

The geometry of HRIC Stavroudis baffle current configuration and main dimensions are sketched in Figure 5.1 :

Diameter of aperture of baffle: *Dap* = 104.6 mm

Length of baffle: *L* = 230.8 mm

and then the cut-off angle of the baffle is calculated as:

HRIC cut-off angle: $\beta_{HRIC} = \arctan\left(\frac{Dap}{L}\right) = 24.4°$

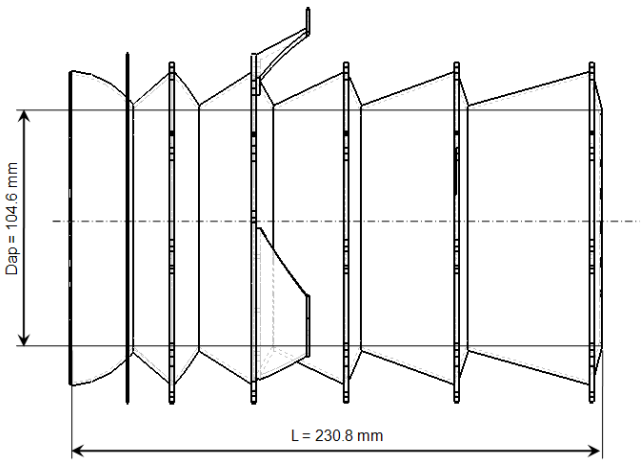

Figure 5.1: HRIC Stavroudis baffle

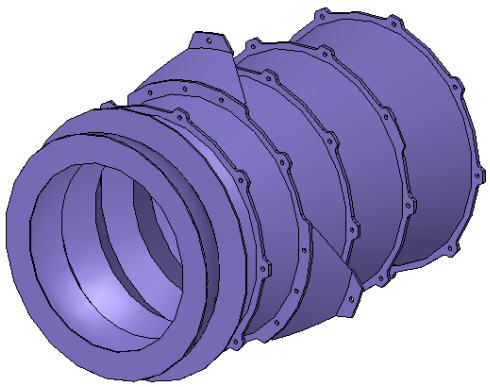

Figure 5.2: HRIC Stavroudis baffle

Given the axial symmetry of the baffle, to verify the geometry of the baffle against direct Sun illumination during mission, the value of the cut-off angle β_{HRIC} must be compared with the value of minimum sun incidence angle $\theta_{SUN,\min}$ previously calculated for the HRIC channel and reported in Table 4.4. To take into account also the solar disk finite dimension, the angle $\alpha_{SUN,PH}$ at perihelion has been considered for angular margin calculation. Even though the solar disk subtended angle $\alpha_{SUN,PH}$ does not correspond to value of α_{SUN} at the Mercury season at which the Sun incidence reaches the minimum $\theta_{SUN,\min}$, this is the maximum value of α_{SUN} and then it will be used for verification purposes.

HRIC Stavroudis baffle verification	
$\theta_{SUN,\min}$	38.2°
α_{SUN_PH}	0.87°
β_{HRIC}	24.4°
$\delta_{MARGIN} = \left(\theta_{SUN,\min} - \alpha_{SUN,\max}\right) - \beta_{HRIC}$	**12.9°**

Table 5.1

The HRIC Stavroudis baffle geometry has an angular margin against direct Sun illumination during mission equal to $\delta_{MARGIN} = 12.9°$. This value can be considered safe enough against direct Sun illumination during nominal phases of BepiColombo mission.

5.2 VIIHI Baffle Geometry Verification

The geometry of VIHI baffle current configuration and the main dimensions are sketched in Figure 5.3, Figure 5.4 and Figure 5.5. In this case the aperture of the baffle is rectangular and the axial symmetry is not valid in this case. The cut-off angle calculation is obtained by some geometrical remarks on the dimensions of frontal and back vane aperture of the baffle. The following dimensions of baffle are given:

Baffle Frontal vane aperture	$A_1 \times B_1 = 25.13 \times 43.42$ mm
Baffle Back vane aperture	$A_2 \times B_2 = 25.10 \times 33.77$ mm
Length of the baffle	$L = 150.1$ mm

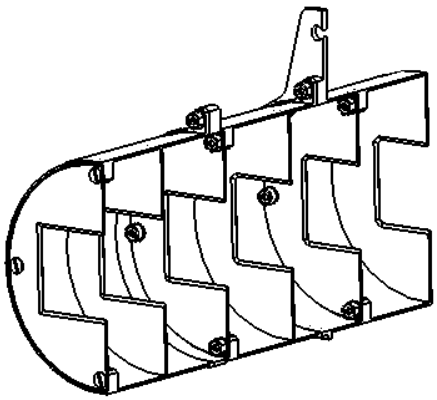

Figure 5.3: VIHI baffle section (symmetry plane)

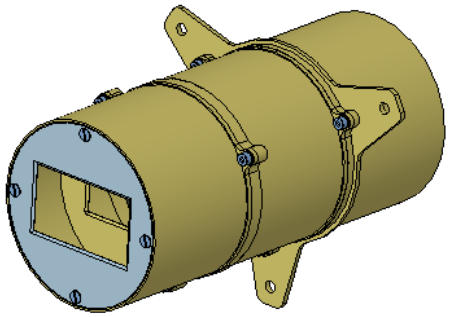

Figure 5.4: VIHI baffle 3D view

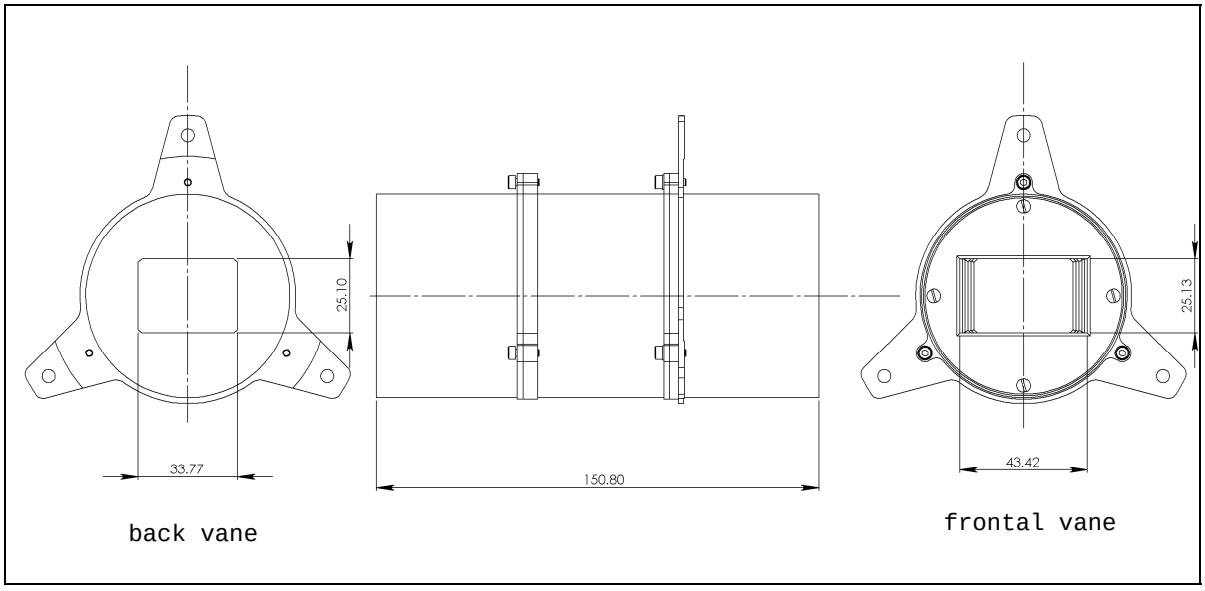

Figure 5.5: VIHI baffle geometry and main dimensions

Let us calculate the quantities:

$A = A_2 + \frac{A_1 - A_2}{2} = 25.115$ mm , $B = B_2 + \frac{B_1 - B_2}{2} = 38.595$ mm , $D = \sqrt{A^2 + B^2} = 46.047$ mm

Then the VIHI baffle cut-off angle is computed as follows:

VIHI cut-off angle: $\beta_{VIHI} = \arctan\left(\frac{D}{L}\right) = 17.1°$

To verify the geometry of the baffle against direct Sun illumination during mission, the value of the cut-off angle β_{VIHI} will be compared with the value of minimum Sun incidence angle $\theta_{SUN,\min}$ previously calculated for the VIHI channel and reported in Table 4.4. To take into account also the solar disk finite dimension, the subtended angle $\alpha_{SUN,PH}$ at perihelion – which is the maximum value of α_{SUN} during mission - has been considered for angular margin calculation.

Even though the solar disk subtended angle $\alpha_{SUN,PH}$ does not correspond to the value of α_{SUN} corresponding to the Mercury season at which the Sun incidence reaches the minimum $\theta_{SUN,\min}$, this is the maximum value of α_{SUN} and then it will be used for verification purposes. Furthermore the cut-off angle β_{VIHI} is the maximum angular value of acceptance of incoming rays but does not correspond to the Sun rays direction at Aphelion, to which we have the minimum Sun incidence angle $\theta_{SUN,\min}$. It must be noticed that, for verification purposes, if we compare the previously defined angles to calculate the angular margin (as in **Table 5.2**) and if a positive value of δ_{MARGIN} is obtained, we know for certain that the angular margin against direct Sun illumination is at least equal to δ_{MARGIN}.

VIHI Stavroudis baffle verification	
$\theta_{SUN,\min}$	38.2°
α_{SUN_PH}	0.87°
β_{VIHI}	17.1°
$\delta_{MARGIN} = \left(\theta_{SUN,\min} - \alpha_{SUN,\max}\right) - \beta_{VIHI}$	**20.2°**

Table 5.2

The VIHI baffle geometry has an angular margin against direct Sun illumination during mission equal to $\delta_{MARGIN} = 20.2°$. This value can be considered safe enough against direct Sun illumination during nominal phases of BepiColombo mission.

5.3 STC Baffle Geometry Verification

The geometry of STC baffles of the current configuration to be verified is shown in **Figure 5.6** and **Figure 5.7** .

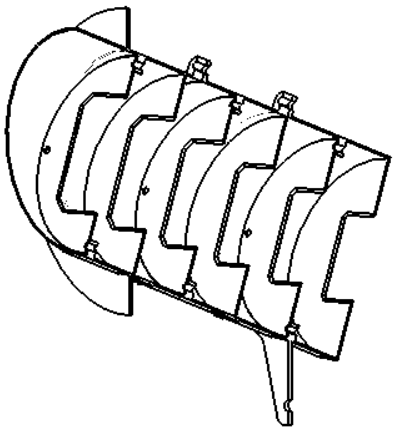

Figure 5.6: STC baffle

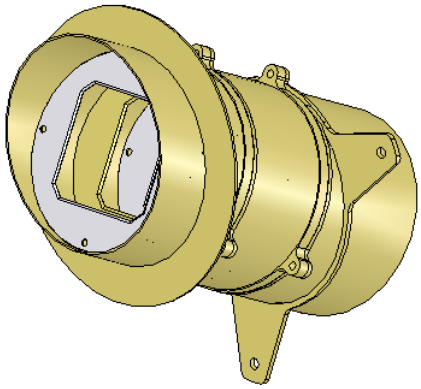

Figure 5.7: STC baffle

The aperture of baffle has rectangular shape and the axial symmetry is not valid in this case. The cut-off angle calculation is obtained by some geometrical remarks on the dimensions of frontal and back vane aperture of the baffle. We have:

Baffle Frontal vane aperture	$A_1 \times B_1 = 44.23 \times 44.65$ mm
Baffle Back vane aperture	$A_2 \times B_2 = 32.26 \times 31.30$ mm
Length of the baffle	$L = 132.0$ mm

Let us calculate the quantities:

$$A = A_2 + \frac{A_1 - A_2}{2} = 38.245 \text{ mm} \ , \ B = B_2 + \frac{B_1 - B_2}{2} = 37.975 \text{ mm} , \ D = \sqrt{A^2 + B^2} = 53.896 \text{ mm}$$

Then the STC baffle maximum cut-off angle is computed as follows:

STC cut-off angle: $$\beta_{STC} = \arctan\left(\frac{D}{L}\right) = 22.2°$$

It is important to notice that this value is bigger than the minimum value of Sun incidence angle $\theta_{SUN,\min}$ calculated for the STC sub-channels and reported in Table 4.5 and in Table 4.6 . This does not necessarily means that Sun will enter the baffle; in fact the minimum Sun incidence angle $\theta_{SUN,\min}$ occurs at Aphelion at the eclipse entry/exit point. In this situation the incident Sun rays lies on the symmetry plane of the baffle and, in this case, the cut-off angle of the baffle can be computed as follows:

STC cut-off angle (Aphelion): $$\beta_{STC,AH} = \arctan\left(\frac{A}{L}\right) = 16.2°$$

Even though the value $\beta_{STC,AH}$ is smaller than the $\theta_{SUN,\min}$ calculated and reported in Table 4.5 and Table 4.6, it could be possible that, at some other condition during the mission, the Sun incidence angle could be smaller than acceptance of the baffle. Furthermore the angle $\beta_{STC,AH}$ is a rough approximation of the cut-off angle of the baffle because the effect of the frontal protrusion of the baffle has not taken into account.

Due to the criticality of this issue, a more detailed analysis must be performed for the verification of the baffle geometry to direct Sun rays entry and some geometric modification will be proposed to overcome the problem. The analysis method is described below.

Ray casting algorithms has been implemented in Matlab software using the 3D geometry of the baffles to accurately analyze the most critical cases of Sun rays direct entry into STC baffles.
The geometry of baffle to be verified is shown in Figure 5.8, where it could be seen the frontal and back vanes with the polygonal aperture, the sloping rectangle corresponding to S/C plane and the edge of the baffle cylinder on the S/C plane.
Thanks to the results of the simulations already performed, the Sun direction is known at each position of the MPO spacecraft during mission and the components of the versor N_{sun} during mission has been expressed in a reference frame fixed with baffle.
Solar rays will be casted from a point R_0 at the corner of baffle aperture on the back vane and with direction N_{sun}. Using ray-object intersection algorithms used for computer graphics application (see [11], [12], [13]), the interception points of solar rays with the S/C plane has been computed and, within them, only the points internal to the rectangle are taken away and plotted in Figure 5.8. The limitation to the rectangular frontal plane interception points reduce the number of points interested in the subsequent computations and greatly reduce the computational cost.
The position of point R_0 has been chosen such that it represents the worst case for the rays to pass through the baffle.
For each ray $r(R_0, N_{sun})$ it is computed the solar disk subtended angle α_{SUN} corresponding to the Mercury true anomaly ν_M and a cone of rays with aperture α_{SUN} and axis of revolution N_{sun} is casted from point R_0; this set of rays of the cone is denoted as: $c_R(R_0, N_{sun}, \alpha_{SUN})$. The intersection curve of the rays of the cones on the S/C plane is plotted (see yellow curves in Figure 5.9).
For each vane of the baffle are calculated the intersection points of the rays of the cone $c_R(R_0, N_{sun}, \alpha_{SUN})$ with the vane plane and the inner and outer points to the vane aperture are computed.

At this point it is found out if there are some cone $c_R(R_0, N_{sun}, \alpha_{SUN})$ for which at **least one solar ray pass through the vanes of the baffle** to reach the point R_0.

If this ray exist, then some solar rays could pass through the baffle and the baffle geometry must be modified.

If **no solar rays pass through the baffle**, then an angular margin $\boxed{\delta_{MARGIN}}$ must be computed. For each ray $r(R_0, N_{sun})$ a new cone of rays $c_R\left(R_0, N_{sun}, \left(\alpha_{SUN} + \delta\right)\right)$ is computed, with vertex R_0, axis of direction N_{sun}, aperture angle $\left(\alpha_{SUN} + \delta\right)$ and incremental angle $\delta > 0°$. A mathematical function has been implemented to find out the value of the angle $\delta = \bar{\delta}$ such that there exist at least one ray of the cone $c_R\left(R_0, N_{sun}, \left(\alpha_{SUN} + \bar{\delta}\right)\right)$ that pass through the baffle. In other words, this means that there exist at least one ray of the cone $c_R\left(R_0, N_{sun}, \left(\alpha_{SUN} + \bar{\delta}\right)\right)$ for which all the intersection points of the ray with the vanes lie in the inner side of the aperture of the vane.

Once the values of the angle $\overline{\delta}$ has been found for each solar ray $r(R_0, N_{sun})$, the minimum value of $\overline{\delta}$ is computed and the angular margin δ_{MARGIN} is then given by: $\delta_{MARGIN} = \min\left\{\overline{\delta}\right\}$. Once the angular margin δ_{MARGIN} has been found, it can be computed the corresponding value of Mercury season (anomaly ν_M), the value of solar disk subtended angle α_{SUN}, the Sun incidence angle θ_{SUN} between the solar ray and the axis of the baffle and the position of the S/C during orbit around the planet. The geometric meaning of the above defined quantities is illustrated in *Figure 5.9* and the angular margin could be also defined as: $\delta_{MARGIN} = P_2\widehat{R_0}P_3$ while the solar disk subtended angle could be defined as $\alpha_{SUN} = P_3\widehat{R_0}P_1$.

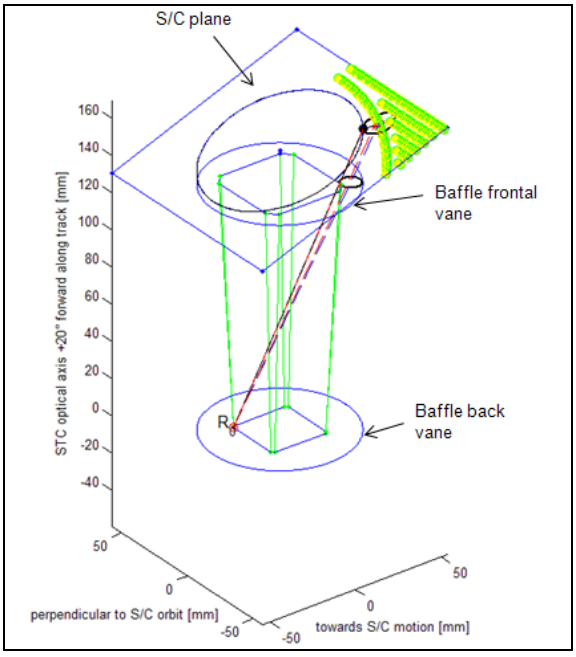

Figure 5.8: STC baffle geometry: starting configuraton. Analysis to direct Sun illumination

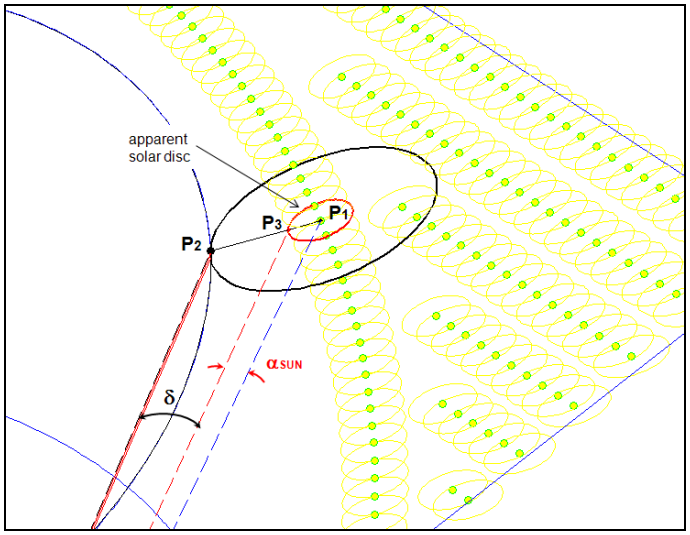

Figure 5.9: STC baffle geometry verification to Sun rays direct entry. Detailed view of critical Sun illumination condition.

The results of simulation performed on the STC baffle geometry configuration in Figure 5.7 and *Figure 5.8* are presented below.

The analysis have been performed for each of the two subchannels of STC baffle and considering the four set of S/C orbital parameter indicated in ***Table 4.3*** to take into account the evolution of MPO orbit around Mercury during BepiColombo mission.

The analysis of STC baffle of subchannel looking +20° forward along track leads to the results reported in the following ***Table 5.3***

Minima values of Sun incidence angle STC forward along track $\alpha_{INSTR} = +20°$				
Rays casted from R0 = corner at the aperture of the back vane of baffle				
	BOL	**REF**	**J2_nom**	**J2_25m**
	Mercury approach	Reference orbit	End of nominal mission	End of extended mission, 25 months
δ_{MARGIN}	**0.2°**	**1.4°**	**4.2°**	**7.2°**
ν_M	167°	166.5°	165.5°	14.5°
α_{SUN}	0.58°	0.58°	0.58°	0.86°
VERIFICATION	**NO rays enter**	**NO rays enter**	**NO rays enter**	**NO rays enter**

Table 5.3: angular margin to Sun rays entry STC + 20° baffle (starting configuration)

The analysis of STC baffle of subchannel looking -20° backward along track leads to the results reported in the following Table 5.4 .

Minima values of Sun incidence angle STC backward along track $\alpha_{INSTR} = -20°$				
Rays casted from R0 = corner at the aperture of the back vane of baffle				
	BOL	**REF**	**J2_nom**	**J2_25m**
	Mercury approach	Reference orbit	End of nominal mission	End of extended mission, 25 months
δ_{MARGIN}	**3.5°**	**1.4°**	**< 0**	**0.2°**
ν_M	166°	166.5°	167°	167°
α_{SUN}	0.58°	0.58°	0.58°	0.58°
VERIFICATION	**NO rays enter**	**NO rays enter**	**RAYS ENTER**	**NO rays enter**

Table 5.4: angular margin to Sun rays entry STC - 20° baffle (starting configuration)

The simulation shows that the STC geometry actually is not suitable to avoid direct entry of solar rays. It could be seen from Table 5.4 that there will be at least one season where solar rays directly pass through the baffle; this event occurs for STC -20° backward subchannel at the end of nominal mission (J2_nom); this event is graphed in ***Figure 5.10***.

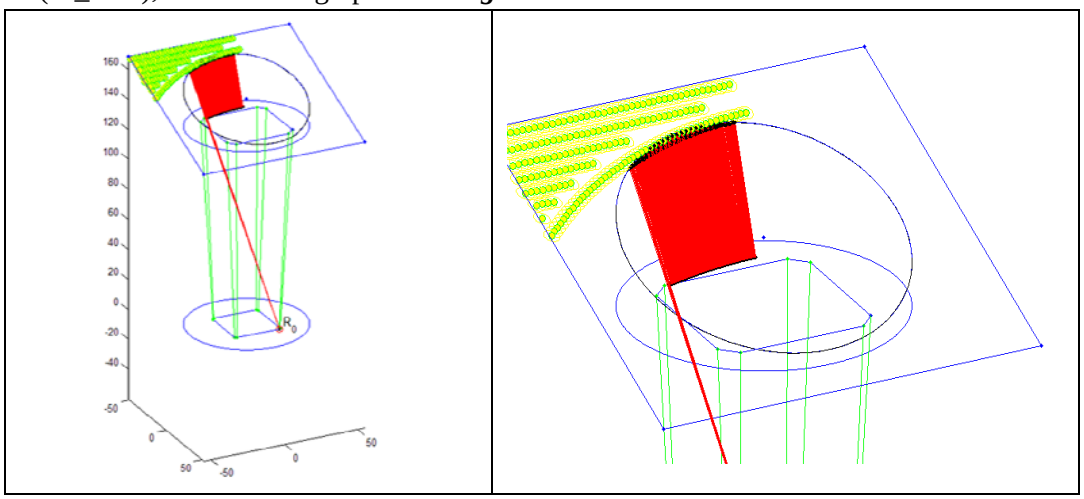

Figure 5.10: STC - 20° baffle at end of nominal mission. Starting configuration; solar rays pass through the baffle

Moreover it must be noticed (Table 5.3, Table 5.4) that the angular margin δ_{MARGIN}, although positive, is extremely narrow also for other operative phases of the mission. This force to find a different geometry for STC baffle to avoid the direct solar illumination.

To overcome this issue two main baffle design modification were introduced by the SIMBIO-SYS team and illustrated in Figure 5.11 and Figure 5.12:

- A frontal ring has been added to increase the cutoff angle
- Two additional vanes has been added, separated by the main baffle structure and mounted on the main honeycomb structure of the instrument nearby the telescope entrance.

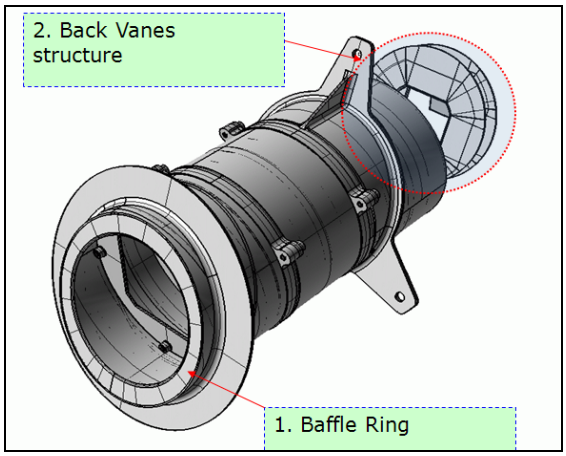

Figure 5.11: STC baffle modified configuration

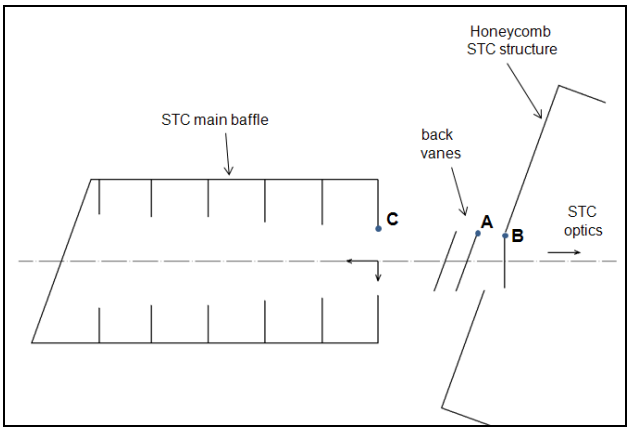

Figure 5.12: *STC baffle modified configuration*

Several simulations has been performed on the modified geometry using the same approach described above. For this new geometrical configuration the rays will be casted from three points R_0 defined in Figure 5.12.
Three different conditions have then been analyzed:

- $\boxed{R_0 = A}$: it lies at the corner of the aperture of the innermost back vane. Sun rays reaching point A could be scattered and enter the STC optical system
- $\boxed{R_0 = B}$: it lies at the corner of a surface representing the aperture of the STC optical system. Sun rays reaching point B could directly enter the STC optical system
- $\boxed{R_0 = C}$: it lies at the corner of the aperture of the back vane of the main baffle. Sun rays reaching point C will enter the volume amid the baffles and the instrument and could be scattered and enter the STC optical system

With the two additional back vane, the baffling system has been modified such that the new reference point for the verification of the baffle will be the point A. The verification of rays casted from point C will be performed anyway to evaluate if there exist some angular margin to avoid direct entry of solar rays through the main baffle and also to estimate the advantage coming from the introduction of the frontal ring.
The verification of rays casted from point B will give the information about the possibility of Sun rays to reach directly the telescope aperture and then the scientific field of view of the instrument.

The results of simulations are presented in the following tables

ANALYSIS RESULTS : Sun rays casted from point $R_0 = A$

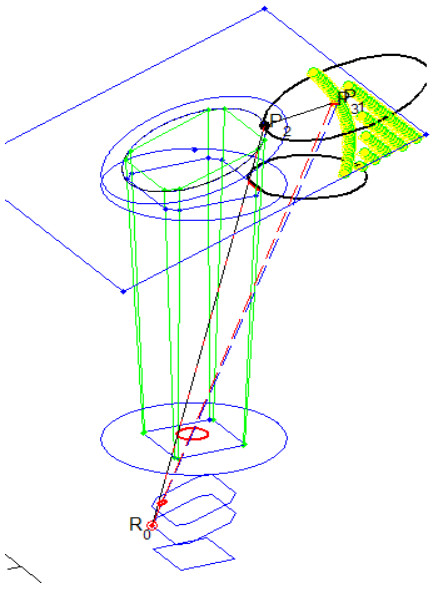

Criticality of Sun incidence **STC forward along track** $\alpha_{INSTR} = +20°$				
Rays casted from point R0 = A				
	BOL Mercury approach	**REF** Reference orbit	**J2_nom** End of nominal mission	**J2_25m** End of extended mission
δ_{MARGIN}	**6.4°**	**7.7°**	**10.6°**	**13.2°**
ν_M	172.5°	173°	172°	7.5°
α_{SUN}	0.57°	0.57°	0.57°	0.87°
θ_{SUN}	19.6°	20.9°	23.8°	26.5°
$\nu_{S/C}$ (*)	202.2°	219.7°	242.5°	98.5°
CHECK	**NO rays enter**	**NO rays enter**	**NO rays enter**	**NO rays enter**

(*) minimum values of sun incidence angle occurs at eclipse entry/exit points of MPO orbit

Table 5.5: angular margin to solar rays entering point A. STC + 20° baffle (modified configuration)

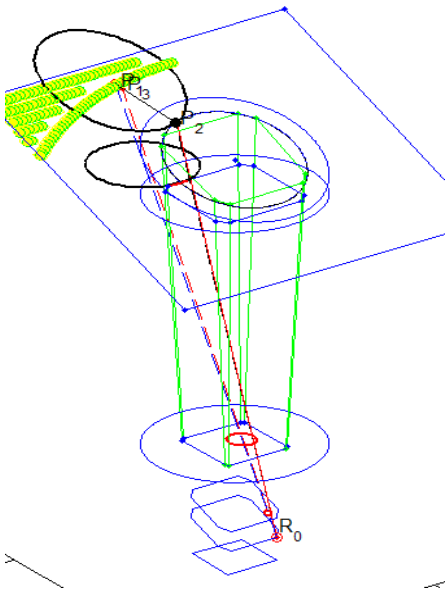

Criticality of Sun incidence **STC backward along track** $\alpha_{INSTR} = -20°$				
Rays casted from point R0 = A				
	BOL Mercury approach	**REF** Reference orbit	**J2_nom** End of nominal mission	**J2_25m** End of extended mission
δ_{MARGIN}	**9.9°**	**7.7°**	**6.2°**	**6.3°**
ν_M	172°	173°	172.5°	173°
α_{SUN}	0.57°	0.57°	0.57°	0.57°
θ_{SUN}	23.1°	20.9°	19.5°	19.5°
$\nu_{S/C}$ (*)	122.2°	140.3°	162.0°	194.7°
CHECK	**NO rays enter**	**NO rays enter**	**NO rays enter**	**NO rays enter**

(*) minimum values of sun incidence angle occurs at eclipse entry/exit points of MPO orbit

Table 5.6: angular margin to solar rays entering point A. STC - 20° baffle (modified configuration)

ANALYSIS RESULTS : Sun rays casted from point $R_0 = B$

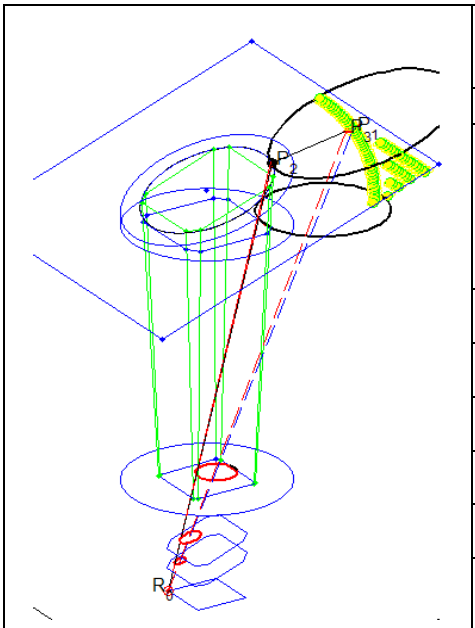

Criticality of Sun incidence
STC forward along track $\alpha_{INSTR} = +20°$

Rays casted from point R0 = B

	BOL Mercury approach	**REF** Reference orbit	**J2_nom** End of nominal mission	**J2_25m** End of extended mission
δ_{MARGIN}	**7.4°**	**8.8°**	**11.6°**	**14.2°**
ν_M	172.5°	172°	172°	8.5°
α_{SUN}	0.57°	0.57°	0.57°	0.87°
θ_{SUN}	19.6°	21.1°	23.8°	26.7°
$\nu_{S/C}$ (*)	202.2°	219.5°	242.5°	98.4°
CHECK	**NO rays enter**	**NO rays enter**	**NO rays enter**	**NO rays enter**

(*) minimum values of sun incidence angle occurs at eclipse entry/exit points of MPO orbit

Table 5.7: *angular margin to solar rays entering point B. STC + 20° baffle (modified configuration)*

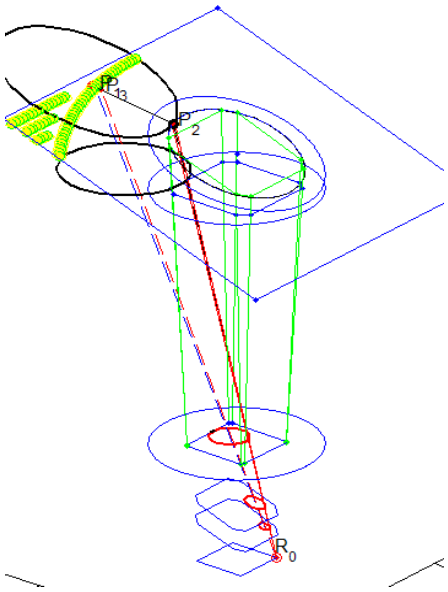

Criticality of Sun incidence
STC forward along track $\alpha_{INSTR} = -20°$

Rays casted from point R0 = B

	BOL Mercury approach	**REF** Reference orbit	**J2_nom** End of nominal mission	**J2_25m** End of extended mission
δ_{MARGIN}	**10.9°**	**8.8°**	**7.2°**	**7.4°**
ν_M	172°	172°	172.5°	172.5°
α_{SUN}	0.57°	0.57°	0.57°	0.57°
θ_{SUN}	23.1°	21.1°	19.5°	19.6°
$\nu_{S/C}$ (*)	122.2°	140.5°	162.0°	194.8°
CHECK	**NO rays enter**	**NO rays enter**	**NO rays enter**	**NO rays enter**

(*) minimum values of sun incidence angle occurs at eclipse entry/exit points of MPO orbit

Table 5.8: *angular margin to solar rays entering point B. STC - 20° baffle (modified configuration)*

ANALYSIS RESULTS: Sun rays casted from point $\boxed{R_0 = C}$

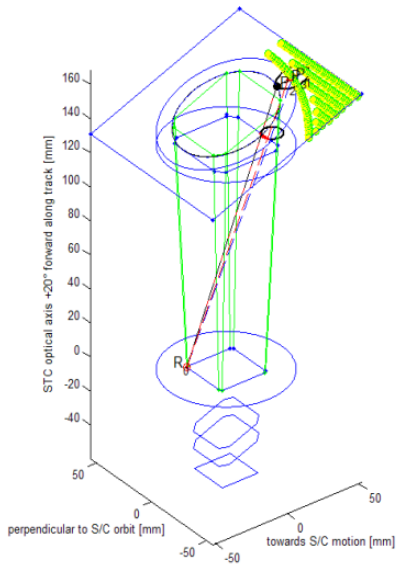

Criticality of Sun incidence
STC forward along track $\alpha_{INSTR} = +20°$

Rays casted from point R0 = C

	BOL Mercury approach	**REF** Reference orbit	**J2_nom** End of nominal mission	**J2_25m** End of extended mission
δ_{MARGIN}	**2.0°**	**3.4°**	**6.2°**	**8.8°**
ν_M	171.5°	170.5°	170.5°	7°
α_{SUN}	0.57°	0.57°	0.57°	0.87°
θ_{SUN}	19.9°	21.4°	24.0°	26.5°
$\nu_{S/C}$ (*)	202.0°	219.2°	242.2°	98.6°
CHECK	**NO rays enter**	**NO rays enter**	**NO rays enter**	**NO rays enter**

(*) minimum values of sun incidence angle occurs at eclipse entry/exit points of MPO orbit

Table 5.9: *angular margin to solar rays entering point C. STC + 20° baffle (modified configuration)*

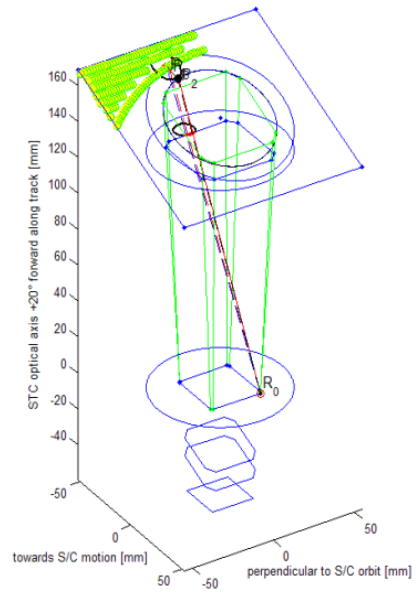

Criticality of Sun incidence
STC forward along track $\alpha_{INSTR} = -20°$

Rays casted from point R0 = A

	BOL Mercury approach	**REF** Reference orbit	**J2_nom** End of nominal mission	**J2_25m** End of extended mission
δ_{MARGIN}	**5.5°**	**3.4°**	**1.8°**	**2.0°**
ν_M	171°	170.5°	171.5°	171.5°
α_{SUN}	0.57°	0.57°	0.57°	0.57°
θ_{SUN}	23.3°	21.4	19.7°	19.9°
$\nu_{S/C}$ (*)	122.4	140.8	162.2°	195.0°
CHECK	**NO rays enter**	**NO rays enter**	**NO rays enter**	**NO rays enter**

(*) minimum values of sun incidence angle occurs at eclipse entry/exit points of MPO orbit

Table 5.10: *angular margin to solar rays entering point C. STC - 20° baffle (modified configuration)*

The modified geometry of STC baffles increase the angular margin against direct passing of solar rays through the baffling system equal to $\delta_{MARGIN} = 6.2°$. This value can be considered safe enough against direct Sun illumination during nominal phases of BepiColombo mission.

6 THERMAL ANALYSIS OF SIMBIO-SYS BAFFLES

6.1 Description of SIMBIO-SYS baffles and thermal analysis methods

The thermal environment that the SIMBIO-SYS scientific package will face during BepiColombo mission has been analyzed in the previous chapter 3 and quantitative results has been provided. The results quantify how severe will be the thermal environment during mission at Mercury and the most critical thermal cases has been identified.
The three optical channels HRIC, VIHI and STC will see directly the external environment through the baffle aperture then appropriate thermo-optical design for the baffling system of the instrument is a demanding task. The baffling of the payload will assume a crucial role for thermal control of the SIMBIO-SYS suite and detailed and appropriate thermal models must be performed to support thermal control system design.

The thermal model and interfaces of three units (HRIC, VIHI, STC) follows the scheme reported in the following Figure 6.1 (see [3]).

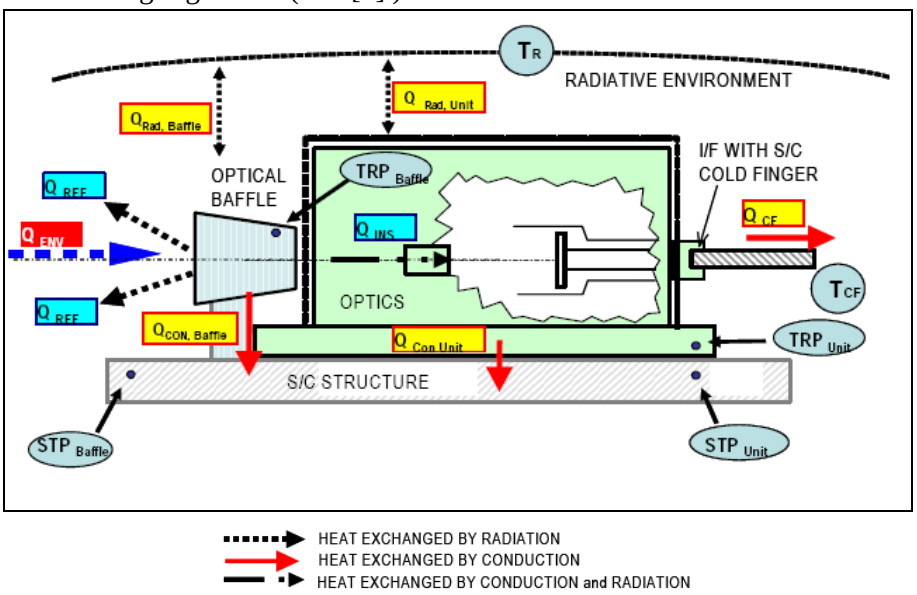

Figure 6.1: scheme of unit thermal interfaces (from ref. [3])

It could be recognized the optics of the unit (green box) and the baffle (grey box). It is important to notice that the baffles and the optics are conductively decoupled in order to reduce the heat load to the telescope optics. Furthermore different thermal interfaces are foreseen for baffles and optics.
Following the graphics above the definition of fluxes is derived:

- The environmental thermal inputs are described by the parameter Q_{ENV}, which is mainly dependent of the aperture size of the baffle and the actual environment
- Instrument will reject part of the heat input by reflection and by re-emission of absorbed heat directly to space, which is mainly dependent of the heat rejection capability of the baffle. This heat flux is described by the parameter Q_{REF}
- The environmental heat load entering the baffle aperture and not reflected back will be partly absorbed by the baffle and either radiated into the S/C body (heat load: $Q_{RAD,baffle}$) or conducted via the baffle mounting into the S/C structure (heat load: $Q_{CON,baffle}$)
- The environmental heat load entering the instrument aperture (lenses etc.) either directly or by baffle induced effects will sum up. The sum is described by the parameter load: Q_{INS}.

Within the relevant instrument unit the following parameters apply:

- As said above the heat input entering the unit is described by the parameter Q_{INS}.

- The unit proximity electronics will have the electrical heat dissipation $\mathbf{Q_{ELC}}$
- The total heat derived from the sources above will be partly absorbed by the unit structure and either radiated into the S/C body or conducted via the unit mounting into the S/C structure. These
- heat loads are described by the parameters : $\mathbf{Q_{RAD,Unit}}$ and $\mathbf{Q_{CON,Unit}}$
- The SIMBIO-SYS units require a cold finger and the heat load dumped into the S/C via this interface is described by $\mathbf{Q_{CF}}$.

The heat balance for the baffling subsystem lead to:

$$\mathbf{Q}_{ENV} = \mathbf{Q}_{REF} + \mathbf{Q}_{RAD,baffle} + \mathbf{Q}_{CON,baffle} + \mathbf{Q}_{INS} \tag{96}$$

While the heat balance for the unit optics subsystem lead to:

$$\mathbf{Q}_{INS} + \mathbf{Q}_{ELC} = \mathbf{Q}_{RAD,unit} + \mathbf{Q}_{CON,unit} + \mathbf{Q}_{CF} \tag{97}$$

Defining the sum of all heat loads introduced in the S/C by the baffle is:

$$\mathbf{Q}_{ABS,baffle} = \mathbf{Q}_{RAD,baffle} + \mathbf{Q}_{CON,baffle} \tag{98}$$

saying that the sum of all heat loads introduced in the S/C by the unit is

$$\mathbf{Q}_{ABS,unit} = \mathbf{Q}_{RAD,unit} + \mathbf{Q}_{CON,unit} \tag{99}$$

And then solving to $\mathbf{Q_{INS}}$ it results:

$$\mathbf{Q}_{ENV} - \mathbf{Q}_{REF} + \mathbf{Q}_{ELC} = \mathbf{Q}_{ABS,baffle} + \mathbf{Q}_{ABS,unit} + \mathbf{Q}_{CF} \tag{100}$$

The terms on the left side of equation (100) are defined by the instrument team when designing the payload and are functions of the aperture of the baffle, the baffle performance and the internal electrical power dissipation. The terms on the right side of equation (100) are under responsibility of satellite thermal control system and are limited by the overall system design.

The thermal design of the instrument should aim to reduce the left terms of the equation (100) in order to guarantee that the heat loads introduced by the unit into the S/C will be within the limit established by the spacecraft thermal control system. Hence thermal design of the baffling system is crucial for the thermal performance of the overall instrument. Herein we will focus on thermal analysis of baffles and the reference heat loads are those described by equation (96) .

A widely used discretization **method for modeling thermal systems**, especially in the aerospace thermal engineering community, is the thermal network approach. It is derived from energy balance equations and is equivalent to a particular finite difference discretization of the underlying heat transfer equation. The thermal network is based on having a series of nodes similar to a circuit consisting of thermal resistances, capacitances and heat sources. Here, the currents correspond to heat flow and the nodal potentials to temperatures. In this approach, each node represents a particular isothermal component of the system and provides the basic advantage of fast computation time of complex systems. The network method was introduced in the seminal paper by Oppenheim [17] and details of on the approach, also known as lumped parameters method, can be found in [15], [16], [20].

Radiative heat transfer plays an important role in space applications and consequently suitable software being able to dealing with radiation must be selected. Within the commercially available software dedicated to thermal analysis of space systems, the ESATAN/ESARAD software have been used. This software implements algorithms for the computation of the inter-nodal view factors and radiative exchange factors using the Monte Carlo technique associated with a fast ray-tracing algorithm [21] and algorithms for the solution of nonlinear thermal network for temperature distribution computation [20]. Furthermore an orbit propagator is implemented which allows to calculate solar , albedo and Planetary heat fluxes absorbed by the thermal nodes.

Monte Carlo Ray Tracing (MCRT) is essentially a stochastic method. In principle, this method calculates radiative couplings and heat fluxes by means of a ray-tracing procedure which considers the individual history of the thermal radiation energy packets, from the point of emission to the point of absorption. In reality, these energy packets may follow an infinite number of paths.

Indeed, they can be emitted from any point on every radiative face, in any direction, and may reach and be reflected by any other radiative face in the model. Since it is not possible to follow the path of an infinite number of rays, an estimate of the radiative couplings or heat fluxes can be made by averaging the results obtained from a finite random sample of rays. The individual history of each ray, that is its emission point, emission direction and ray/face interaction, is randomly determined. An introduction to the MCRT method applied to heat transfer analysis can be found in cited references [8], [18], [19] .

For the thermal analysis purposes, in order to focusing on baffle performance, we will make use of a simplified model which allows to perform thermal simulation of baffles comparing different configurations, geometry and thermo-optical properties. The schematics of thermal modeling of the baffling sub-system is graphed in the following Figure 6.2. Geometrically the unit optics will be assumed as a box with a hole corresponding to the optical aperture. A rejection filter will be put at the telescope entrance if the case (HRIC channel). The inner side of the unit optics will be assumed as a blackbody cavity at boundary temperature T_{BO}. This temperature will be established on the basis of preliminary results of thermal models of the unit and sensitivity analysis will be performed within the assumed T_{BO} temperature range. External faces of the optics box will be covered of MLI blanket to insulate the telescope. It has been agreed between the TCS responsible and the instrument team that the unit optics must be thermally insulated to the optical bench, which therefore will not be modeled. The spacecraft thermal environment will be assumed as blackbody cavity at boundary temperature $T_{R,SC}$ defined for hot and cold cases [3], [14] . A baffle bracket for the mountings of the baffle is assumed to be at boundary temperature T_{BB} defined for hot and cold cases [3], [14]; it represents the conductive interface between the baffle and the spacecraft.

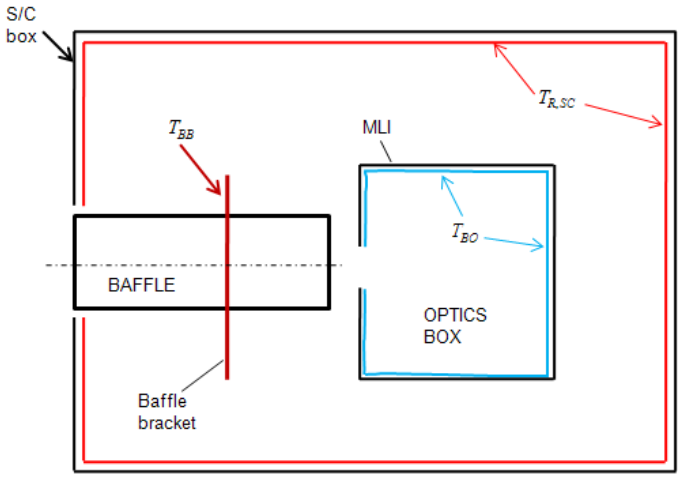

Figure 6.2: baffle thermal model scheme and interfaces

This approach allows to predict the solar, albedo and planetary IR absorbed heat fluxes in orbit around Mercury, to calculate the conductive and radiative heat power exchanged with S/C interfaces and the albedo, solar and IR heat fluxes entering the telescope aperture. Furthermore temperature distribution over the nodes of the baffles can be computed during orbital motion around Mercury.

In the following Table 6.1 are listed the thermal cases analyzed and the interface boundary temperatures values used for the simulations.

	$T_{R,SC}$	T_{BB}	T_{BO}
Perihelion orbit (Hot Case) [°C]	+50	+65	+25
Aphelion orbit (Hot Case) [°C]	+50	+65	+20
Autumn/Spring orbit (Cold case) [°C]	-30	-40	-10

Table 6.1: analysis cases and Boundary temperature

As previously mentioned, the boundary temperature T_{BO} of the inner side of the unit optics will be assumed on the basis of preliminary results of thermal models of the unit [25]. A sensitivity analysis has been performed to evaluate the effect of temperature value T_{BO} on baffle temperature distribution and exchanged heat power with interfaces.
To perform this analysis it has been used the STC and VIHI baffles thermal model and the main results are reported in the following Table 6.2. Comparison has been made between the steady state solution of temperatures and fluxes among the perihelion reference orbit.

Unit black cavity temperature	$T_{BO} = 0°C$	$T_{BO} = 10°C$	$T_{BO} = 20°C$	$T_{BO} = 30°C$	$T_{BO} = 40°C$
Analysis Case	**Perihelion (PH_REF)**	**Perihelion (PH_REF)**	**Perihelion (PH_REF)**	**Perihelion (PH_REF)**	**Perihelion (PH_REF)**
T baffle VIHI(1)	77.10 °C	77.21 °C	77.32 °C	77.56 °C	77.61 °C
QRbc_VIHIB(4)	0.48 W	0.41 W	0.36 W	0.30 W	0.26 W
T baffle STC1(1)	84.68 °C	84.73 °C	84.80 °C	84.86 °C	84.93 °C
QRbc_STCB (5)	0.88	0.75	0.63 W	0.52	0.41
T baffle STC2(1)	85.50 °C	85.56 °C	85.61 °C	85.67 °C	85.74 °C
QLIFbb_tot (2)	12.79 W	12.88 W	12.97 W	13.06 W	13.20 W
QRtoSC_tot (3)	4.85 W	4.93 W	5.00 W	5.08 W	5.15 W

(1) Mean value of baffle's nodes temperature - Steady State solution among orbit (PH_REF)
(2) Conductive heat power to baffle bracket IF – mean value among orbit (PH_REF)
(3) Radiative heat power to S/C radiative environment IF at T = +50°C
(4) Radiative heat power from VIHI baffle to VIHI optics black enclosure
(5) Radiative heat power from STC baffles to STC optics black enclosure

Table 6.2

It could be seen from Table 6.2 that temperature values of baffles and exchanged heat power with interfaces is not greatly affected by differences in the assumed value of temperature T_{BO}. Then it can be deduced that substituting the units optics thermal model with a black cavity at assumed temperature does not greatly affect the results regarding the baffles and therefore the assumption is considered coherent.
This simplification allows to perform detailed thermal analysis and simulations focused on baffling subsystem without implementing the whole unit optics thermal model.

For each SIMBIO-SYS unit thermal mathematical model has been developed and simulations has been performed considering the three most critical orbits identified (see the previous chapter3 of the thesis). These cases corresponds to Perihelion, Aphelion and Spring/Autumn MPO orbits. The orbital parameters used for the simulations are summarized in the following table:

CASE DEFINITION	Perihelion PH_REF	Aphelion AH_REF	Spring/Autumn SP_REF
Apocentre height	1508 km	1508 km	1508 km
Pericentre height	400 km	400 km	400 km
Inclination	90°	90°	90°
Argument of pericentre	0°	0°	0°
Right ascension (Mercury season)	0°	180°	90°
Solar constant	14490 W/m^2	6290 W/m^2	9970 W/m^2

Table 6.3: thermal modeling analysis cases

6.2 HRIC Stavroudis baffle thermal modeling

6.2.1 Description of Stavroudis baffle concept and modeling in ESARAD

Due to its large aperture the HRIC channel will see the largest amount of heat entering the telescope from the environment, then an effective heat rejection must be foreseen for this channel. In an ideal case, a baffle appropriate to severe thermal constraints would reject the un wanted reflection back through the front aperture rather than absorbing it. This capability must be reached by means of a reflective baffle which is nothing but a "non-imaging" optical system characterized by highly specular reflecting surfaces, rather than black diffuse surfaces, and by appropriate geometry [22]. A Stavroudis type baffle has been selected by the SIMBIO-SYS team as a design solution to overcome the heat rejection from severe Mercury environment.

The Stavroudis baffle is a reflective telescope baffling system which consist of an alternated series of ellipsoids (oblate spheroid) and hyperboloids having common foci located at the edge of entrance aperture. This geometry leads to a system that ideally reflects all the stray light entering the aperture as well illustrated by O.N. Stavroudis in [23] . A US patent was awarded on this idea in July 1993 and it is meanwhile expired [24].

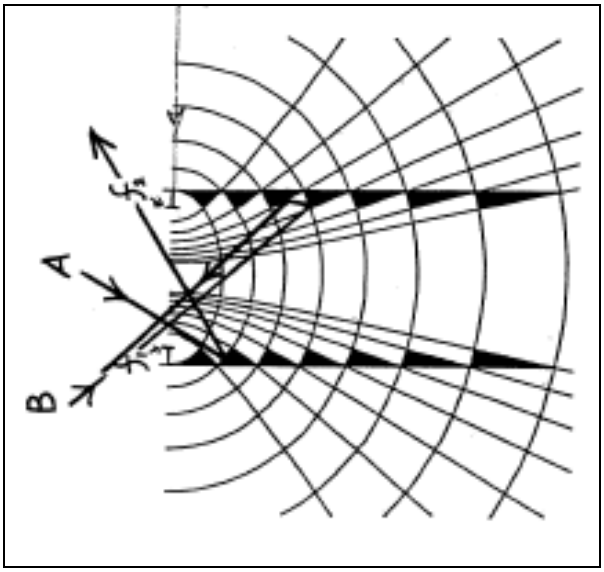

*Figure 6.3: Stavroudis baffle concept. The points **f1** and **f2** are the common foci*
***A** : a ray falling onto ellipse is rejected after 1 reflection*
***B**: a ray falling onto hyperbola is rejected after 2 reflection*
(see ref. [23] .)

The thermal modeling of Stavroudis baffle must be made using appropriate geometrical representation due to the optical properties depending on the particular geometry of the baffle.

ESARAD software is not able to model neither ellipsoids nor hyperboloids surfaces, so the Monte Carlo ray-tracing must be performed using an approximating geometry. Preliminary study has been conducted to find a suitable approximation of baffle geometry to be used in thermal modeling software. It was found out that an appropriate model should minimize the adsorbed flux on the internal part of the Stavroudis frontal ring. This rule stems directly from the Stavroudis geometry and from the ellipses and hyperbola geometrical properties. Ideally, if ellipses and hyperbola had a specular reflective coefficient equal to one, the flux adsorbed by the inner side of the Stavroudis frontal ring would be zero. Moreover, in a baffle of sufficient length, an appropriate model should minimize the direct solar adsorbed fluxes by a surface at the rear side of the baffle. Ideally, if ellipses and hyperbola had a specular reflective coefficient equal to one, the flux adsorbed by this surface would be zero and all the incident solar rays would be rejected out of the entrance aperture (see Figure 6.4).

Then an appropriate model should minimize the flux absorbed by the internal part of the Stavroudis frontal ring and by the rear side of baffle. This will be chosen as figure of merit for the thermal model of the Stavroudis.

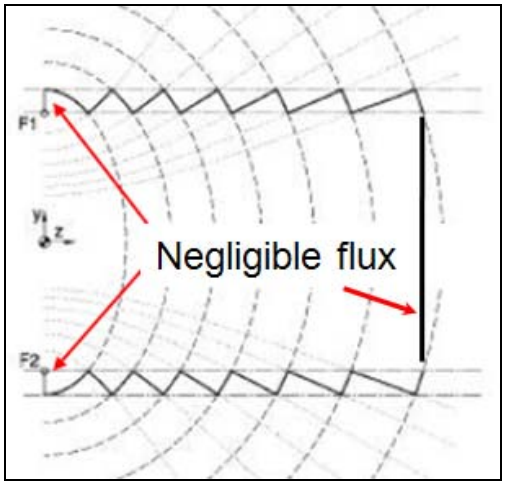

Figure 6.4: Stavroudis baffle figure of merit

To implement the baffle in ESARAD software, every conic profile have been modeled with a series of primary geometrical shells in order to improve the results of Monte Carlo ray tracing. Some simulations have been performed to find an appropriate geometrical representation of Stavroudis . The following discretization (Table 6.4, Table 6.5) have been analyzed and compared:

		ESARAD SHELL TYPE USED	DISCRETIZATION
CASE 1	ELLIPSES	CONE	DETAILED
	HYPERBOLAS	CONE	
CASE 2	ELLIPSE	CONE	COARSE
	HYPERBOLA	CONE	
CASE 3	ELLIPSE	SPHERICAL SEGMENT	COARSE
	HYPERBOLA	CONE	

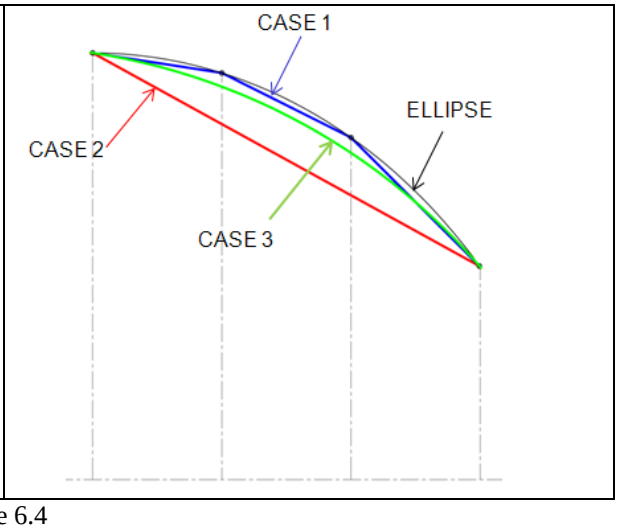

Table 6.4

In order to make easier the modeling process, some Matlab routines has been implemented to automatically calculate the Stavroudis geometry given the aperture diameter, the external diameter and the number of ellipsoids and hyperboloids constituting the baffle. The significant points of the approximating geometrical shell will be calculated and a ESARAD command file is automatically generated. This file can therefore be directly imported in ESARAD. Furthermore, given the fact that ESARAD software does not calculate conductive interfaces with circular edge between two geometric shells, some algorithms have been implemented that calculate the conductive links between contiguous cone shells. The conductive link analytical formulae for a conical shell has been calculated. With regards to conductive links, the conduction formulae for conic shell has been assumed to be a good approximation also for spherical shells. The numerical results presented hereafter refer to a previous configuration of a conical Stavroudis baffle, even if the method has been tested and successfully applied also to present configuration of cylindrical Stavroudis baffle.

	SHELL TYPE USED	ELL1	HYP1	ELL2	HYP2	ELL3	HYP3	ELL4	HYP4	ELL5	HYP5	ELL6	NUMBER OF AXIAL SEGMENTS	TOTAL
CASE 1	CONE	39		9		9		9		9		9	79	
	CONE		9		9		9		10		11		48	127
CASE 2	CONE	10		3		1		1		1		1	17	
	CONE		2		1		1		1		1		6	23
CASE 3	SPHERICAL SEGMENT	10		3		1		1		1		1	17	
	CONE		2		1		1		1		1		6	23

Table 6.5

The thermo-optical properties reported in Table 6.6 has been used for this analysis , following the model scheme of Figure 6.2.

nodes	ε	ρ_{IR}^{d}	τ_{IR}	α	ρ_{S}^{d}	τ_{S}	ρ_{IR}^{s}	ρ_{S}^{s}
Baffle Stavroudis	0.03	0.00	0.00	0.12	0.00	0.00	0.97	0.88
Filter (outward)	0.25	0.75	0.00	0.20	0.00	0.80	0.00	0.00
Filter (inward)	0.96	0.04	0.0	0.0	0.0	1.0	0.0	0.0
MLI (kvda)	0.05	0.95	0.00	0.15	0.85	0.00	0.00	0.00
Black surf.	1.0	0.0	0.0	1.0	0.0	0.0	0.0	0.0

Table 6.6: thermo-optical properties

Simulations of the three different representation of baffle (Table 6.4, Table 6.5) has been performed and results of the analysis will be presented in the following plots. Radiative case orbit is Perihelion orbit.

In order to figuring out what should be the best representation of a Stavroudis baffle in ESARAD, the results have been analyzed by comparison of:

- Heat power absorbed by the inward side of the frontal ring of the baffle
- Solar power absorbed by a black surface behind the filter

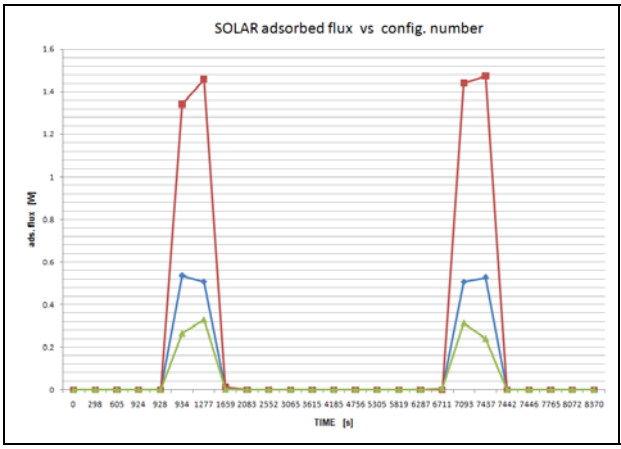

Figure 6.5: *Inward side of frontal ring: absorbed solar heat comparison.*
case 1 (blue), case2 (red), case3 (green)

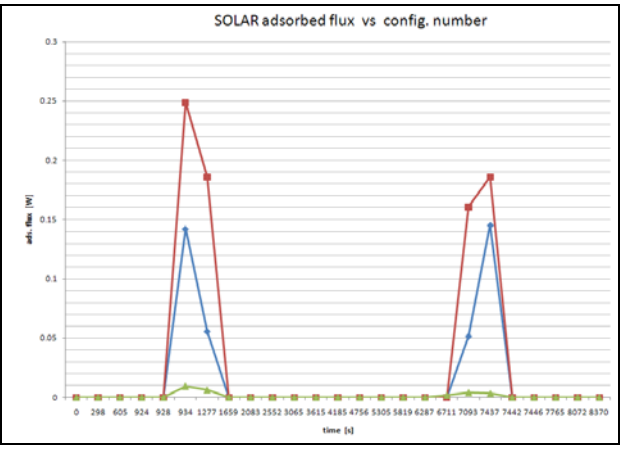

Figure 6.6 *: Black surface behind the filter: absorbed solar heat comparison*
case 1 (blue), case2 (red), case3 (green)

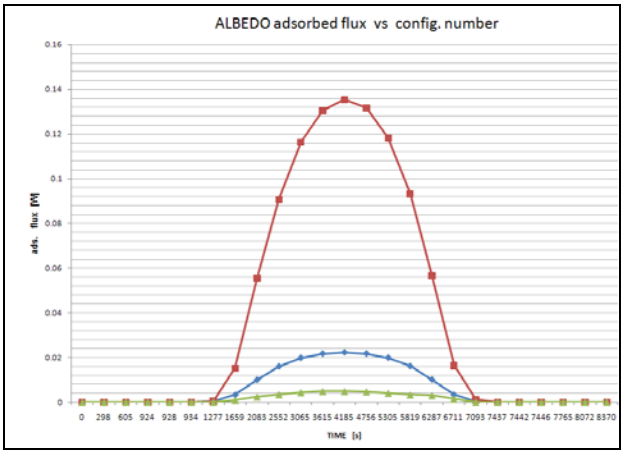

Figure 6.7*: Inward side of frontal ring: absorbed albedo heat comparison.*
case 1 (blue), case2 (red), case3 (green)

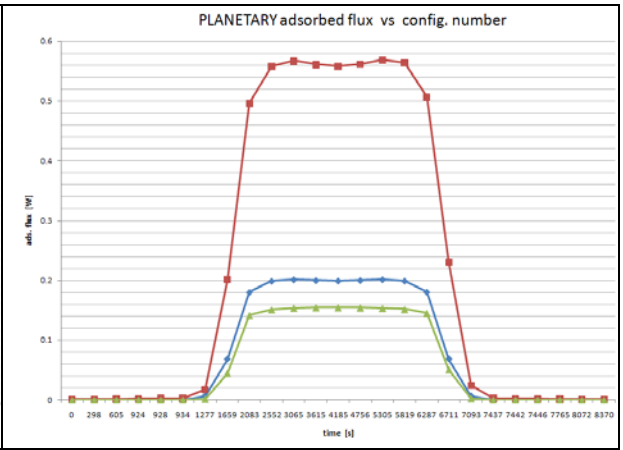

Figure 6.8: *Inward side of frontal ring: absorbed planetary heat comparison*
case 1 (blue), case2 (red), case3 (green)

Inward side of frontal ring						
AVERAGE VALUES [W]	**SOLAR**		**ALBEDO**		**PLANETARY**	
CASE1 : 127 segments / CONES	0.083	79.6%	0.007	340.4%	0.077	30.9%
CASE 2 : 23 segments / CONES	0.229	394.1%	0.038	2466.6%	0.218	271.7%
CASE 3 : 23 segments / SPHERICAL + CONES	0.046	REF	0.001	REF	0.059	REF

Table 6.7: average values of heat fluxes power absorbed by the inward side of frontal ring

Inward side of frontal ring						
PEAK VALUES [W]	**SOLAR**		**ALBEDO**		**PLANETARY**	
CASE1 : 127 segments / CONES	0.536	62.1%	0.022	353.6%	0.201	30.3%
CASE 2 : 23 segments / CONES	1.474	346.0%	0.135	2659.1%	0.569	268.0%
CASE 3 : 23 segments / SPHERICAL + CONES	0.331	REF	0.005	REF	0.155	REF

Table 6.8: peak values of heat power absorbed by the inward side of frontal ring

Referring to results reported in the above Figure 6.5, Figure 6.7, Figure 6.8 and in Table 6.7 and Table 6.8 , if we consider the *heat adsorbed* by the *inward side of frontal ring* as the parameter to evaluate how appropriate the model is, it is shown that the use of **spherical segment** is more effective than using series of conical segments, even with a large number of segments.

Black surface behind the filter						
AVERAGE VALUES [W]	SOLAR		ALBEDO		PLANETARY	
CASE1 : 127 segments / CONES	0.016	1506.8%	0.232	29.0%	0.000	-
CASE 2 : 23 segments / CONES	0.031	3079.0%	0.200	11.1%	0.000	-
CASE 3 : 23 segments / SPHERICAL + CONES	0.001	REF	0.180	REF	0.000	REF

Table 6.9: average values of heat power absorbed by a black surface behind the filter

Black surface behind the filter						
PEAK VALUES [W]	SOLAR		ALBEDO		PLANETARY	
CASE1 : 127 segments / CONES	0.145	1459.0%	0.909	28.8%	0.000	-
CASE 2 : 23 segments / CONES	0.248	2566.6%	0.777	10.2%	0.000	-
CASE 3 : 23 segments / SPHERICAL + CONES	0.009	REF	0.706	REF	0.000	REF

Table 6.10: peak values of heat power absorbed by a black surface behind the filter

Referring to results reported in the above Figure 6.6 and Table 6.9 and Table 6.10, if we consider the *solar power absorbed* by a *black surface behind the filter* as the parameter to evaluate how appropriate the model is, it is shown that the use of spherical segment is much more effective than using series of conical segments, even using a large number of segments.

CONFIGURATION	COMPUTATIONAL TIME (1 orbit ESARAD run)	MODELING EFFECTIVENESS RANKING
CASE1 : 127 segments / CONES	15 ~ 24 h	2nd
CASE 2 : 23 segments / CONES	20 ~ 40 min	3rd- worst
CASE 3 : 23 segments / SPHERICAL + CONES	20 ~ 40 min	1st - Best

Table 6.11: Stavroudis modeling outlooks and conclusions

From the results of simulation presented above we can infer that the use of spherical segments in ellipses modeling allows to :

- significantly reduce the computational time
- significantly increase the modeling effectiveness, reducing the overestimation of absorbed heat fluxes
- effectively model the baffle even with constraints on the number of nodes (e.g. in ITMM)
- perform reliable trade-off analysis of the baffle (quite impossible with frustum of cones modelisation)

Concluding, as ESARAD does not allow to model ellipsoids and hyperboloids, spherical segments should be used to implement in ESARAD the ellipsoids of HRIC Stavroudis baffle

Furthermore this study lead to the definition of a **criterion** to evaluate the **performance** of a Stavroudis baffle whose figure of merit is to minimize the values of absorbed fluxes by the internal part of the Stavroudis frontal ring and by the rear side of baffle. Furthermore this criterion will guide the design of the most appropriate test-bed to be used to evaluate the performance of a Stavroudis baffle.

6.3 Stavroudis baffle thermal analysis and results

6.3.1 Nodal breakdown and thermo-optical properties

A thermal mathematical model of HRIC Stavroudis baffle has been implemented in ESARAD/ESATAN software in order to estimate the temperature distribution and heat transfer main paths.

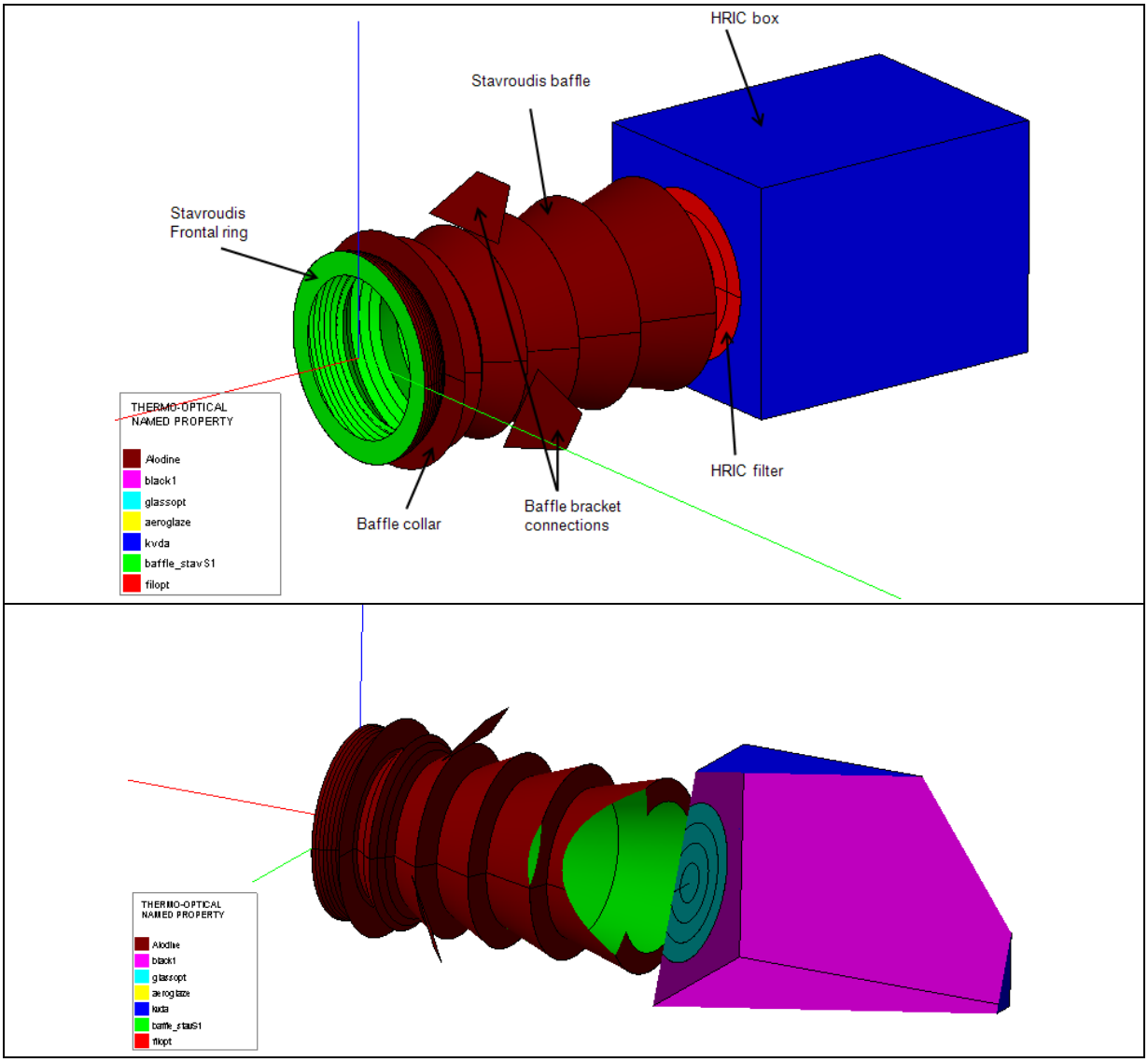

Figure 6.9: HRIC Stavroudis baffle thermal model

At present the Stavroudis baffle is foreseen to be made of sintered aluminum alloy RSA6061, with properties indicated in Table 6.13 . This allow to perform manufacturing processes that allow to have excellent surface roughness (RMS < 2nm) and shape stability to reproduce the particular ellipsoids/hyperboloids geometry of the baffle. This lead to have the highly reflective thermo-optical properties indicated in the following Table 6.12. This properties apply to the frontal ring and to the internal surfaces of the baffle. Externally the baffle will be alodined. The HRIC filter will be externally coated of Al-doped ZnO (ZAO) which has comparable electrical, optical and infrared (IR)

properties to ITO, is cost-effective and is easy to fabricate. It will cut the infrared radiation coming from the outer space as indicated in Table 6.12.
The geometry of the baffle will be modeled following the methods indicated in previous chapter 6.2.1 and due conductive links between nodes will be calculated with ad-hoc implemented Matlab routines using conduction calculation formulae of frustum of cones. In the following tables the thermo-optical properties and bulk material properties used in the model are reported.

Node #	Name	Thermo-optical	ε	ρ_{IR}^{d}	τ_{IR}	α	ρ_{S}^{d}	τ_{S}	ρ_{IR}^{s}	ρ_{S}^{s}
682000-682022	Stavroudis (int.)	Polished	0.05	0.05	0.00	0.12	0.03	0.00	0.90	0.85
682000-682022	Stavroudis (ext.)	Alodine	0.15	0.425	0.00	0.35	0.325	0.00	0.425	0.325
689600	Baffle collar	Alodine	0.15	0.425	0.00	0.35	0.325	0.00	0.425	0.325
682023	Baffle frontal ring (int.)	Aeroglaze	0.85	0.075	0.00	0.96	0.02	0.00	0.075	0.02
682023	Baffle frontal ring (ext.)	Polished	0.05	0.05	0.00	0.12	0.03	0.00	0.90	0.85
689000-689400	Baffle bracket interface	Alodine	0.15	0.425	0.00	0.35	0.325	0.00	0.425	0.325
672000-672003	Filter (inward)	glass	0.96	0.04	0.00	0.00	0.00	1.00	0.00	0.00
671000-671003	Filter (outward)	ZAO	0.25	0.75	0.00	0.20	0.00	0.80	0.00	0.00
674000-674005	HRIC box (ext.)	MLI (kvda)	0.05	0.95	0.00	0.15	0.85	0.00	0.00	0.00
10000 - 10005	HRIC box (int.)	Black1	1.0	0.0	0.0	1.0	0.0	0.0	0.0	0.0
5000	S/C int. environment	Black1	1.0	0.0	0.0	1.0	0.0	0.0	0.0	0.0

Table 6.12: Nodes and thermo-optical properties

Name	Material	Heat capacity c_p [J/(kg K)]	Density ρ [kg/m^3]	Thermal conductivity k [W/(m K)]
Stavroudis baffle	RSA6061 (sintered)	2800	850	130
Filter	Zerodur glass	2530	800	1.46
HRIC box MLI cover	MLI foil	0.0	0.0	0.7

Table 6.13: Nodes and bulk material properties

6.3.2 Analysis cases and results of thermal simulations

In the following paragraph are reported the results of thermal simulations performed. It will be presented mean and peak temperature distribution obtained for critical radiative cases and afterwards graphs of temperatures of HRIC Stavroudis baffle nodes and filter nodes during two subsequent orbits. Since the algorithm implemented in ESATAN integrates the system of nonlinear differential equations taking as initial condition the steady state solution of the thermal network, two subsequent orbits are taken to allow the solution to replicate temperature distribution at the beginning and at the end of the orbit.

The heat balance loads for the baffling subsystem, with reference to equation (96) , will be reported in tables. The balance refers to steady state solution (average among the orbit), with quantity defined in [3] (see paragraph 6.1). The average heat power at interfaces and the heat load entering the instrument will be reported. These quantities are: the total conductive heat power from baffle nodes to S/C bracket ($Q_{CON,baffle}$), the total radiative heat power from baffle's nodes to S/C radiative environment ($Q_{RAD,baffle}$) and the average heat load entering the unit Q_{INS} which is the sum of heat loads entering the instrument aperture either directly ($Q_{INS,ENV}$) or by filter /baffle induced effects ($Q_{INS,IND}$). The average environmental thermal inputs Q_{ENV} have been also computed in order to evaluate the rejection capability of the baffling system.

6.3.2.1 APHELION reference orbit

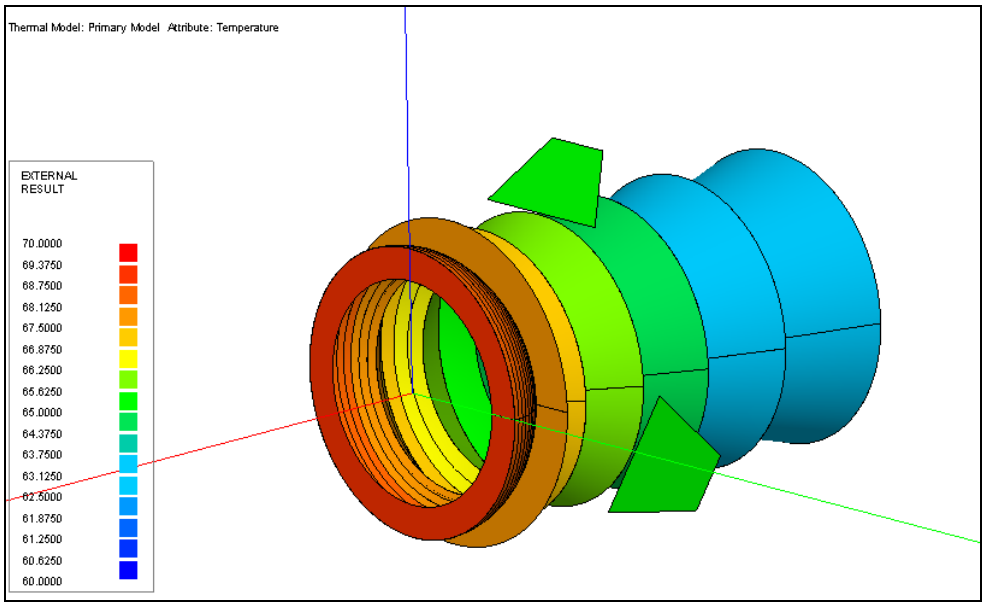

Figure 6.10: HRIC baffle Steady state temperature (Aphelion)

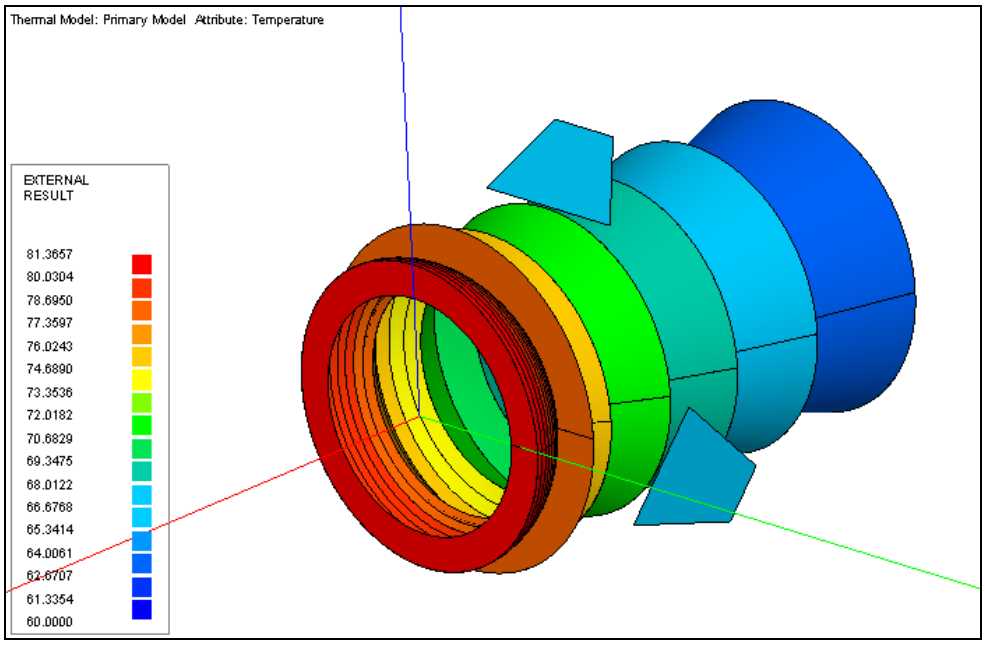

Figure 6.11: HRIC baffle . Peak temperature during aphelion orbit (at t = 11310 s)

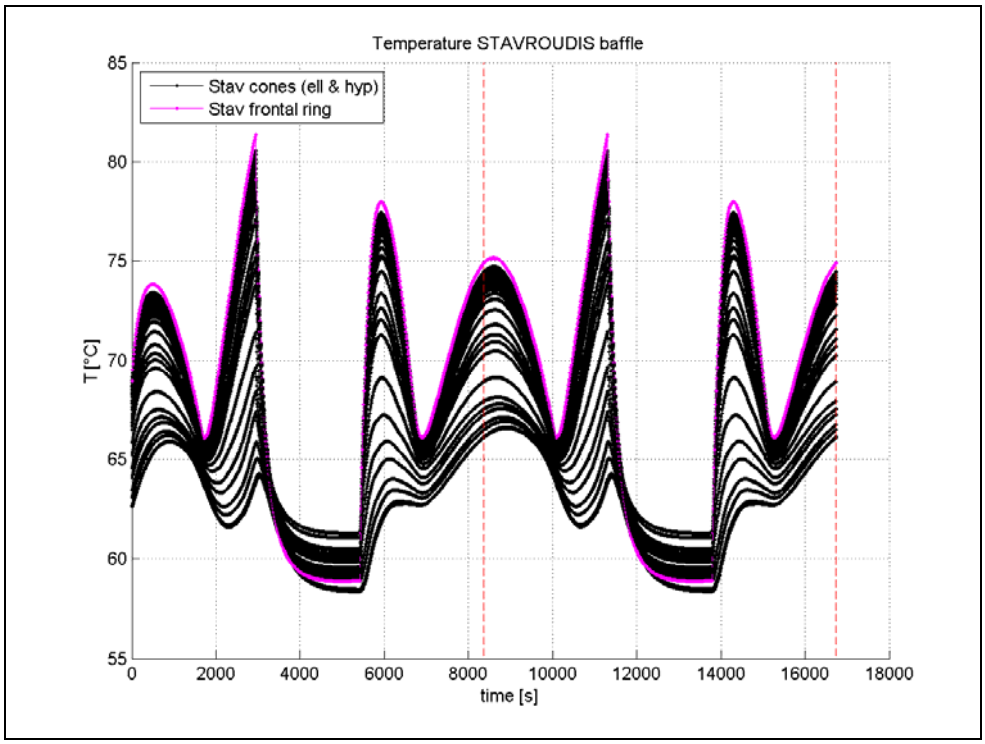

Figure 6.12: Temperature of HRIC Stavroudis baffle nodes (Aphelion)

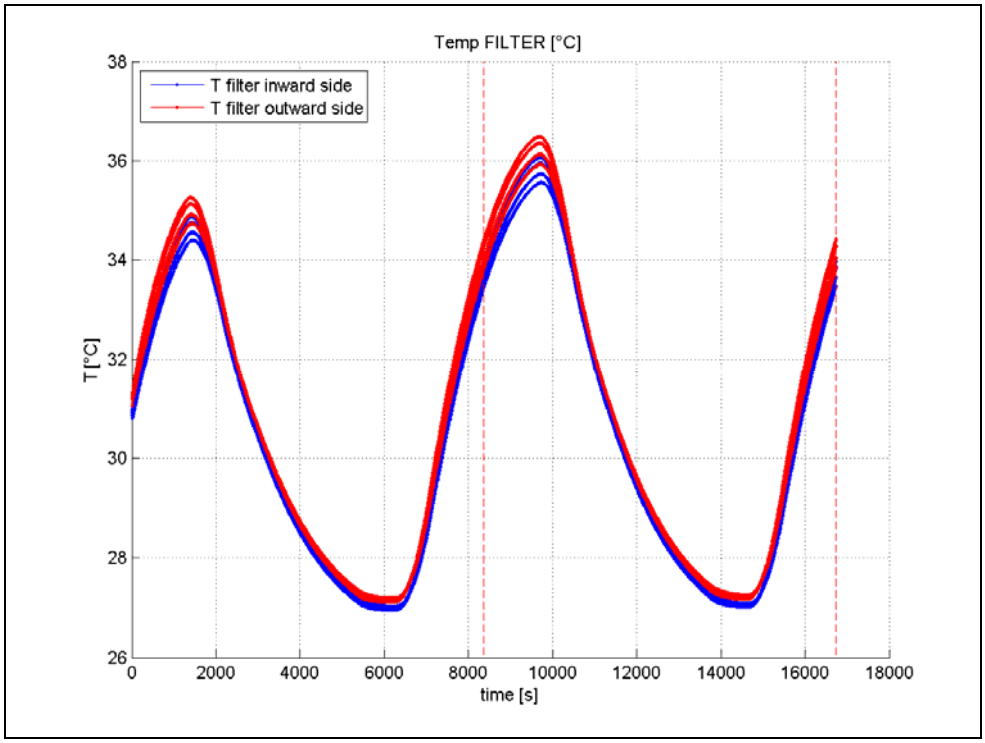

Figure 6.13: Temperature of HRIC filter (Aphelion)

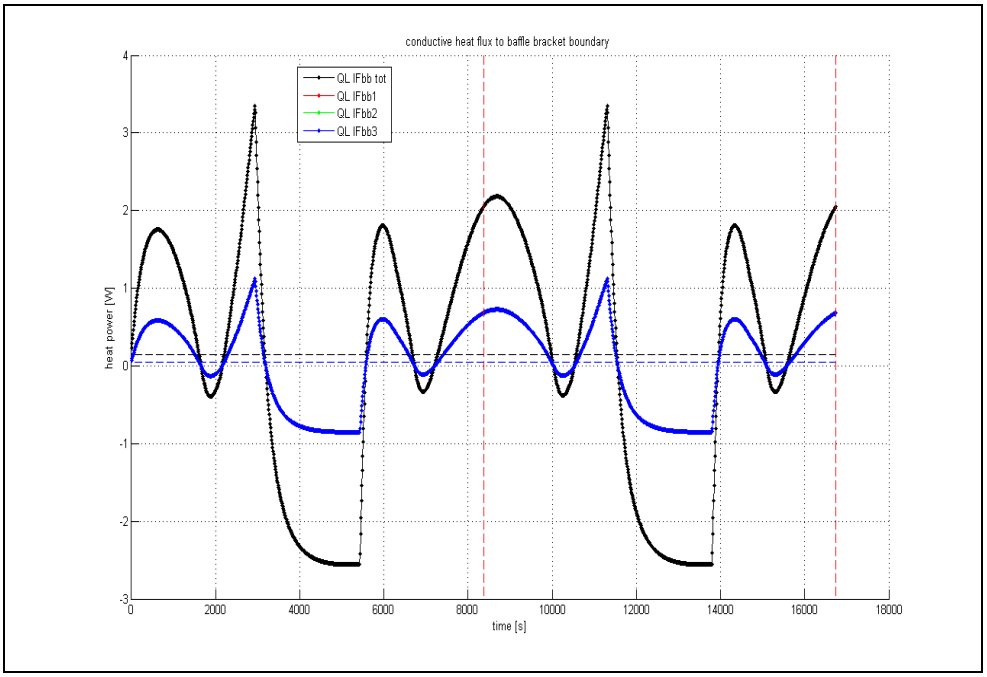

Figure 6.14: Conductive heat power from HRIC baffle to S/C bracket (Aphelion)

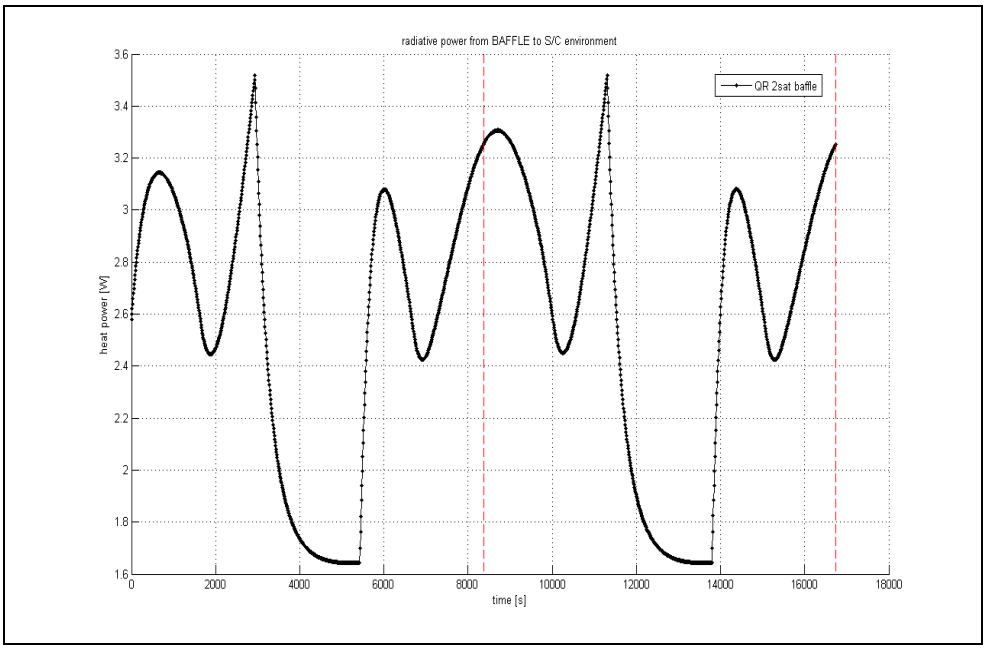

Figure 6.15: Radiative heat power from baffle to S/C radiative environment (Aphelion)

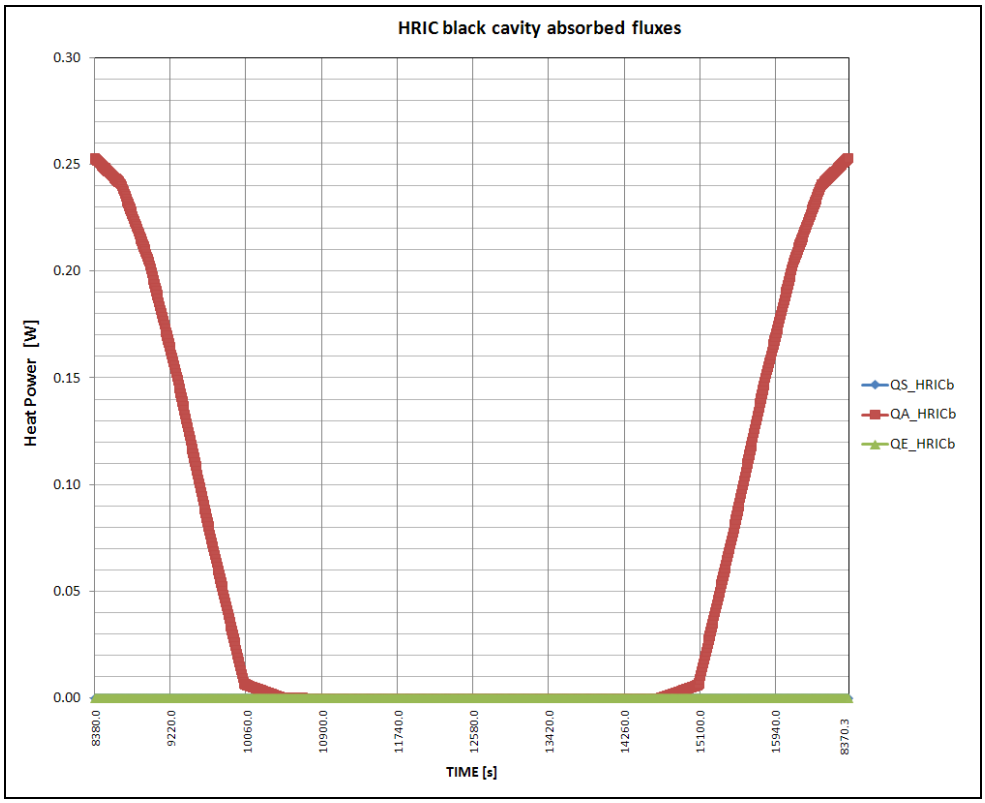

Figure 6.16: HRIC black enclosure absorbed fluxes (Aphelion)

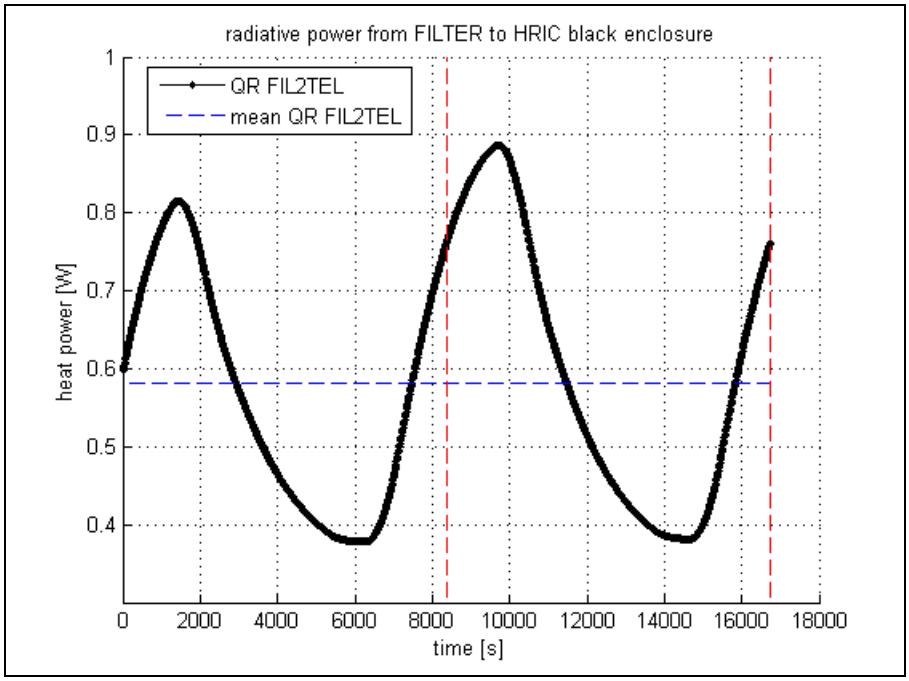

Figure 6.17: radiative power from filter to HRIC black enclosure (Aphelion)

In the following tables are reported the average orbital heat loads among the orbit and the mean values of temperature at nodes (steady state solution). Quantities are those defined in [3] (see paragraph 6.1).

HRIC steady state Heat Loads [W] (Aphelion)						
Qenv	**Qref**	**Qrad,baffle**	**Qcon,baffle**	**Qins**	**Qins, ind**	**Qins, env**
35.1	31.7	2.6	0.2	0.7	0.6	0.1

Table 6.14

HRIC steady state temperatures [°C] (Aphelion)				
$T_{R,SC}$ Boundary node	T_{BB} Boundary node	T_{BO} Boundary node	**Tbaffle (mean)**	**Tfilter (mean)**
+50	+65	+20	67.7	31.0

Table 6.15

It can be seen that the baffling system will reject around the 90% of the heat coming from the environment.

6.3.2.2 PERIHELION reference orbit

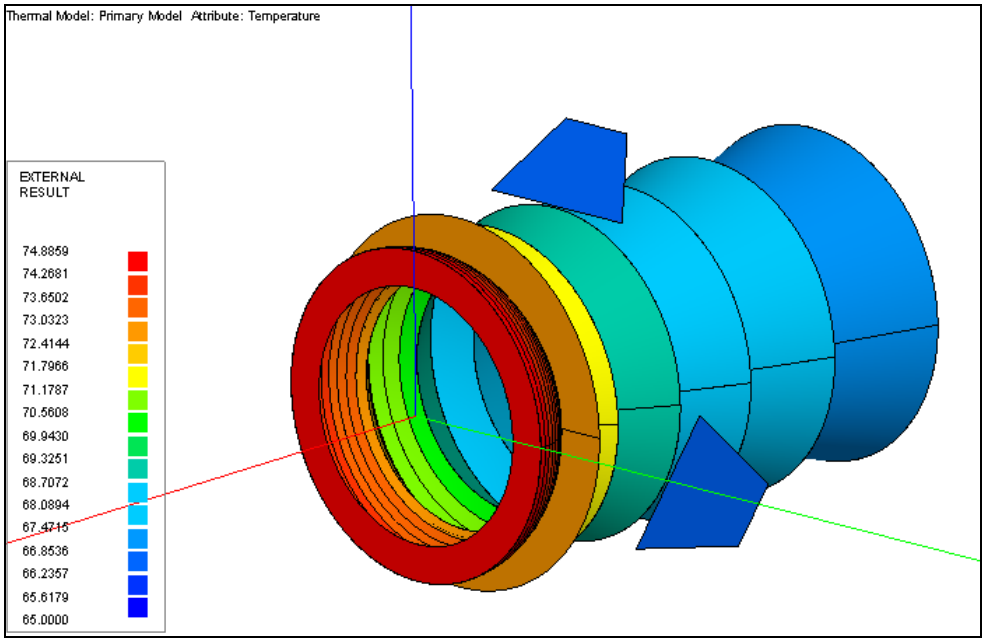

Figure 6.18: HRIC baffle Steady state temperature (Perihelion)

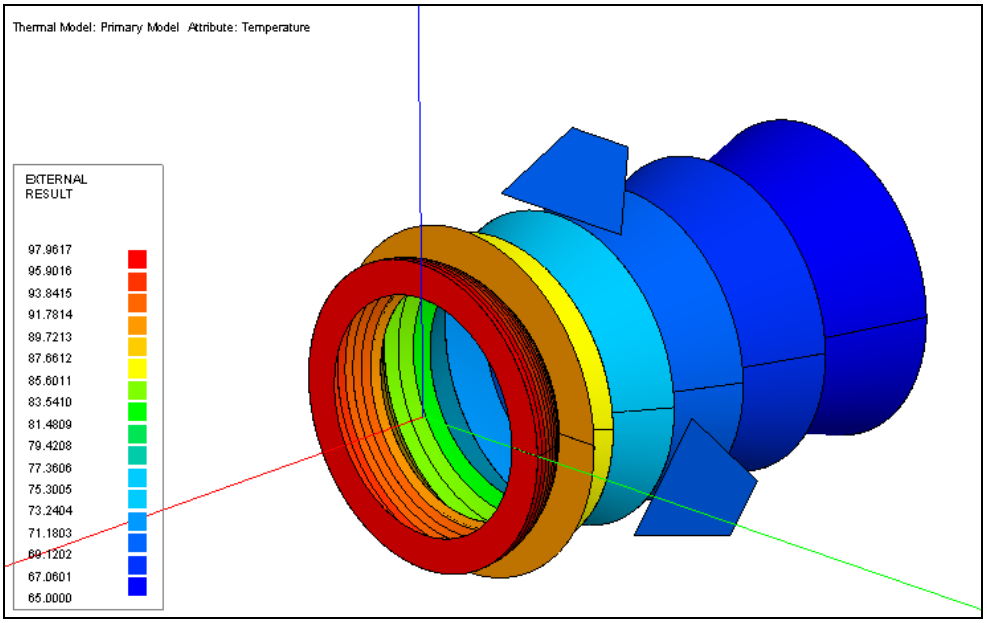

Figure 6.19: HRIC baffle peak temperature during perihelion orbit (at t = 15810 s)

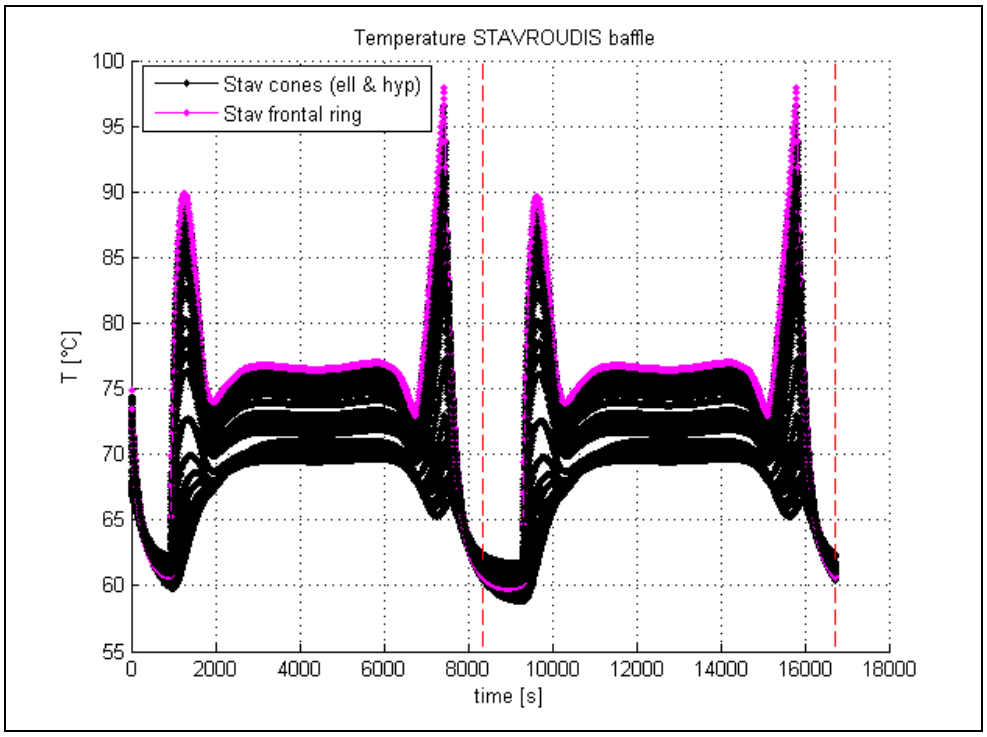

Figure 6.20: Temperature of HRIC Stavroudis baffle nodes (Perihelion)

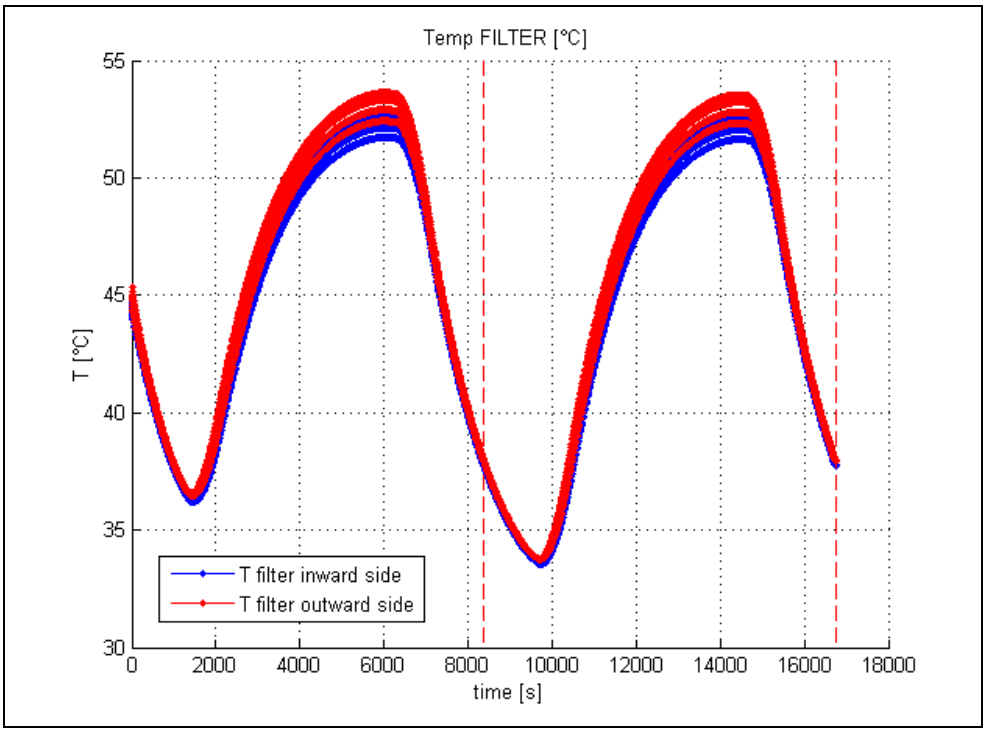

Figure 6.21: Temperature of HRIC filter (Perihelion)

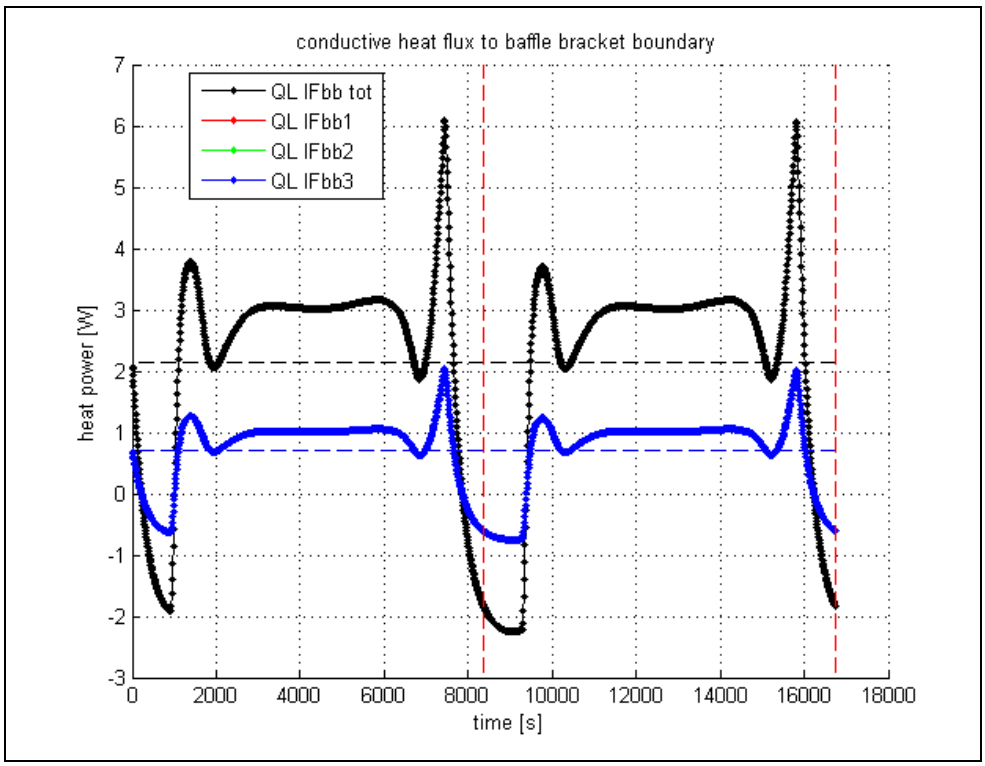

Figure 6.22: Conductive heat power from HRIC baffle to S/C bracket (Perielion)

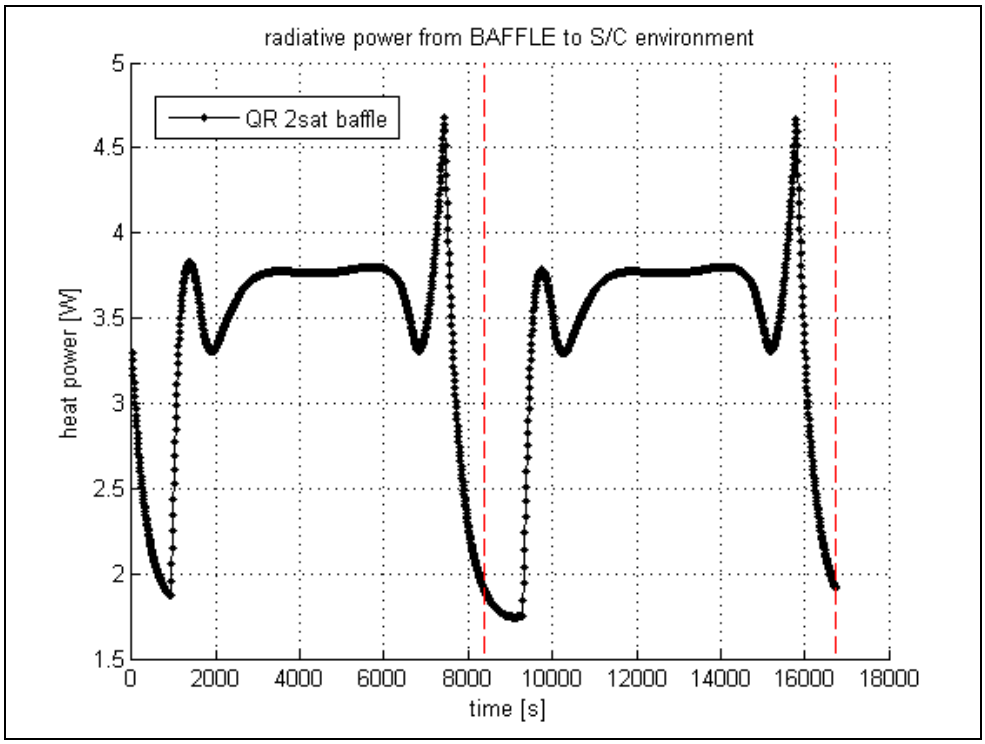

Figure 6.23: Radiative heat power from baffle to S/C radiative environment (Perihelion)

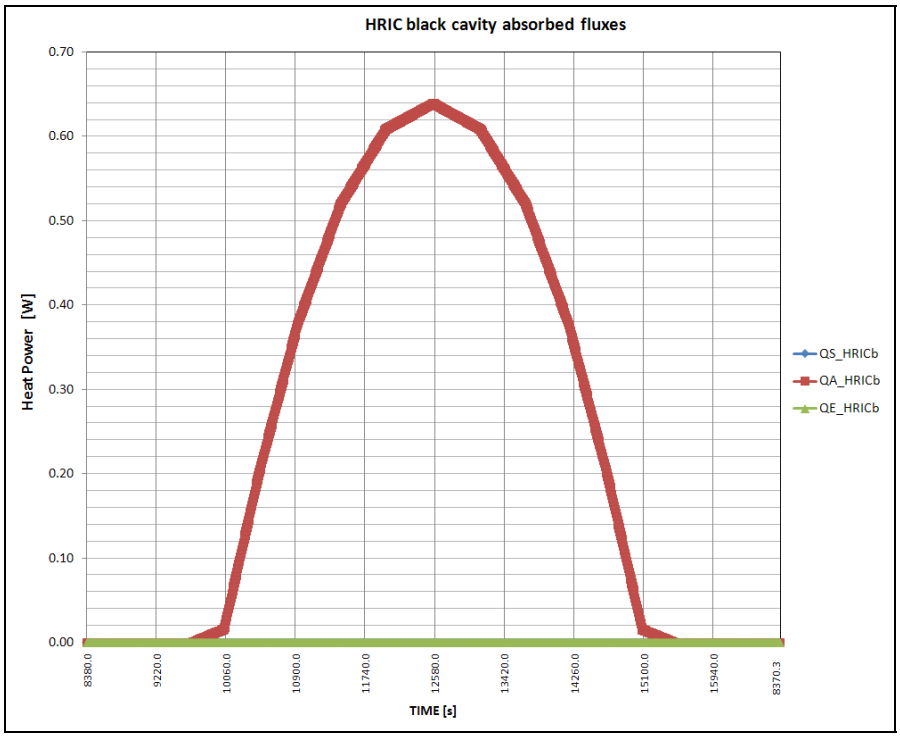

Figure 6.24: HRIC black enclosure absorbed fluxes (Perihelion)

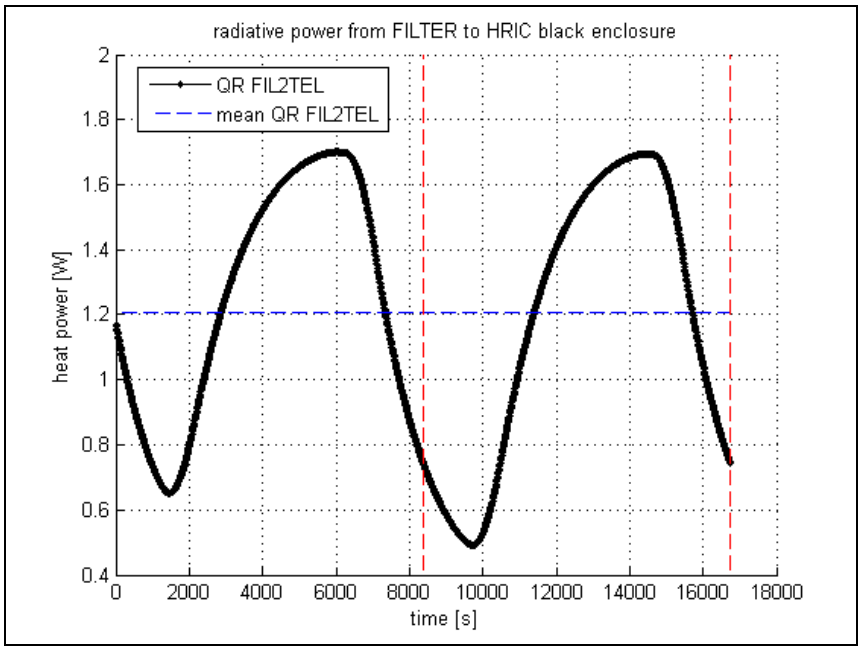

Figure 6.25: radiative power from filter to HRIC black enclosure (Perihelion)

In the following tables are reported the average orbital heat loads among the orbit and the mean values of temperature at nodes (steady state solution). Quantities are those defined in [3] (see paragraph 6.1).

HRIC steady state Heat Loads [W] (Perihelion)						
Qenv	**Qref**	**Qrad,baffle**	**Qcon,baffle**	**Qins**	**Qins, ind**	**Qins, env**
60.5	53.6	3.3	2.1	1.5	1.2	0.3

Table 6.16

HRIC steady state temperatures [°C] (Perihelion)				
$T_{R,SC}$	T_{BB}	T_{BO}	Tbaffle (mean)	Tfilter (mean)
+50	+65	+25	73.0	44.7

Table 6.17

It can be seen that the baffling system will reject around the 90% of the heat coming from the environment.

6.3.2.3 SPRING / AUTUMN reference orbit

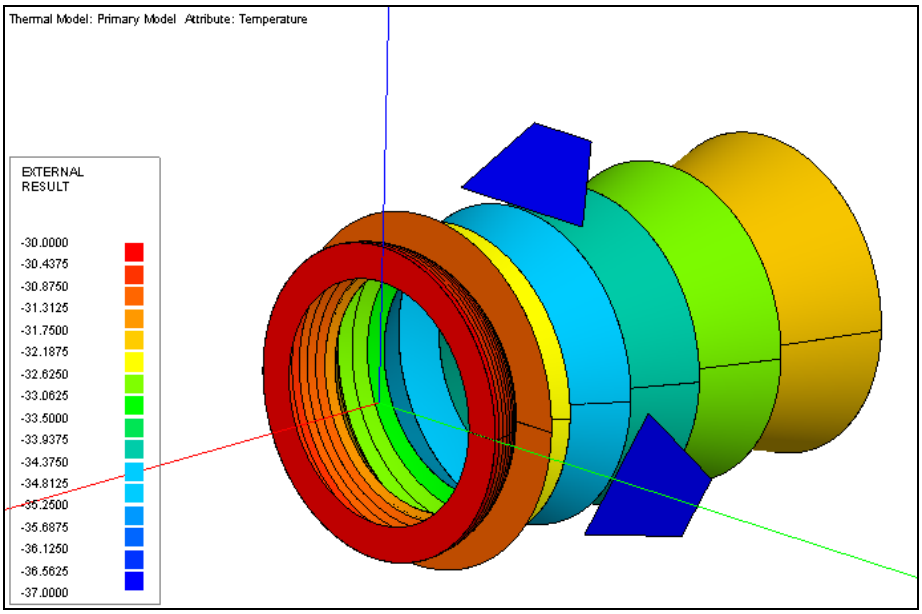

Figure 6.26: HRIC baffle steady state temperature (Spring/Autumn)

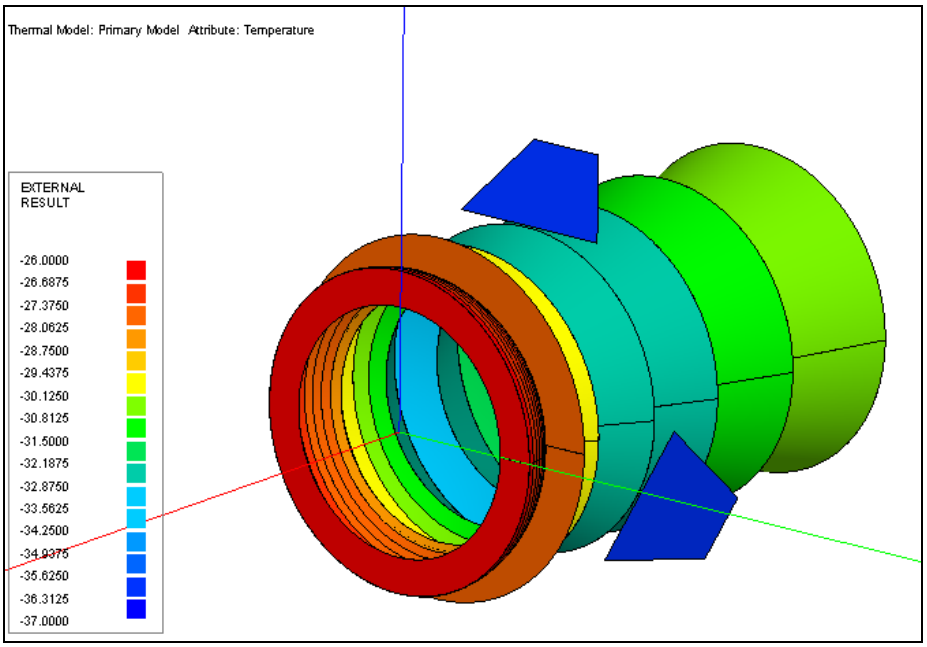

Figure 6.27: HRIC baffle peak temperature during spring/Autumn orbit (at t = 8630s)

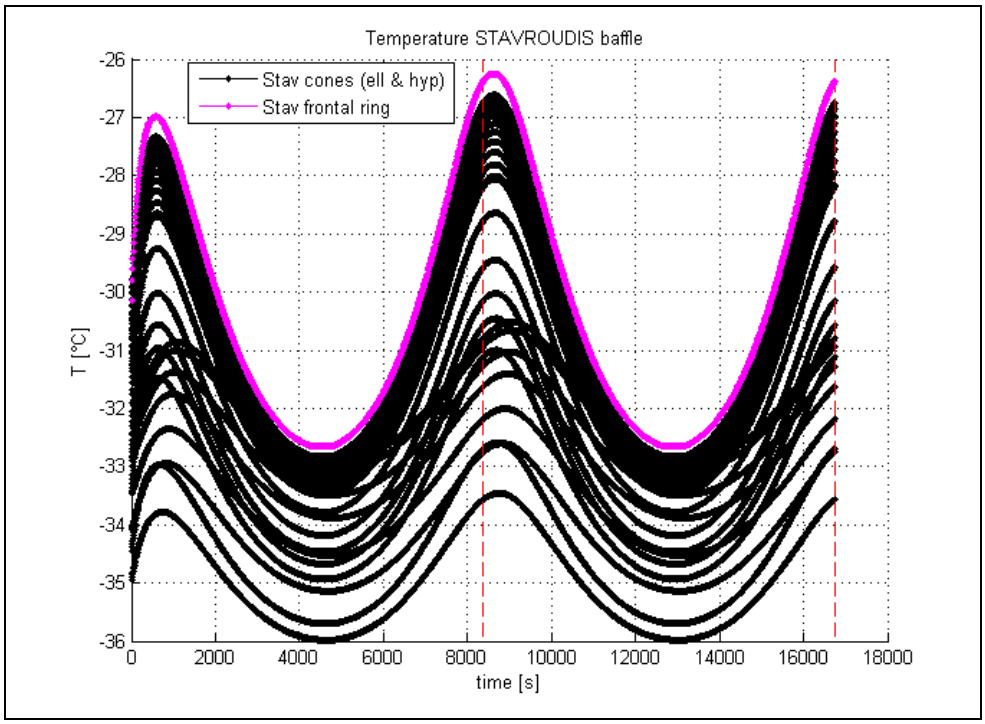

Figure 6.28: Temperature of HRIC Stavroudis baffle nodes (Spring/Autumn)

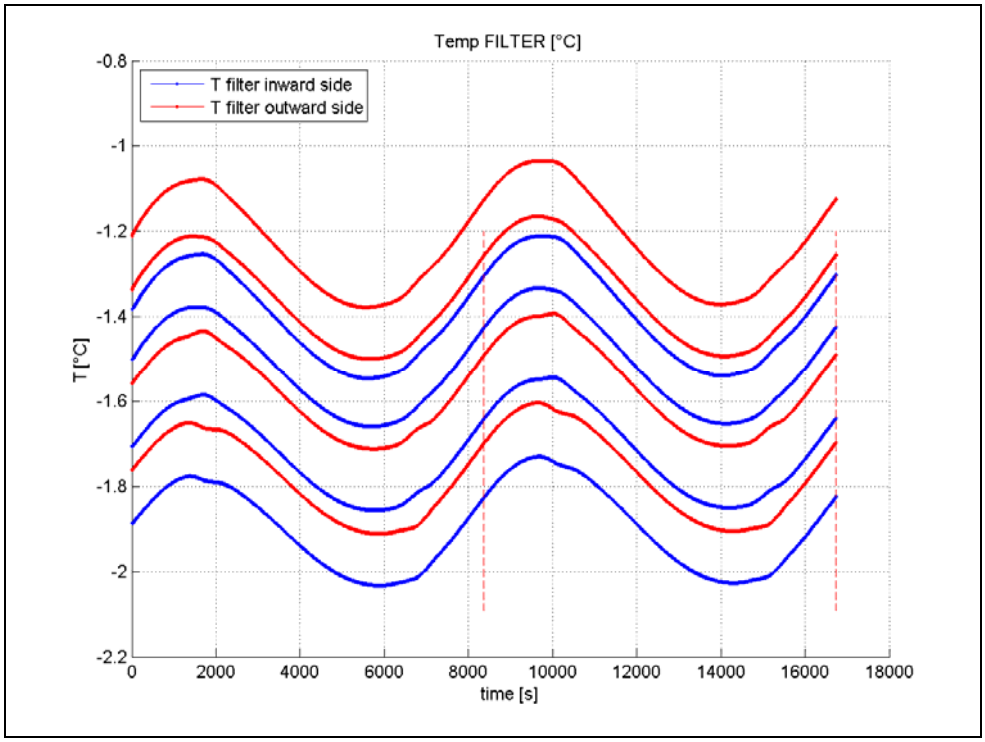

Figure 6.29: Temperature of HRIC filter (Spring/Autumn)

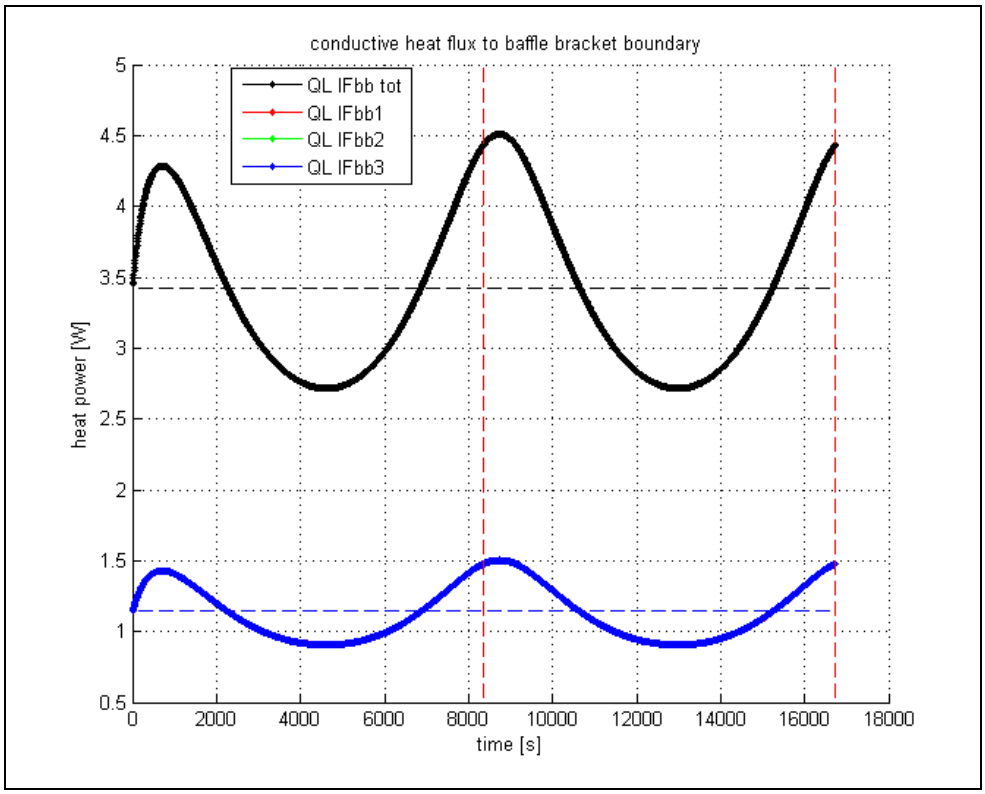

Figure 6.30: Conductive heat power from HRIC baffle to S/C bracket (Spring/Autumn)

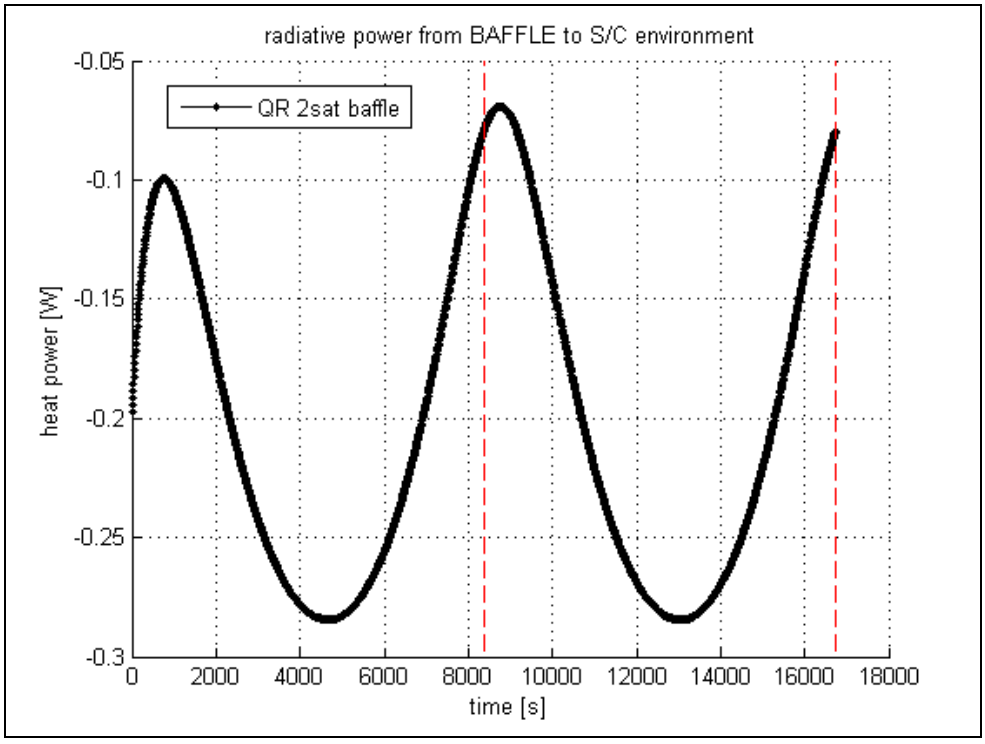

Figure 6.31: Radiative heat power from baffle to S/C radiative environment (Spring/Autumn)

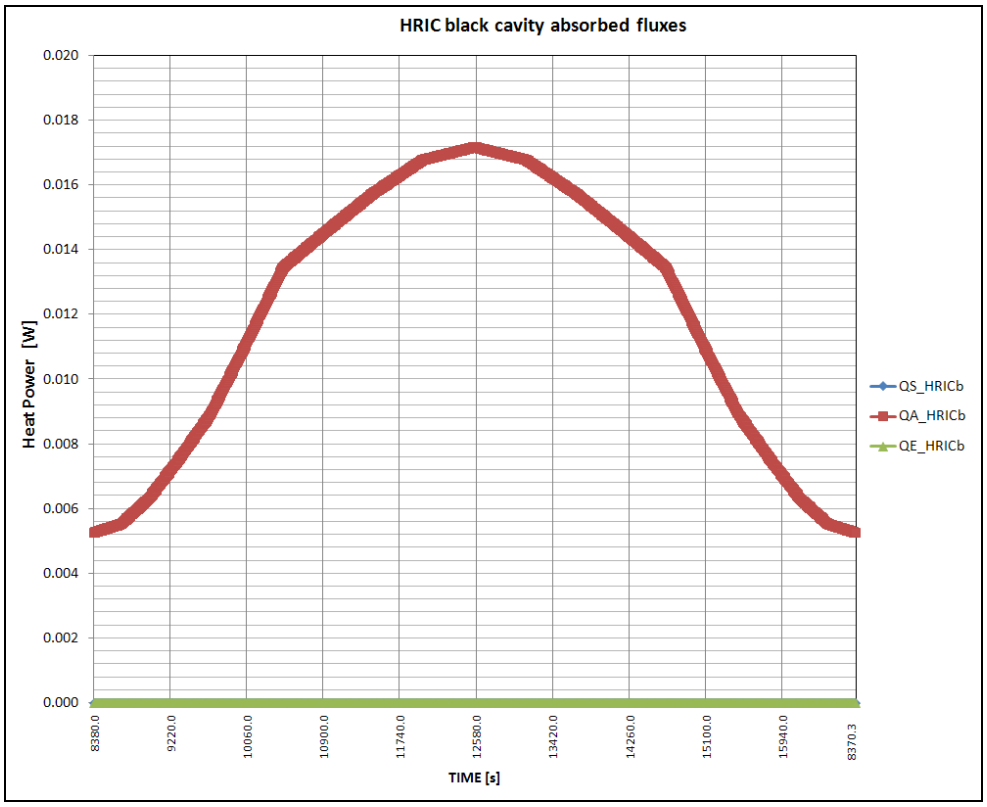

Figure 6.32: HRIC black enclosure absorbed fluxes (Spring/Autumn)

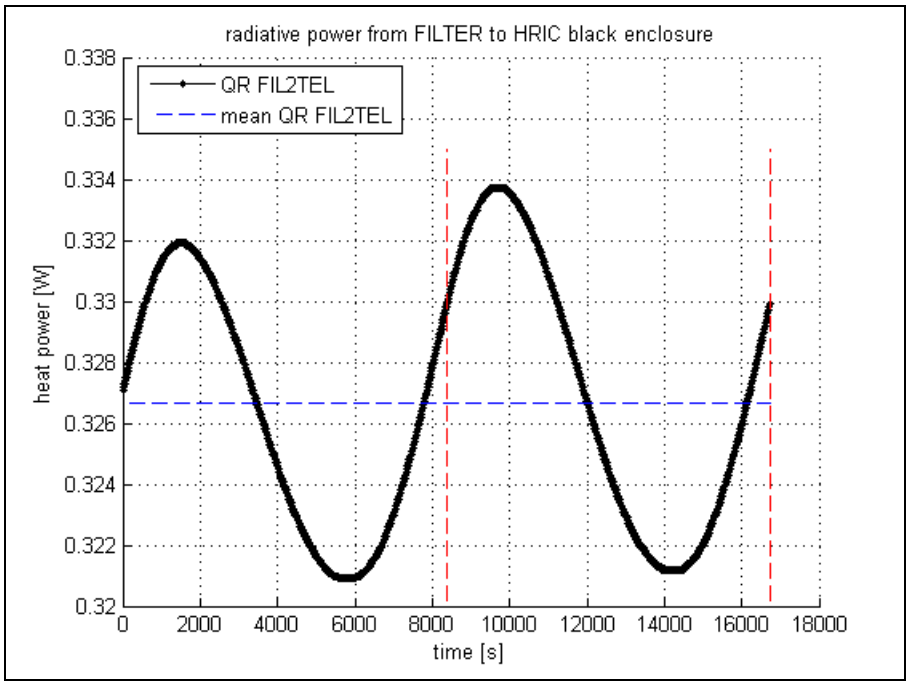

Figure 6.33: radiative power from filter to HRIC black enclosure (Spring/Autumn)

In the following tables are reported the average orbital heat loads among the orbit and the mean values of temperature at nodes (steady state solution). Quantities are those defined in [3] (see paragraph 6.1).

HRIC steady state Heat Loads [W] (Spring/Autumn)						
Qenv	**Qref**	**Qrad,baffle**	**Qcon,baffle**	**Qins**	**Qins, ind**	**Qins, env**
33.5	30.0	-0.2	3.4	0.3	0.3	0.01

Table 6.18

HRIC steady state temperatures [°C] (Spring/Autumn)				
$T_{R,SC}$ Boundary node	T_{BB} Boundary node	T_{BO} Boundary node	**Tbaffle (mean)**	**Tfilter (mean)**
-30	-40	-10	-31.2	-1.5

Table 6.19

It can be seen that the baffling system will reject around the 90% of the heat coming from the environment.

6.4 STC and VIHI baffles thermal analysis and results

6.4.1 Nodal breakdown and thermo-optical properties

A thermal mathematical model of STC and VIHI baffles has been implemented in ESARAD/ESATAN software in order to estimate the temperature distribution and heat transfer main paths.

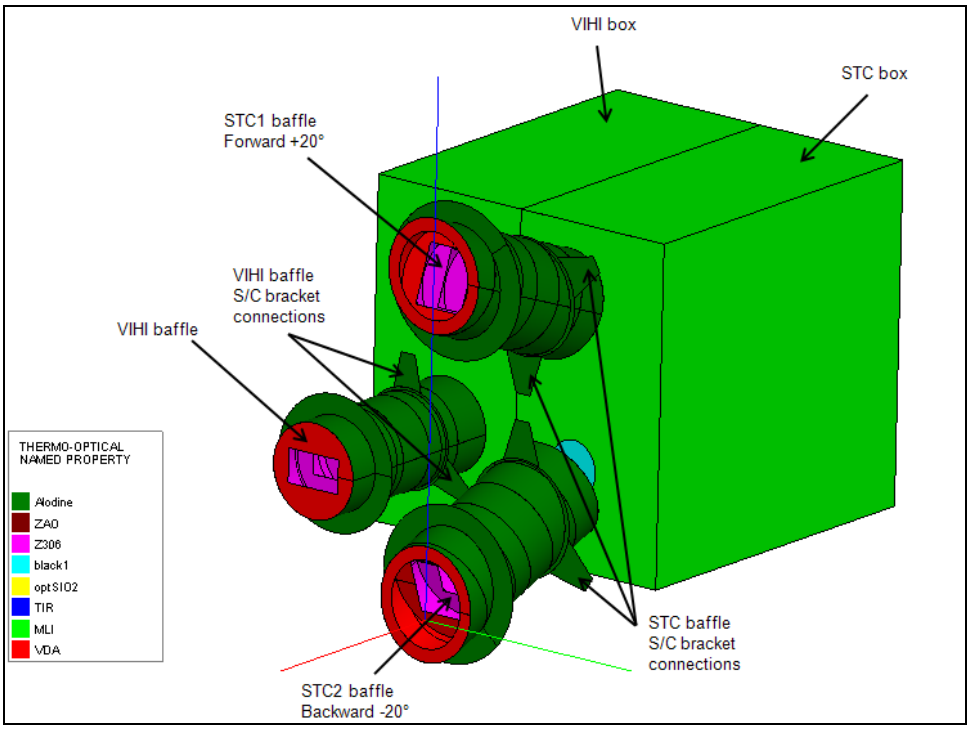

Figure 6.34: STC and VIHI baffle thermal model

At present the STC and VIHI baffle are foreseen to be made of aluminum Al 7075 alloy with properties as indicated in *Table 6.21*. Referring to *Figure 6.34*, the internal vane of the baffle will be coated of Z306 (aeroglaze) as classically made in the design of baffles of imaging system to absorb unwanted light coming from the environment. Externally the baffles will be alodined (*Table 6.20*). In order to increase the rejection capability of the baffles, the external surface of the frontal part will be of VDA (Vapor Deposited Aluminum) with thermo- optical properties reported in *Table 6.20*. The frontal ring of STC baffle , introduced after analysis reported in *Chapter 5.3*, will be externally of VDA and internally of aeroglaze.

The configuration herein analyzed does not foresee filters neither for STC nor for VIHI channel, even though the design option of having filters at the telescope entrance is still open, in particular for STC channel.

Since ESATAN software does not automatically calculates conductive links between shells with non rectilinear interface, conductive links between nodes will be hand calculated and star to triangle transformations will be used to calculate conduction between three or more shells converging at the same edge.

Node #	Name	Thermo-optical	ε	ρ_{IR}^{d}	τ_{IR}	α	ρ_{S}^{d}	τ_{S}	ρ_{IR}^{s}	ρ_{S}^{s}
641000-655300	VIHI baffle (int.)	Z306 (aeroglaze)	0.90	0.10	0.00	0.95	0.05	0.00	0.00	0.00
641000-655300	VIHI baffle (ext.)	Alodine	0.15	0.425	0.00	0.35	0.325	0.00	0.425	0.325
648000	VIHI baffle frontal disc (int.)	Z306 (aeroglaze)	0.90	0.10	0.00	0.95	0.05	0.00	0.00	0.00
648000	VIHI baffle frontal disc (ext.)	VDA	0.03	0.05	0.00	0.12	0.05	0.00	0.92	0.83
441000-455600	STC1 baffle (int.)	Z306 (aeroglaze)	0.90	0.10	0.00	0.95	0.05	0.00	0.00	0.00
441000-455600	STC1 baffle (ext.)	Alodine	0.15	0.425	0.00	0.35	0.325	0.00	0.425	0.325
455600	STC1 baffle frontal ring (int.)	Z306 (aeroglaze)	0.90	0.10	0.00	0.95	0.05	0.00	0.00	0.00
455600	STC1 baffle frontal ring (ext.)	VDA	0.03	0.05	0.00	0.12	0.05	0.00	0.92	0.83
541000-555600	STC2 baffle (int.)	Z306 (aeroglaze)	0.90	0.10	0.00	0.95	0.05	0.00	0.00	0.00
541000-555600	STC2 baffle (ext.)	Alodine	0.15	0.425	0.00	0.35	0.325	0.00	0.425	0.325
555600	STC2 baffle frontal ring (int.)	Z306 (aeroglaze)	0.90	0.10	0.00	0.95	0.05	0.00	0.00	0.00
555600	STC2 baffle frontal ring (ext.)	VDA	0.03	0.05	0.00	0.12	0.05	0.00	0.92	0.83
30000-30005	VIHI box (int.)	Black1	1.0	0.0	0.0	1.0	0.0	0.0	0.0	0.0
672000-672005	VIHI box (ext.)	MLI (kvda)	0.05	0.95	0.00	0.15	0.85	0.00	0.00	0.00
20000-20005	STC box (int.)	Black1	1.0	0.0	0.0	1.0	0.0	0.0	0.0	0.0
472000-472005	STC box (ext.)	MLI (kvda)	0.05	0.95	0.00	0.15	0.85	0.00	0.00	0.00
5000-5006; 6000	S/C int. environment	Black1	1.0	0.0	0.0	1.0	0.0	0.0	0.0	0.0

Table 6.20: Nodes and thermo-optical properties

Name	Material	Heat capacity c_p [J/(kg K)]	Density ρ [kg/m^3]	Thermal conductivity k [W/(m K)]
VIHI baffle	Al 7075	2800	850	130
STC1 baffle	Al 7075	2800	850	130
STC2 baffle	Al 7075	2800	850	130
MLI unit cover	MLI foil	0.0	0.0	0.7

Table 6.21: nodes and bulk material properties

6.4.2 Analysis cases and results of thermal simulations

In the following paragraph are reported the results of thermal simulations performed. It will be presented mean and peak temperature distribution obtained for critical radiative cases and afterwards graphs of temperatures of STC and VIHI baffle nodes during two subsequent orbits. Since the algorithm implemented in ESATAN integrates the system of nonlinear differential equations taking as initial condition the steady state solution of the thermal network, two subsequent orbits are taken to allow the solution to replicate temperature distribution at the beginning and at the end of the orbit.

The heat balance loads for the baffling subsystem, with reference to equation (96) , will be reported in tables. The balance refers to steady state solution (average among the orbit), with quantity defined in [3] (see paragraph 6.1). The average heat power at interfaces and the heat load entering the instrument will be reported. These quantities are: the total conductive heat power from baffle nodes to S/C bracket ($Q_{CON,baffle}$), the total radiative heat power from baffle's nodes to S/C radiative environment ($Q_{RAD,baffle}$) and the average heat load entering the unit Q_{INS} which is the sum of heat loads entering the instrument aperture either directly ($Q_{INS,ENV}$) or by baffles induced effects ($Q_{INS,IND}$). The average environmental thermal inputs Q_{ENV} have been also computed in order to evaluate the rejection capability of the baffling system.

6.4.2.1 APHELION reference orbit

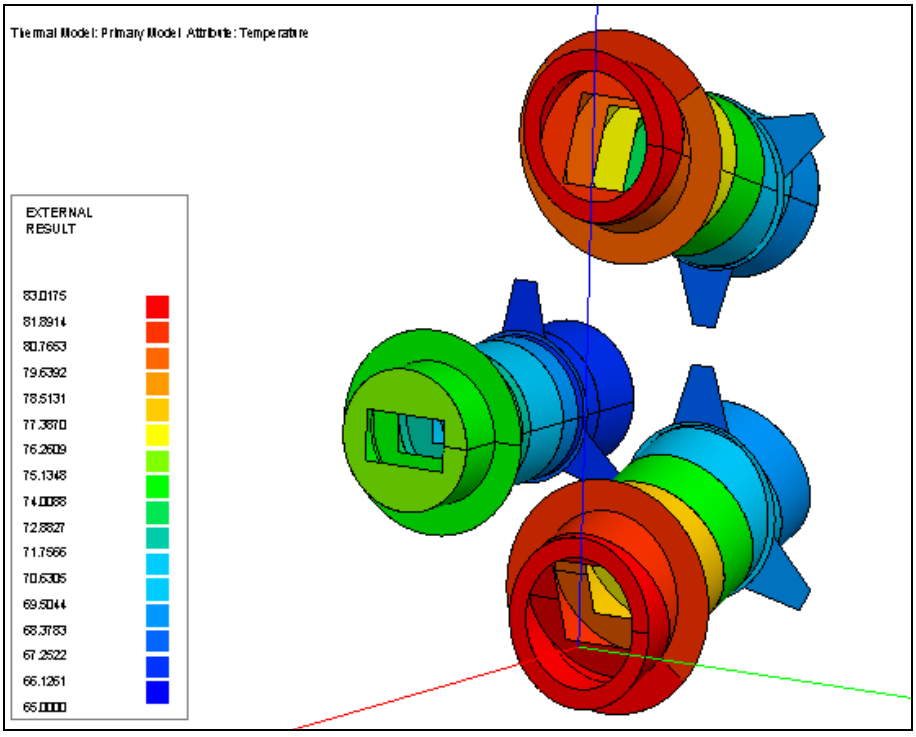

Figure 6.35: STC and VIHI baffles steady state temperatures (Aphelion)

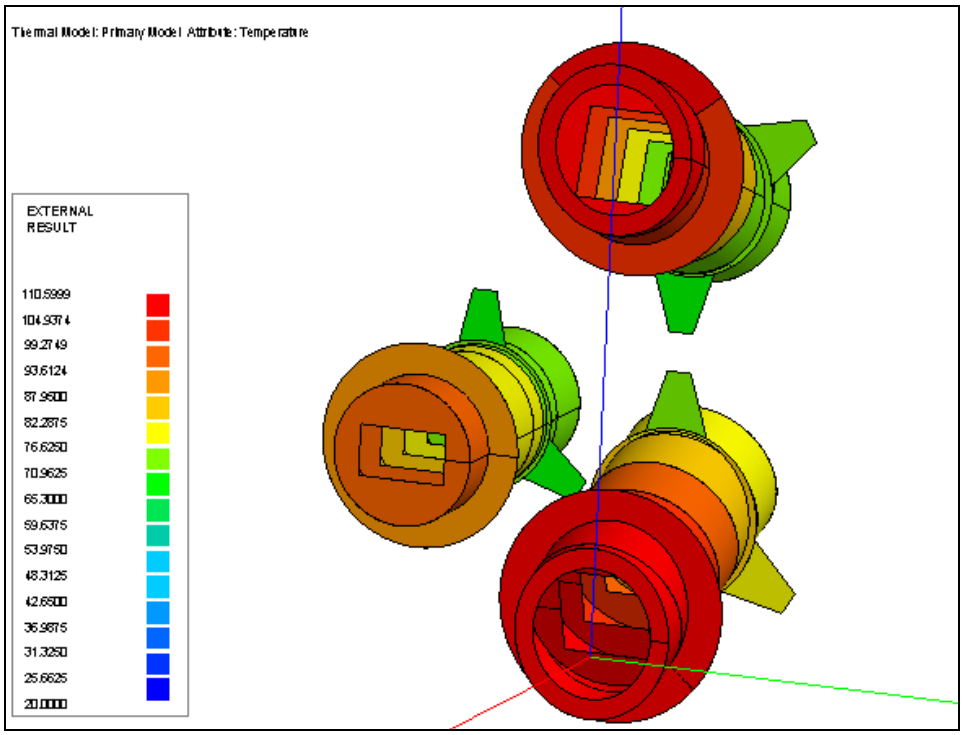

Figure 6.36: STC and VIHI baffles peak temperatures during Aphelion orbit (at t = 11300 s)

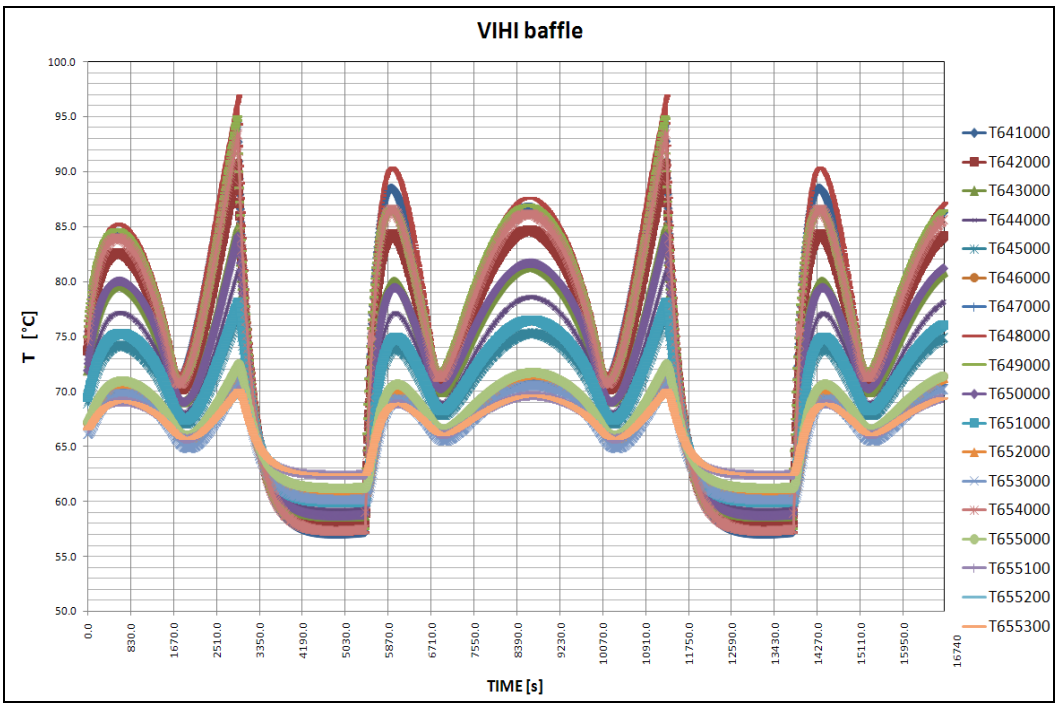

Figure 6.37: Temperature of VIHI baffle nodes (Aphelion)

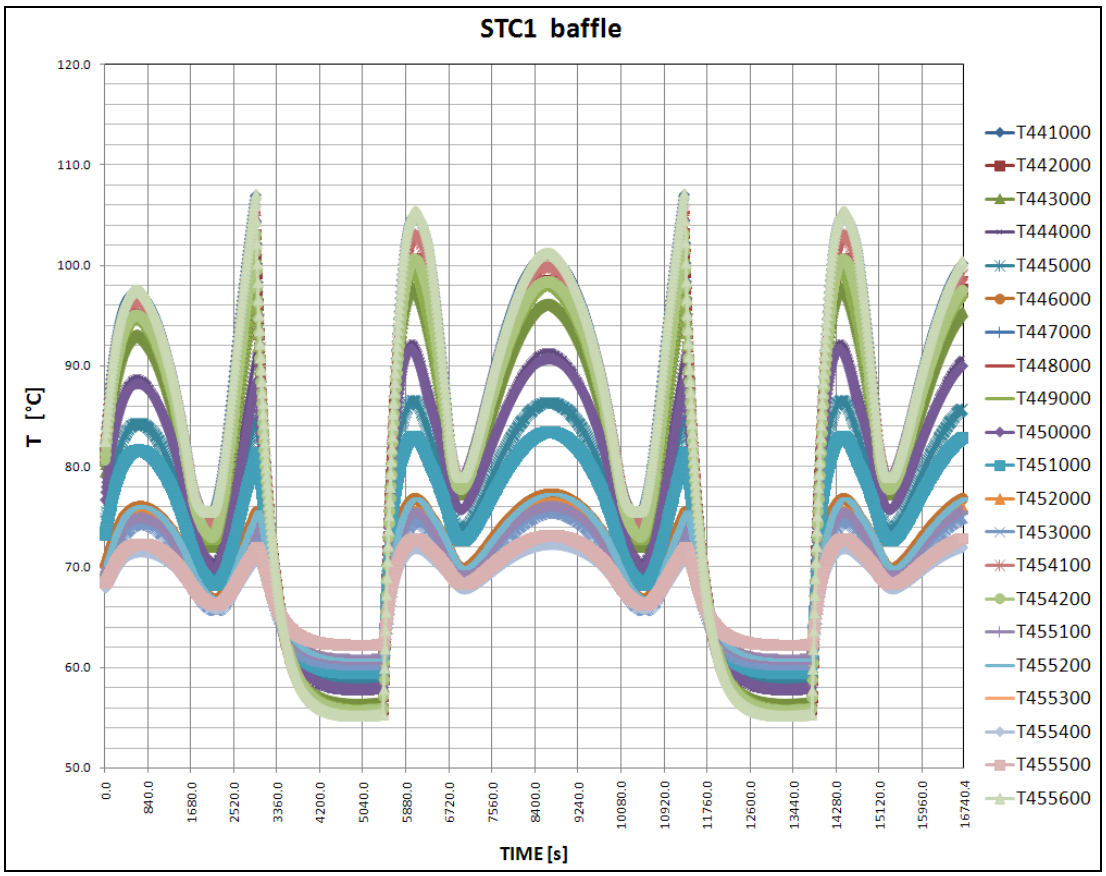

Figure 6.38: Temperature of STC1 baffle nodes (Aphelion)

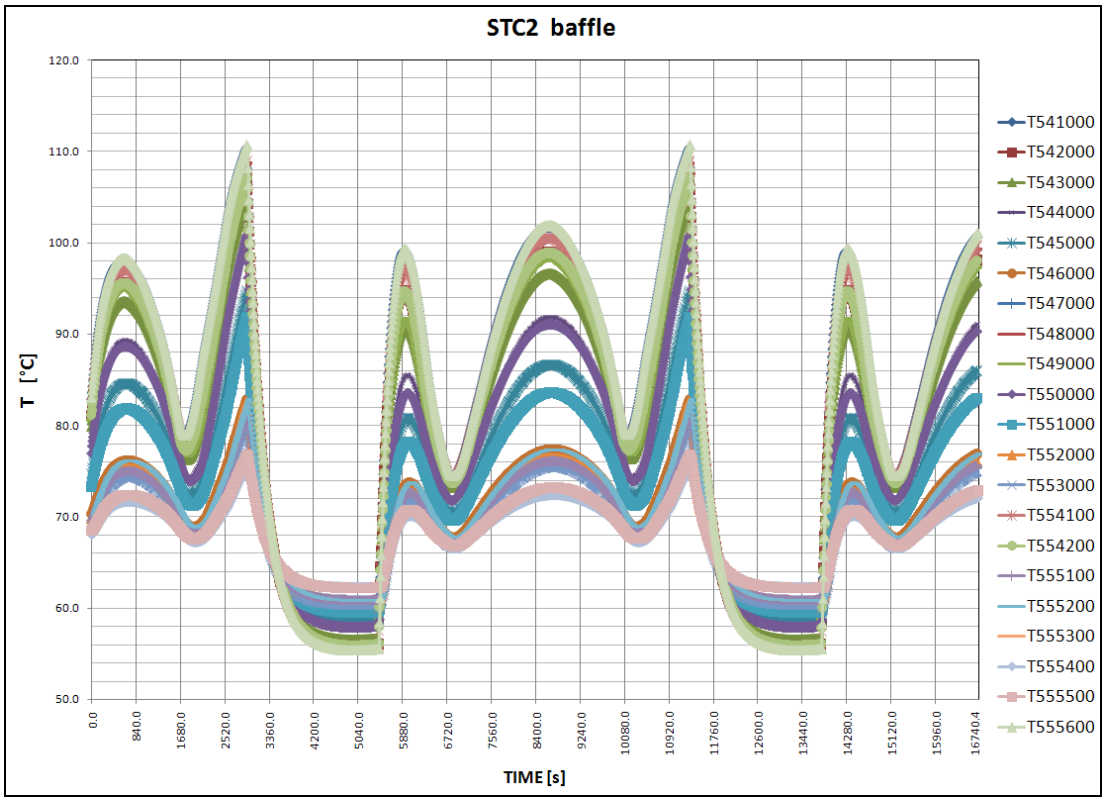

Figure 6.39: Temperature of STC2 baffle nodes (Aphelion)

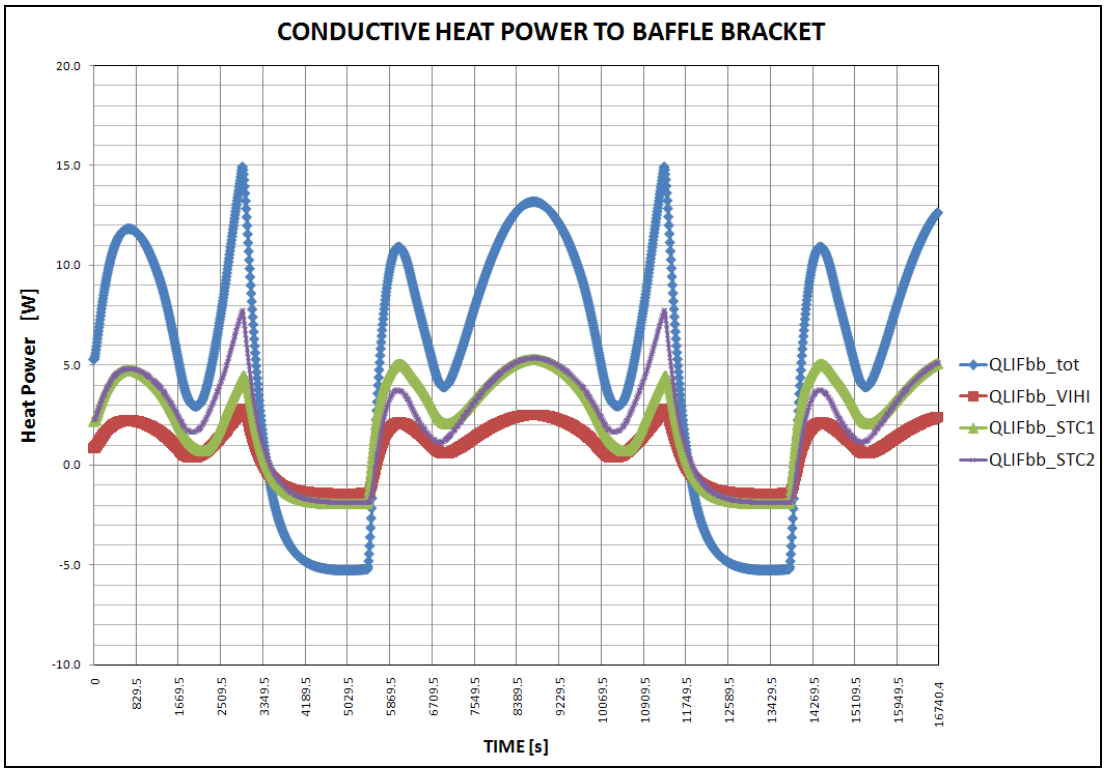

Figure 6.40: Conductive heat power from STC and VIHI baffles to S/C bracket (Aphelion)

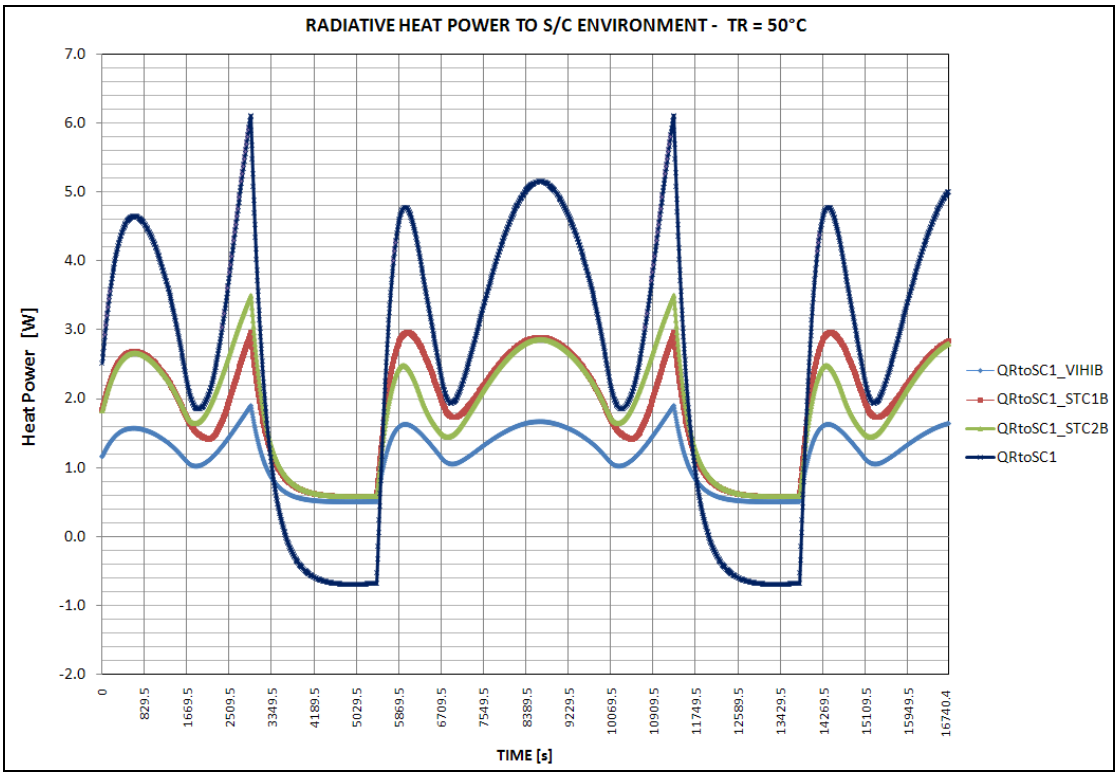

Figure 6.41: Radiative heat power from STC and VIHI baffles to S/C radiative environment (Aphelion)

In the following tables are reported the average orbital heat loads among the orbit and the mean values of temperature at nodes (steady state solution). Quantities are those defined in [3] (see paragraph 6.1).

VIHI baffle steady state Heat Loads [W] (Aphelion)						
Q_{ENV}	Q_{REF}	$Q_{RAD,baffle}$	$Q_{CON,baffle}$	Q_{INS}	$Q_{INS,ind}$	$Q_{INS,env}$
9.3	6.8	1.2	0.8	0.4	0.4	0.02

Table 6.22

STC baffles steady state Heat Loads [W] (Aphelion)					
$Q_{RAD,baffle}$	$Q_{RAD,bafSTC1}$	$Q_{RAD,bafSTC2}$	$Q_{CON,baffle}$	$Q_{CON,bafSTC1}$	$Q_{CON,bafSTC2}$
3.7	1.8	1.8	**4.5**	2.2	2.3

Q_{ENV}	Q_{ENV_STC1}	Q_{ENV_STC2}
25.2	12.6	12.6

Table 6.23

STC baffles total steady state Heat Loads [W] (Aphelion)						
Q_{ENV}	Q_{REF}	$Q_{RAD,baffle}$	$Q_{CON,baffle}$	Q_{INS}	$Q_{INS,ind}$	$Q_{INS,env}$
25.2	16.3	3.7	4.5	0.8	0.7	0.1

Table 6.24

It can be seen that the VIHI baffle will reject around the 74%, while the STC baffles will reject around the 64% of the incoming power from the environment.

VIHI & STC steady state temperatures [°C] (Aphelion)					
$T_{R,SC}$ Boundary node	T_{BB} Boundary node	T_{BO} Boundary node	**Tbaffle VIHI (mean)**	**Tbaffle STC1/H (mean)**	**Tbaffle STC2/L (mean)**
+50	+65	+20	+70.0	+74.9	+75.2

Table 6.25

6.4.2.2 PERIHELION reference orbit

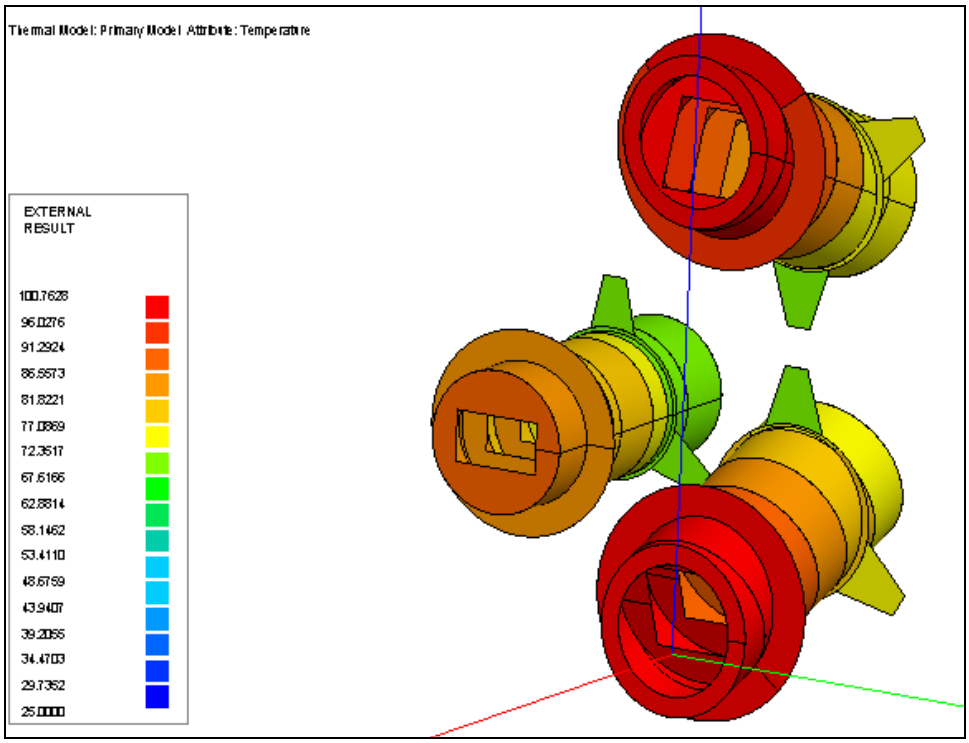

Figure 6.42: STC and VIHI baffles steady state temperatures (Perihelion)

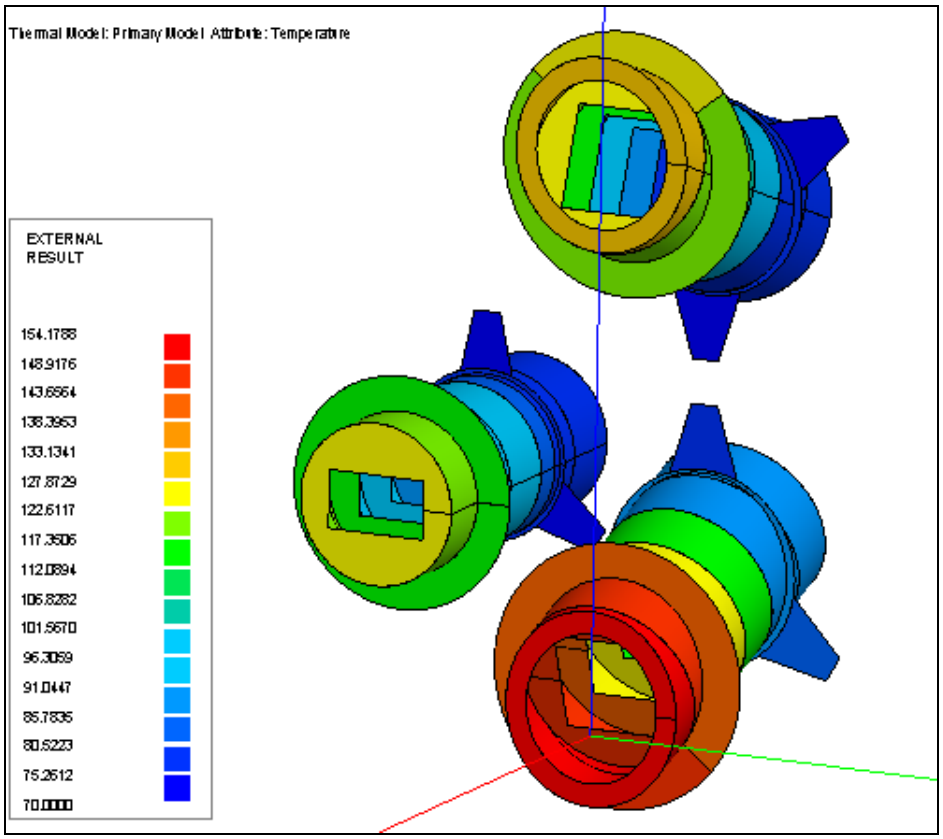

Figure 6.43: STC and VIHI baffles peak temperatures during Perihelion orbit (at t = 15810 s)

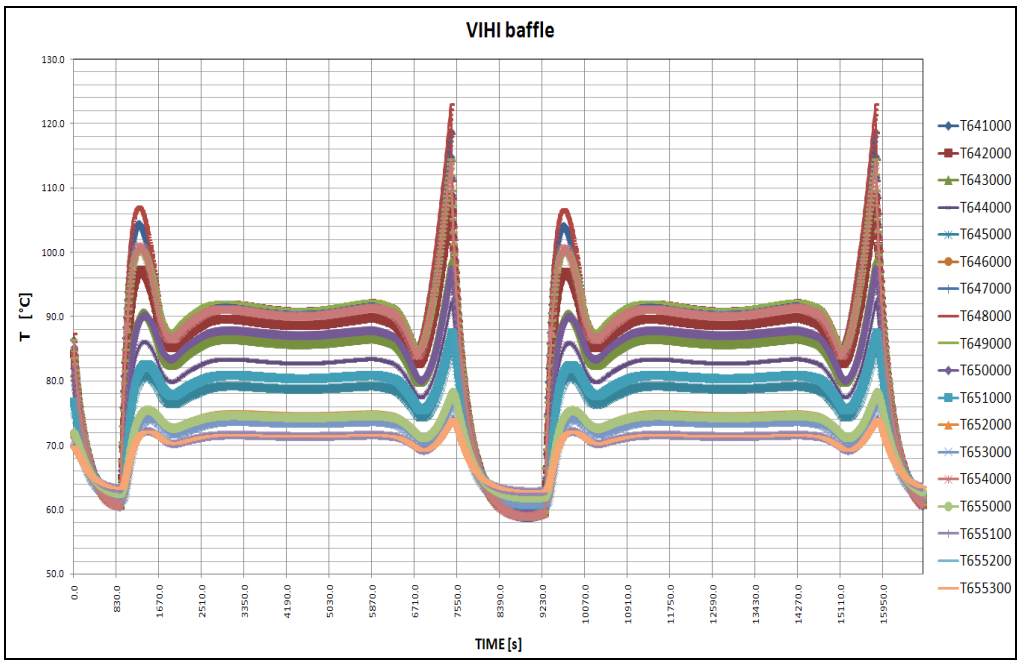

Figure 6.44: Temperature of VIHI baffle nodes (Perihelion)

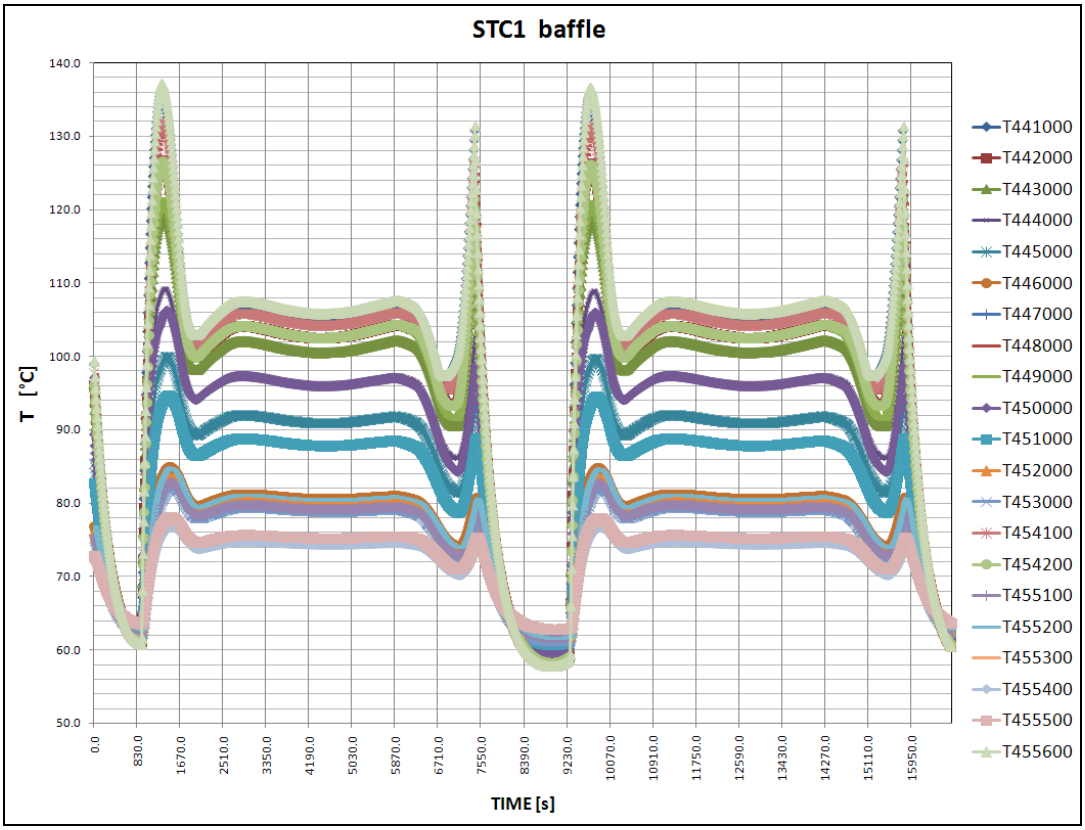

Figure 6.45: Temperature of STC1 baffle nodes (Perihelion)

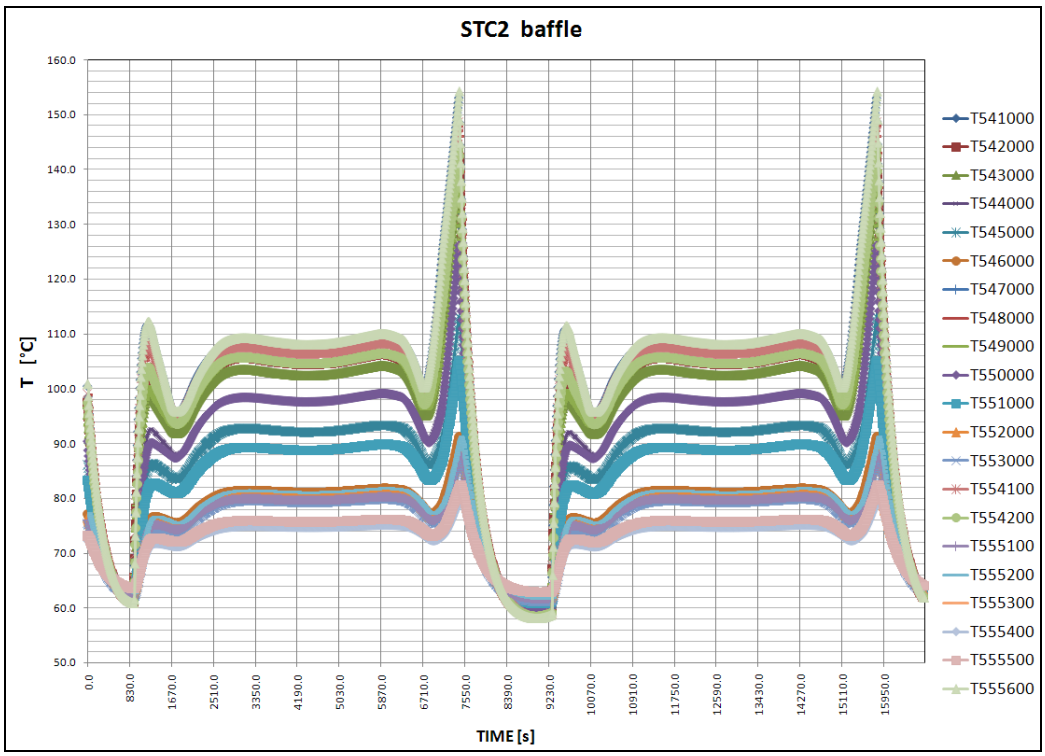

Figure 6.46: Temperature of STC2 baffle nodes (Perihelion)

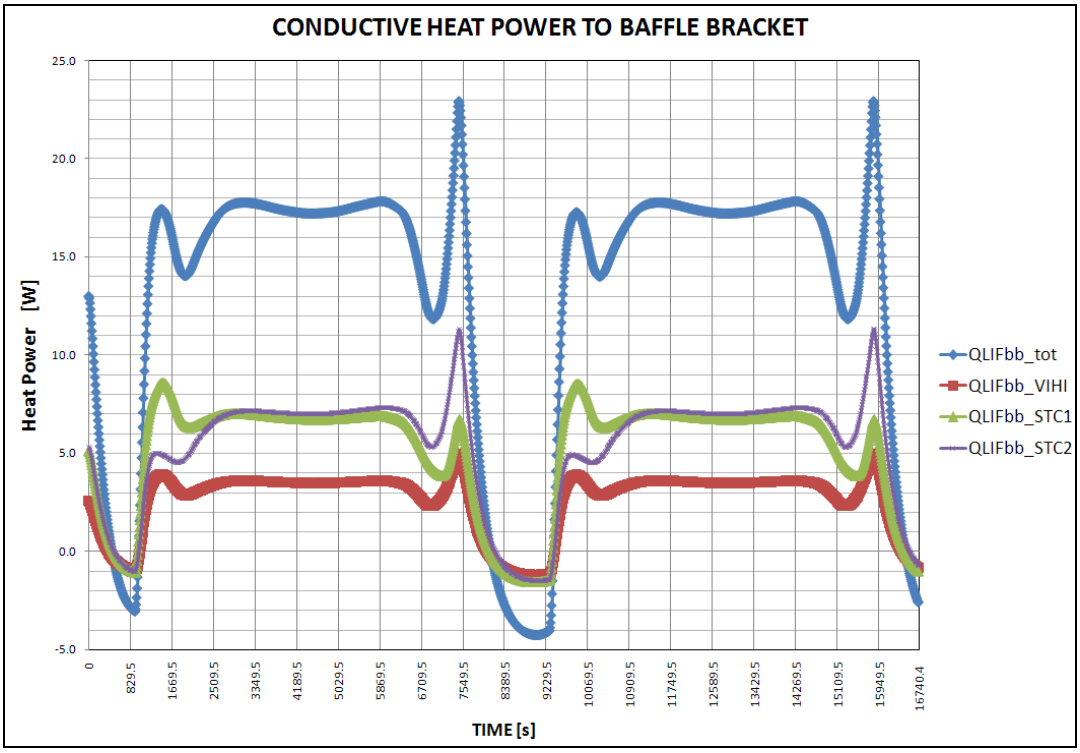

Figure 6.47: Conductive heat power from STC and VIHI baffles to S/C bracket (Perihelion)

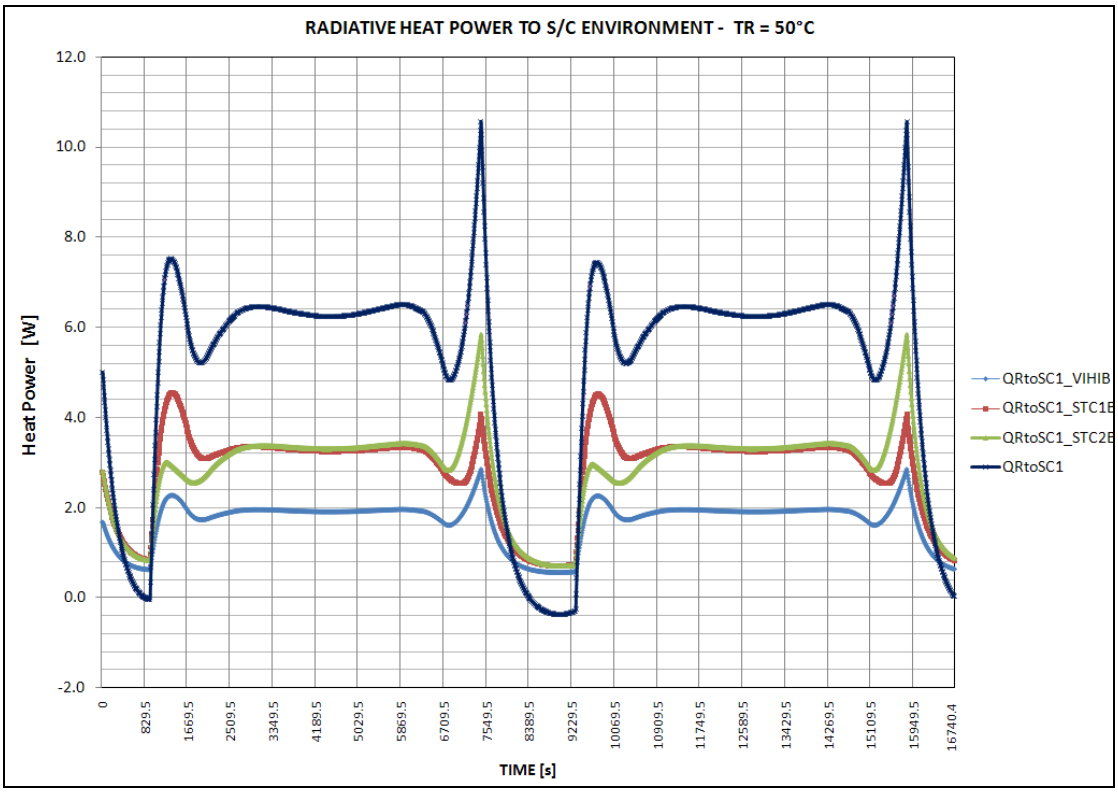

Figure 6.48: Radiative heat power from STC and VIHI baffles to S/C radiative environment (Perihelion)

In the following tables are reported the average orbital heat loads among the orbit and the mean values of temperature at nodes (steady state solution). Quantities are those defined in [3] (see paragraph 6.1).

VIHI baffle steady state Heat Loads [W] (Perihelion)						
Q_{ENV}	Q_{REF}	$Q_{RAD,baffle}$	$Q_{CON,baffle}$	Q_{INS}	$Q_{INS,ind}$	$Q_{INS,env}$
16.0	11.3	1.7	2.6	0.5	0.4	0.05

Table 6.26

STC baffles steady state Heat Loads [W] (Perihelion)					
$Q_{RAD,baffle}$	$Q_{RAD,bafSTC1}$	$Q_{RAD,bafSTC2}$	$Q_{CON,baffle}$	$Q_{CON,bafSTC1}$	$Q_{CON,bafSTC2}$
5.6	2.8	2.8	**10.4**	5.1	5.3

Q_{ENV}	Q_{ENV_STC1}	Q_{ENV_STC2}
43.7	21.7	22.0

Table 6.27

STC baffles total steady state Heat Loads [W] (Perihelion)						
Q_{ENV}	Q_{REF}	$Q_{RAD,baffle}$	$Q_{CON,baffle}$	Q_{INS}	$Q_{INS,ind}$	$Q_{INS,env}$
43.7	26.7	5.6	10.4	0.8	0.3	0.8

Table 6.28

It can be seen that the VIHI baffle will reject around the 71%, while the STC baffles will reject the 61% of the incoming power from the environment.

VIHI & STC steady state temperatures [°C] (Perihelion PH _REF)					
$T_{R,SC}$ Boundary node	T_{BB} Boundary node	T_{BO} Boundary node	**Tbaffle VIHI (mean)**	**Tbaffle STC1/H (mean)**	**Tbaffle STC2/L (mean)**
+50	+65	+25	+77.3	+84.8	+85.6

Table 6.29

6.4.2.3 SPRING / AUTUMN reference orbit

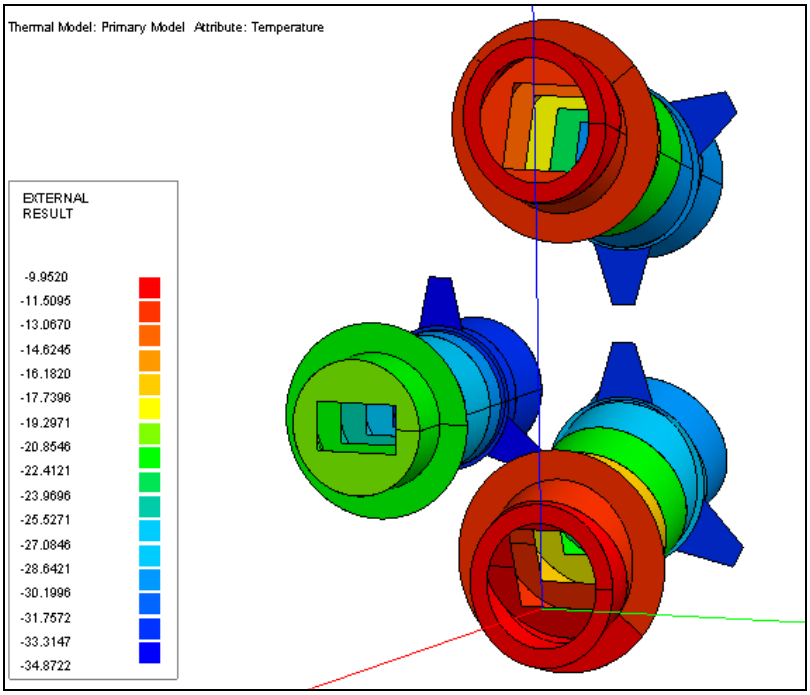

Figure 6.49: STC and VIHI baffles steady state temperatures (Spring/Autumn)

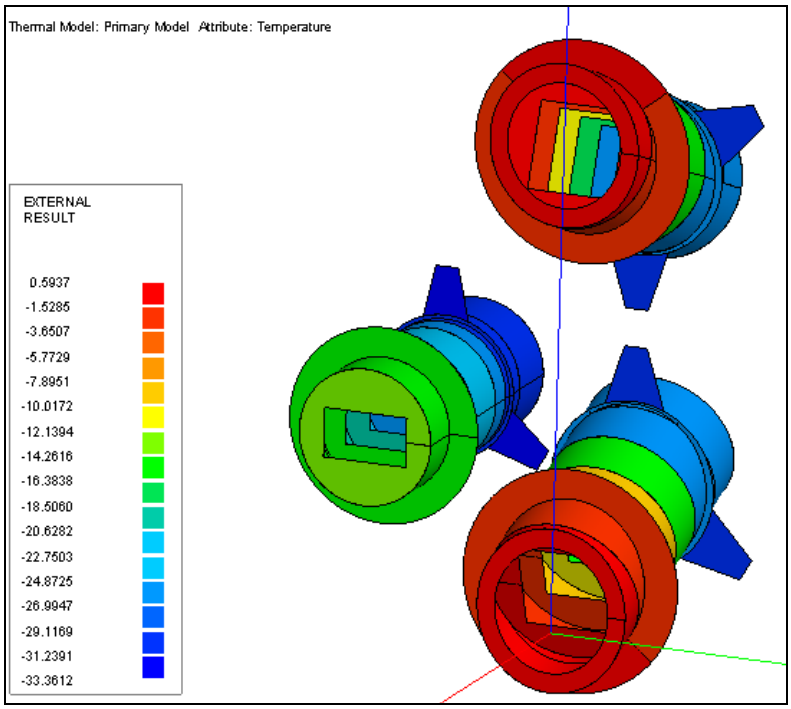

Figure 6.50: STC and VIHI baffles peak temperatures during Spring/Autumn orbit (at t = 9130 s)

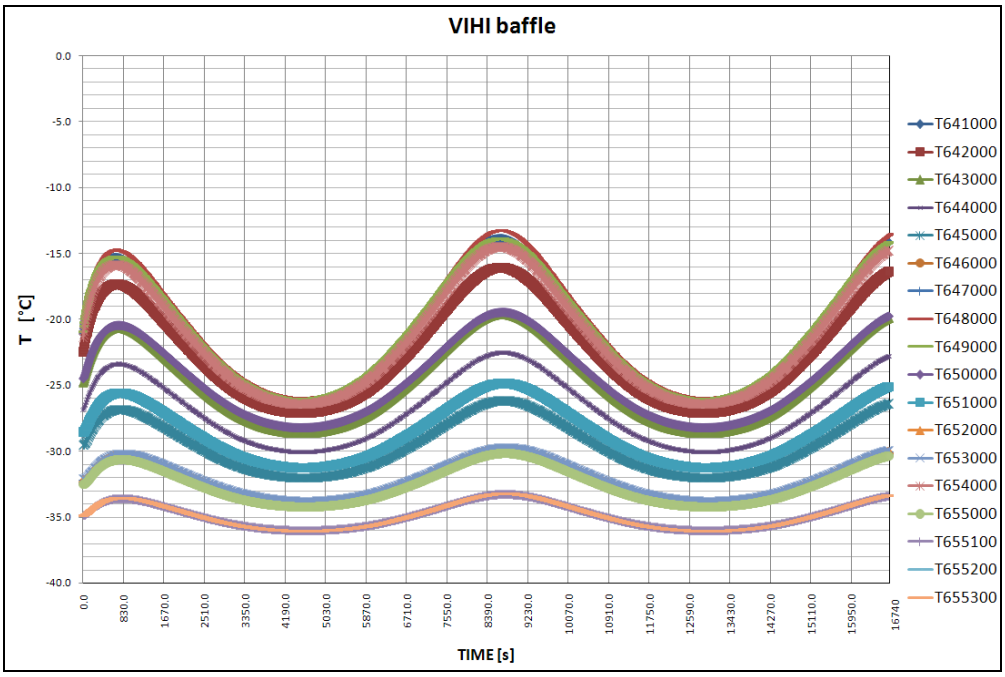

Figure 6.51: Temperature of VIHI baffle nodes (Spring/Autumn)

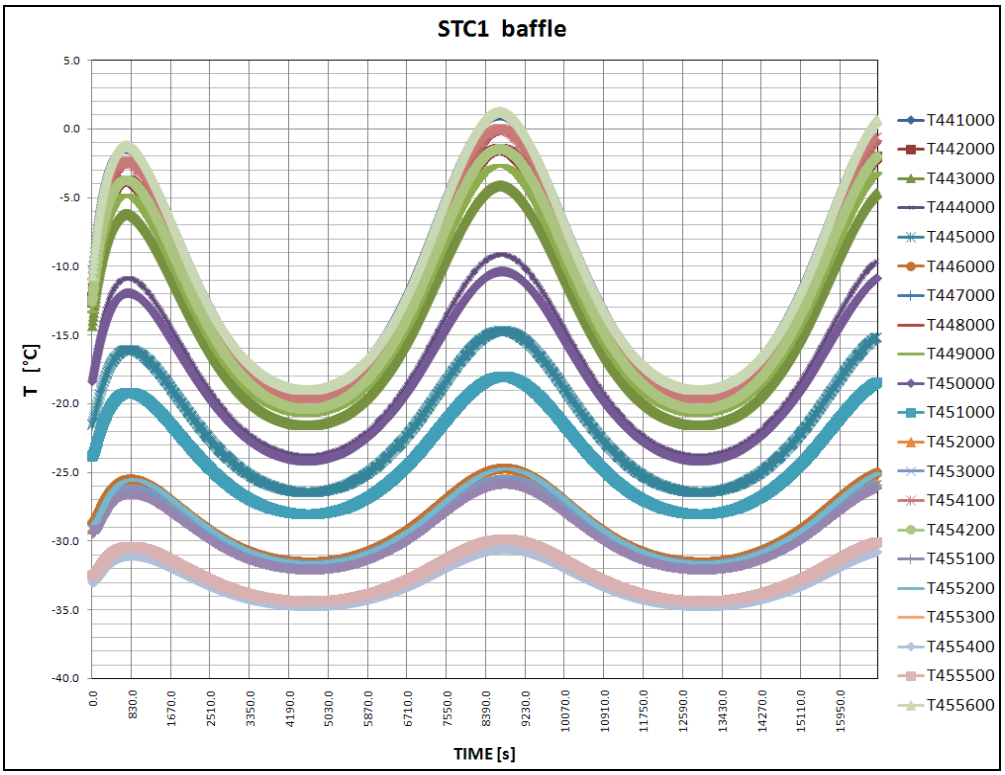

Figure 6.52: Temperature of STC1 baffle nodes (Spring/Autumn)

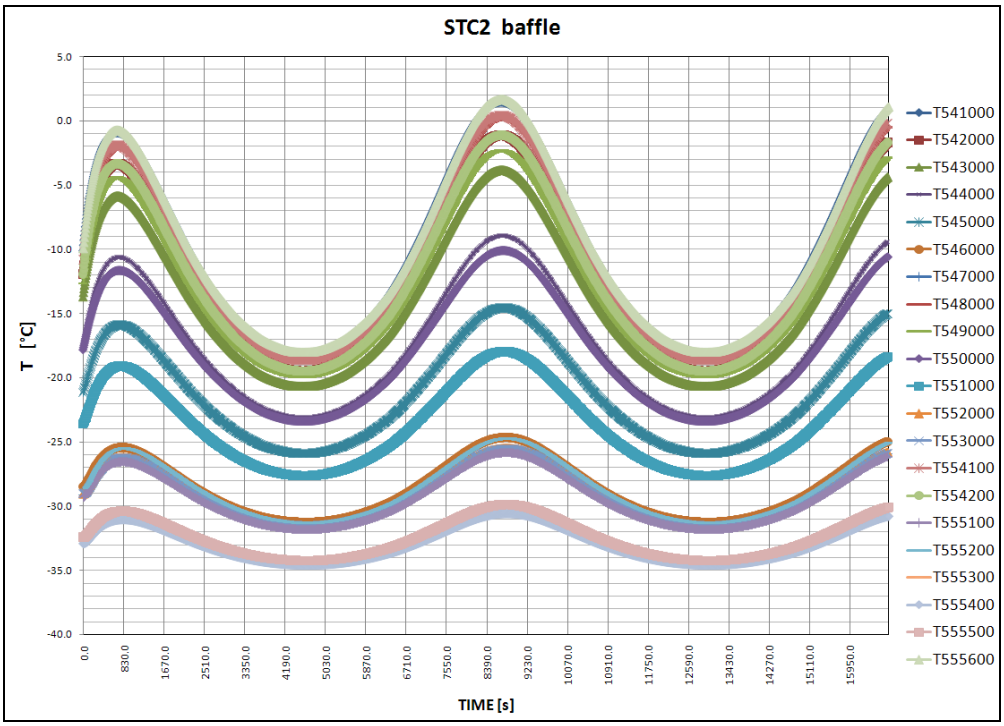

Figure 6.53: Temperature of STC2 baffle nodes (Spring/Autumn)

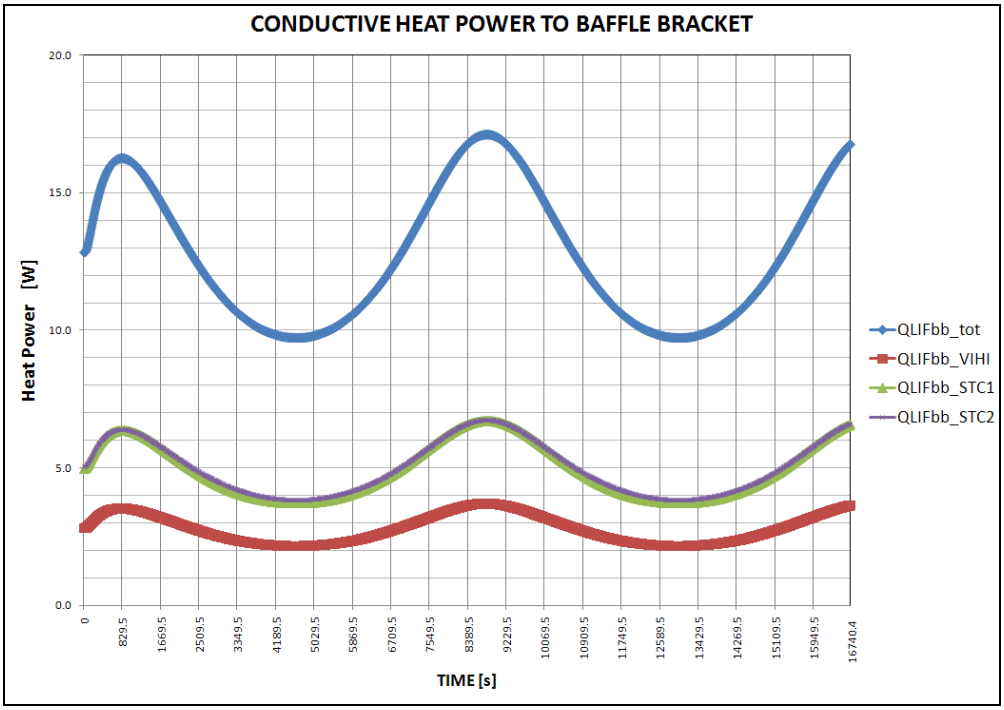

Figure 6.54: Conductive heat power from STC and VIHI baffles to S/C bracket (Spring/Autumn)

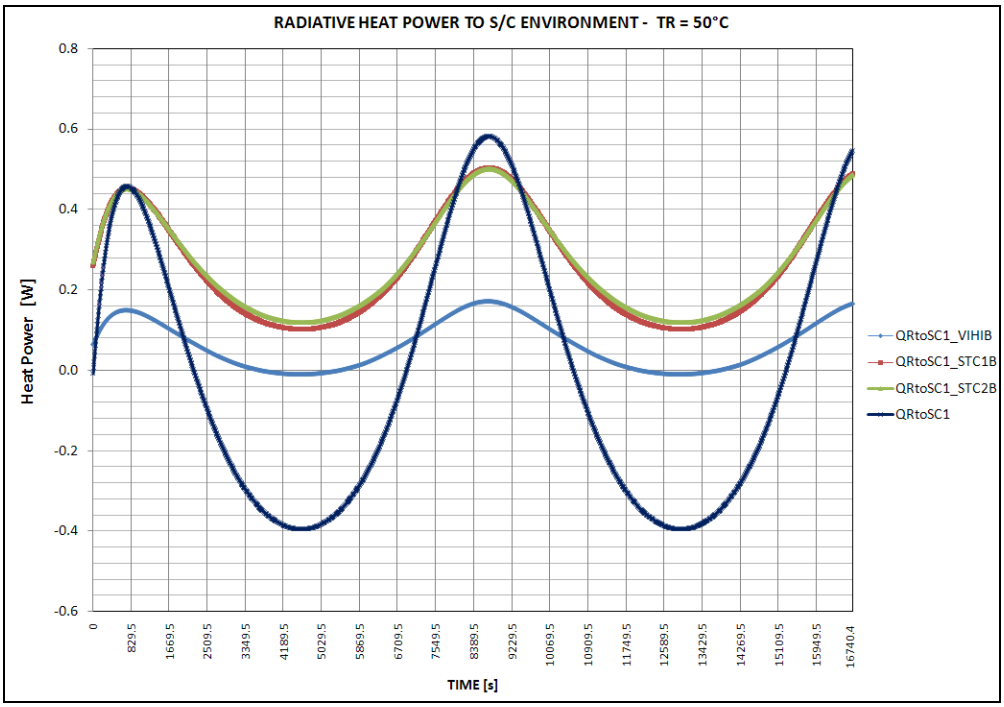

Figure 6.55: Radiative heat power from STC and VIHI baffles to S/C radiative environment (Spring/Autumn)

In the following tables are reported the average orbital heat loads among the orbit and the mean values of temperature at nodes (steady state solution). Quantities are those defined in [3] (see paragraph 6.1).

VIHI baffle steady state Heat Loads [W] (Spring/Autumn)						
Q_{ENV}	Q_{REF}	$Q_{RAD,baffle}$	$Q_{CON,baffle}$	Q_{INS}	$Q_{INS,ind}$	$Q_{INS,env}$
8.9	6.1	0.1	2.8	-0.1	-0.1	0.03

Table 6.30

STC baffles steady state Heat Loads [W] (Spring/Autumn)					
$Q_{RAD,baffle}$	$Q_{RAD,bafSTC1}$	$Q_{RAD,bafSTC2}$	$Q_{CON,baffle}$	$Q_{CON,bafSTC1}$	$Q_{CON,bafSTC2}$
0.6	0.3	0.3	**10.0**	5.0	5.0

Q_{ENV}	Q_{ENV_STC1}	Q_{ENV_STC2}
24.1	12.0	12.1

Table 6.31

STC baffles total steady state Heat Loads [W] (Spring/Autumn)						
Q_{ENV}	Q_{REF}	$Q_{RAD,baffle}$	$Q_{CON,baffle}$	Q_{INS}	$Q_{INS,ind}$	$Q_{INS,env}$
24.1	13.6	0.6	10.0	0.0	-0.2	0.2

Table 6.32

It can be seen that the VIHI baffle will reject around the 68% , while the STC baffles will reject the 56% of the incoming power from the environment.

VIHI & STC steady state temperatures [°C] (Spring/Autumn SP _REF)					
$T_{R,SC}$ Boundary node	T_{BB} Boundary node	T_{BO} Boundary node	**Tbaffle VIHI (mean)**	**Tbaffle STC1/H (mean)**	**Tbaffle STC2/L (mean)**
-30	-40	-10	-28.2	-21.5	-21.1

Table 6.33

6.5 Thermal analysis results outlook and conclusions

Thermal model of the baffling subsystem for the three channels have been performed by the lumped parameter method using ESATAN commercial software package. Both steady state and transient solution has been obtained among the most critical orbits of the mission.

The HRIC Stavroudis highly reflective baffle and the thermal rejection filter behind it, reveal good performance in terms of heat power rejection capability, able to reflect up to the 90% of the incoming radiation from the Mercury environment. The heat loads to spacecraft thermal interfaces are within the limits foreseen for the mission and also the temperature range are within the specified component range (-40 / +100 °C). The sudden changes in the amount of heat power from the planet and the Sun, in particular for aphelion and perihelion radiative cases, results in extreme and fast variation of temperature among the light baffle structure and temperature differences within the baffle nodes can be up to about 30° at the eclipse terminator points. This could results in distortion due to thermal stress induced by temperature gradients and the geometry of the Stavroudis baffle will be modified and this could make worse the performance of the baffle. Thermo-structural analysis should be performed to estimate the performance drop of the baffle due to thermal gradients. The filter at the HRIC optics entrance allows to minimize the entrance of the infrared coming from the planet and the baffle itself, even if the optics will see the emitted IR radiation of the filter itself. The maximum temperature gradients within the filter (conductively isolated in the model) are limited to 1÷3°C between the nodes facing the optics and those looking outwards to the scene.

STC and VIHI baffle are conceived as usually for optical instruments: the unwanted light is scattered on diffuse black surfaces and eventually most of it is trapped within the baffle. From an optical point of view this concept will allow to easily manage the straylight but will make more difficult to reduce the absorbed heat load coming from the environment, and therefore the temperatures. Frontal surfaces of the baffles, facing the Mercury environment, will be coated (or eventually polished) to obtain high refection capability surface, in particular in the IR spectral range. This allows to obtain a baffling system that will have rejection capability equal up to about 65% for the STC baffles and up to 75% for the VIHI baffle.

7 MERCURY THERMAL ENVIRONMENT SIMULATOR TEST BED

To verify the thermal design and ensure successful operational use, space payloads are subjected to extensive ground thermal testing.
Thermal verification tests can be subdivided into two main varieties, those dedicated to confirming the validity of thermal control and those devised to affirm integrity of components. Ideally qualification tests expose design defects while acceptance tests uncover defects in workmanship, parts, materials and processes. In the validation tests the input is a predetermined heating load (usually satellite thermal interfaces and simulated orbital fluxes) with temperature as output to be compared and evaluated relative to predictions. Final validation before flight is through a thermal balance test, which is conducted to verify that the methods of analysis are legitimate and the temperature of the assembled components will indeed be within the mission requirements limits. A successful test and subsequent correlation to thermal analytic models establishes the ability of the thermal control to maintain equipment within the specified temperature limits for all mission phases. The thermal balance tests has provided successful in correcting major thermal modeling errors, in reducing the uncertainty between prediction and flight measurements and in providing physical insight into heat transfer mechanisms [15], [16].

Due to the extreme thermal environment of Mercury, test requirements should be tailored to the specific BepiColombo program and an experimental set-up for SIMBIO-SYS instrument thermal testing is under development at CISAS (University of Padova). It will consist of a thermal vacuum chamber (TVC) with heating and cooling sources to simulate the thermal environment that the SIMBIO-SYS units will face on orbit. The facility will be described in the following paragraph. An outlook of the test bed layout is illustrated in Figure 7.1 .

Thermal testing is more revealing when done in a vacuum as the absence of heat transfer by convection is likely to lead to results similar to those that would be encountered in space, then temperatures and stresses will more closely simulate on-flight conditions. Therefore thermal test will be performed in a vacuum chamber (air pressure in the 10^{-6} mbar range) equipped with heating sources and cryogenic surroundings for simulating orbital fluxes and space background. Furthermore a solar simulator is foreseen to simulate the solar flux at Mercury.

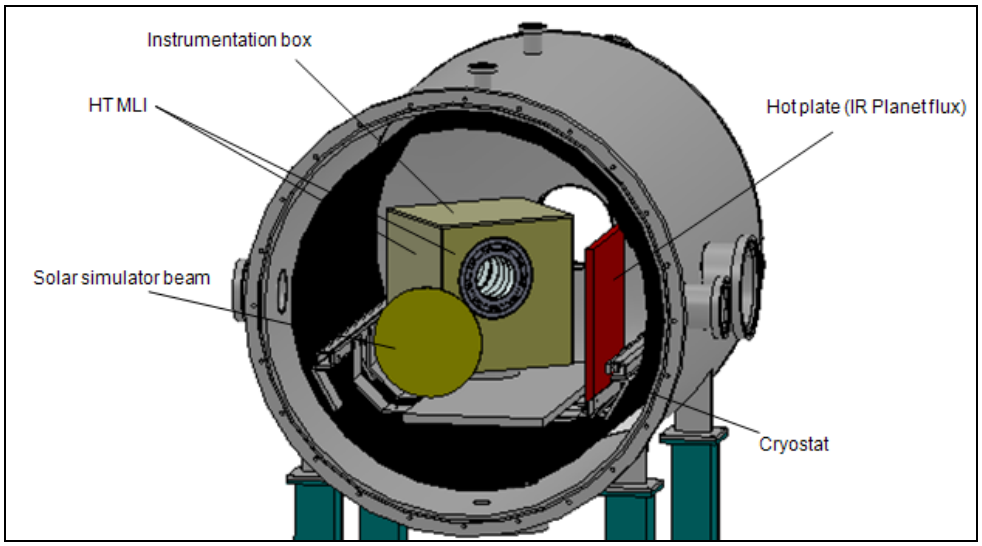

Figure 7.1:Mercury thermal environment simulator test bed

Methods for simulation of environmental heat loads are sometimes divided into two categories: absorbed flux and incident flux. In the design of this facility the incident fluxes approach will be used. The incident heat fluxes on the instrument during flight, previously calculated with method presented in Chapter 3 of this thesis , will be used as an input for the design of the test bed lay out to simulate the orbital fluxes.
The radiative heat sources that should be simulated are the solar, albedo and infrared planetary fluxes. Recalling the thermal test purpose of the facility, only the solar and planetary fluxes will be simulated, providing that the albedo has in general lower values during the orbits than the other sources and furthermore it is more difficult to simulate.

Referring to Figure 7.1 an heating shrouds, the so called hot plate, will simulate the IR planetary flux corresponding to Mercury hot side, the solar flux will be produced by a solar simulator and a cylindrical cryostat will simulate the cold planet surface and the sky background.

The solar environment will be handled by a solar simulator, which consist of a xenon arc lamp of 10 kW absorbed electrical power. The solar simulator system will be external to the thermal vacuum chamber and the simulator beam will enter the thermal vacuum chamber through a view port window of 270 mm diameter. The solar simulator system has been designed such that the solar beam entering the chamber will irradiate up to around 14kW/m^2 which corresponds to solar constant at Mercury at perihelion. A sketch of the solar simulator optical system is illustrated in Figure 7.2.

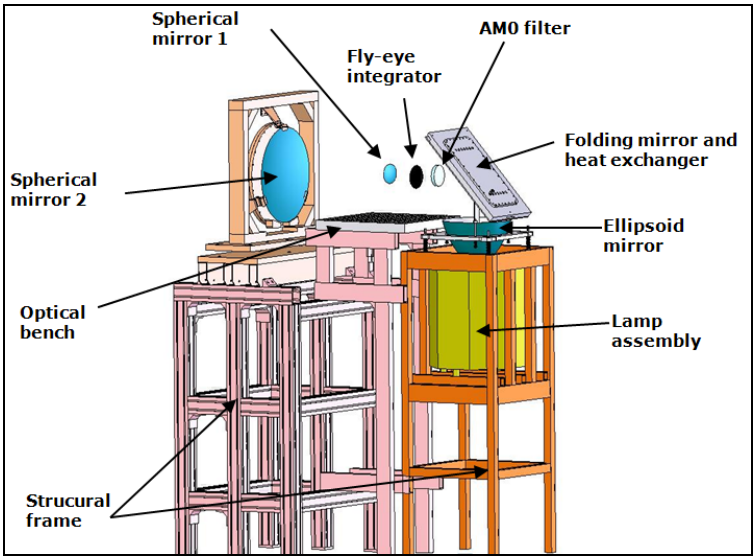

Figure 7.2: solar simulator lay-out

The heating shroud for IR flux simulation will be coated with high emissivity and placed laterally on the vacuum chamber, as close as possible in front of the instrument box. The target temperature is established by thermostatic control of bounded heaters while liquid nitrogen continuously flows through an integrated pipe system. The tubing layout will be designed to results in acceptable uniformity of shroud temperature.
Preliminary calculations on equivalent shroud temperature for simulating orbital fluxes have been made using classical radiative heat transfer equations. With a plate of area equal to 370x400 mm^2 and analytical formula of view factor between two facing rectangular surfaces (see for example [8]), given the dimensions of the chamber, the calculated maximum equivalent temperature of the heating shroud will be in the range 400÷450 °C to have an incident flux equal to the maximum planetary IR at perihelion (~4500 W/m^2). The minimum equivalent temperature would be in the range -140÷-150 °C to simulate the cold side of the planet. The cylindrical cryostat can reach a temperature of 90K. Detailed thermal modeling of simulation test bed with ESATAN software are under development.

The Mercury thermal environment simulator test bed will be used to perform thermal test in particular on SIMBIO-SYS baffles. The tests will be performed separately for Stavroudis HRIC baffle and for STC&VIHI baffles. STM and QM baffles will be placed in a (367x364x290) mm^3 box able to rotate thanks to a vacuum compatible motorized rotary stage, in order to expose the instrumentation to the different heat sources and to solar simulator beam angle corresponding to critical Sun incidence angle. The control volume is thermal insulated with High Temperature and Standard MLI: the HT MLI lies on the faces directly exposed to the solar simulator flux (frontal and lateral faces of the box respectively), standard MLI on the other faces.

Inside the control volume, baffles will be supported by an aluminium plate (10 mm thickness), which shall be provided with heating resistors and connected to the cryostat by a copper braid in order to adjust the plate temperature. This plate will represents the S/C baffle bracket interface and temperature will be equal to baffle brackets temperature (e.g. at Perihelium T = 65°C). The aluminium plate will be radiatively insulated thanks to MLI coverage from other internal components of instrumentation box. An aluminium box (2 mm thickness) will be located behind the aluminium plate and will be provided with heaters and copper braid connected to the cryostat, in order to set the internal temperature equal to T_R, which represents the radiative temperature of the spacecraft environment (e.g. at Perihelium T_R= 65°C). The box will be externally insulated by MLI.

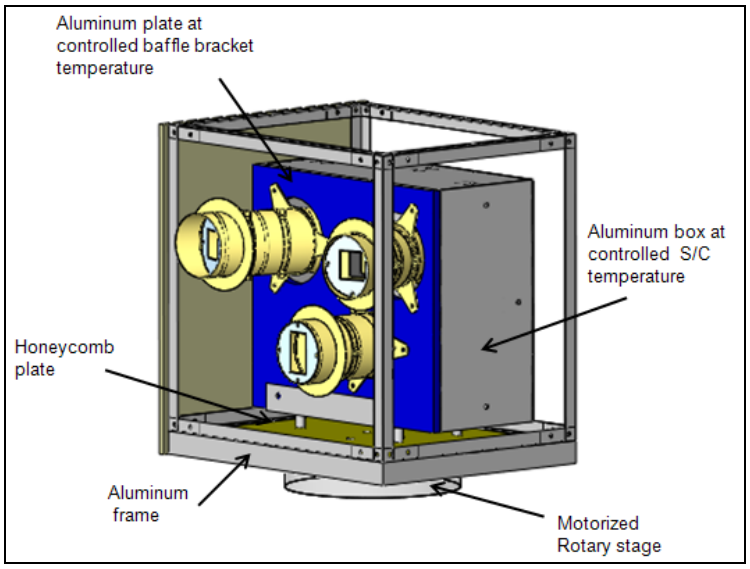

Figure 7.3: Instrumentation control volume

The described facility will allow to test the thermo-optical behavior of baffles and to simulate the most critical cases that will occur during flight. The kinematics and orientation of baffle model inside the vacuum chamber, will reproduce, as good as possible, the thermal environment encountered by the instrument orbiting Mercury.

The most critical cases for direct Sun illumination of baffles can be simulated thanks to the rotation capability of the rotary stage. The most critical solar incidence angle for baffles previously calculated (see chapters 4 and 5 of this thesis) can be therefore simulated as indicated in Figure 3.1for nadir pointing HRIC & VIHI units baffles and in Figure 7.5 for STC unit baffles. The minimum values of the Sun incidence angle θ_{SUN} will be taken from Table 4.4, Table 4.5, Table 4.6.

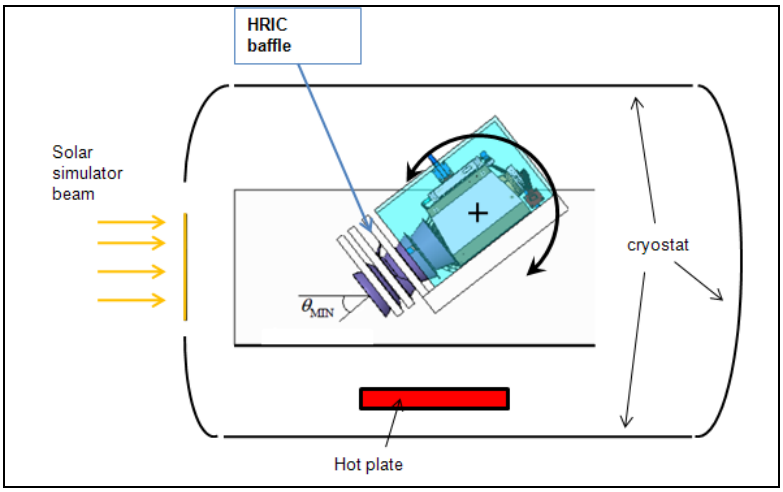

Figure 7.4: critical sun incidence angle simulation with test bed of nadir pointing baffles (HRIC, VIHI). $\theta_{MIN} = 38.2°$

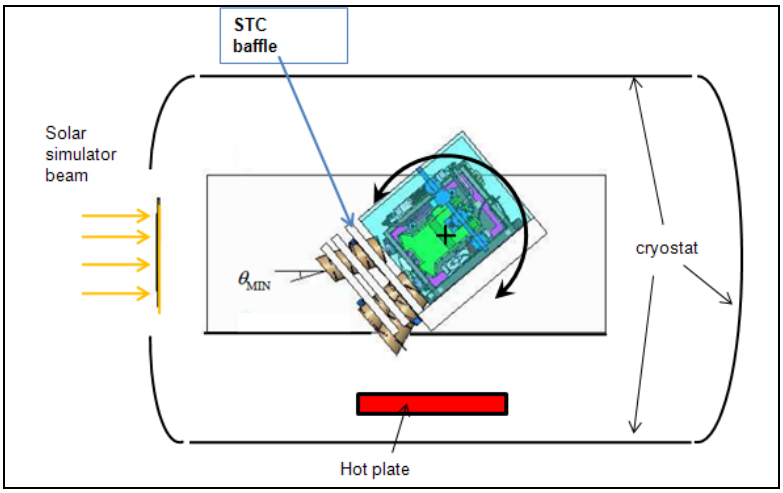

Figure 7.5: critical sun incidence angle simulation with test bed of STC off-nadir pointing baffles. $\theta_{MIN} = 18.7°$

The radiative heat sources will be characterized and calibrated to know the appropriate amount and spectral distribution of flux irradiated by the source. The solar simulator optical system in particular, will be characterized in terms of total irradiance and spectral distribution. To measure the total amount of heat flux irradiated by the source a Gardon heat flux sensor has been selected while spectroradiometric measurements are foreseen for the spectral characterization of the solar simulator beam entering the thermal vacuum chamber.

The foil type heat flux sensor (also known as Gardon heat flux gage after his inventor [26]) measures the heat transfer through a surface and produces an output that is proportional to the heat flux (W/m^2). The Gardon gage consist of a hollow cylinder of one thermocouple material with a thin circular foil of a second thermocouple material attached to one end. A wire of the first material is attached to the center of the foil to complete a differential thermocouple pair between the center and edge of the foil. The body and wire are commonly made of copper with the foil made of constantan. For a uniform incoming heat flux, the center to edge temperature difference is proportional to the heat flux with the formula [26]:

$$q = \frac{4k\delta}{R^2}\left(T_0 - T_s\right) \tag{101}$$

Where δ is the thickness of the foil, R the active radius of the foil, k is the thermal conductivity of the foil material, T_0 the temperature at the center of the foil and T_s the temperature at the periphery . The temperature difference produced from center to edge of the foil is measured by a single thermocouple pair, typically copper-constantan.

This lead to a sensor for direct measurement of incident heat flux to a surface, therefore this gage could be used to measure the incident heat flux on significant surfaces of the instrument control volume inside the Mercury simulator facility, for example the frontal surface of the baffle aperture, to make a measure of the overall incident fluxes produced by the test bed sources. Furthermore it could be used to experimentally evaluate the performance of the baffle, in particular the Stavroudis baffle, on the basis of the performance criterion previously defined in chapter 6.2.1. In fact, by positioning the sensor at the inner side of the frontal ring of the baffle and at a surface behind the baffle and comparison with the incident flux at the entrance it could be possible to have an experimental estimation of Stavroudis baffle performance.

8 CONCLUSIONS

This thesis work investigated reduction techniques of thermal effects for the SIMBIO-SYS scientific suite of BepiColombo mission. SIMBIO-SYS will have to operate in a very harsh environment, mainly from the thermal point of view. For this reason, state-of-art heat rejection baffles and filters have to be designed. A methodological approach has been used to overcome this issue.

Starting from the estimation of thermal environment encountered by the payload during mission, led to a deep knowledge of the heat loads that the instrument will face during the mission phases and provided a framework to the design of the payload baffling system. A mathematical model has been developed and simulations has been carried out to evaluate the incident fluxes on the front end of the payload during the orbiting of MPO spacecraft around Mercury. This allowed to rigorously identify the most critical cases from the thermal point of view.

Furthermore the Sun aspect angle of the optical axes of the three channels of SIMBIO-SYS has been assessed and the criticality during the various phases of the mission has been identified.
The geometry of the present configuration of the baffles have been be verified against direct Sun illumination and dedicated ray-casting algorithms have been implemented to verify the geometry and calculate the angular margin against direct entry of the Sun. The baffles of STC channel, which is the most critical to solar illumination since this channel have rectangular aperture and will point off-nadir (±20° forward/backward along track), has been verified and design modification has been proposed to overcome a too narrow margin to direct Sun illumination.

Thermal analyses and models have been carried out with lumped parameter thermal network method and implemented using ESARAD/ESATAN software to evaluate heat loads and temperature distribution among the baffling subsystem. This allows to predict main heat transfer mechanisms and temperature distribution on the baffling subsystem and to estimate the performance of baffles in terms of heat rejection capability.

The HRIC Stavroudis highly reflective baffle and the filter behind it, reveal good performance in terms of heat power rejection capability, able to reflect up to the 90% of the incoming radiation from the Mercury environment. The filter at the HRIC unit entrance allows to minimize the entrance of the infrared power coming from the planet and the baffle itself, even if the unit optics will see the IR radiation emitted by the filter. The maximum temperature gradients within the filter are limited to 1÷3 °C between the nodes facing the optics and those looking outwards to the scene. STC and VIHI baffle are conceived as classically diffuse black surfaces and therefore would show higher temperatures values and absorbed fluxes. Frontal surfaces of the baffles, facing the Mercury environment, will be a high reflection capability surface, in particular in the IR spectral range. This allows to obtain a baffling system that will have rejection capability equal up to about 65% for the STC baffles and up to 75% for the VIHI baffle. A study on the implementation on ESARAD software of the HRIC Stavroudis baffle allows to appropriate modeling this kind of geometry; furthermore this study led to the definition of a criterion to evaluate the performance of Stavroudis baffle and to guide the design of the most appropriate test bed to be used to evaluate its efficiency.

The lay-out of a Mercury thermal environment simulator facility has been designed on the basis of the study carried out, providing design drivers for the test bed. The facility is at present under development at CISAS (University of Padova) an will be used as an experimental set-up for SIMBIO-SYS baffles and instrument thermal testing. It will consist of a thermal vacuum chamber

with heating and cooling sources to simulate the thermal environment that the payload will face on orbit.

Activities foreseen in the future are the characterization and calibration of the radiative heat sources of the facility and the validation of baffles thermal mathematical models through experimental tests data. The radiative heat sources would be characterized and calibrated to know the appropriate amount and spectral distribution of flux irradiated by the source. The solar simulator optical system in particular, would be characterized in terms of total irradiance as well as of spectral distribution.

Further analysis would be made for the baffle optimization. With regards to the Stavroudis baffle, the sudden changes in the amount of heat power from the planet and the Sun, in particular at eclipse terminator points at aphelion and perihelion orbits, results in extreme and fast variation of temperature among the baffle structure and temperature differences within the baffle nodes could results in distortion due to thermal stress induced by temperature gradients. Afterwards the geometry of the Stavroudis baffle will be modified and this could make worse the performance of the baffle. Thermo-structural analysis should be performed to estimate the performance drop of the baffle due to deformation caused by thermal gradients. Interfacing between thermal analysis software, which uses lumped parameters methods, and finite element structural analysis software would lead to estimate the performance of the baffle. Furthermore experimental test data would give an estimation of baffle loss of efficiency due to temperature gradients and validation of mathematical models would be made.

9 REFERENCES

[1] ESA BepColombo mission web page: http://sci.esa.int/science-e/www/area/index.cfm?fareaid=30

[2] E.Flamini et al., *SIMBIO-SYS: The spectrometer and imagers integrated observatory system for the BepiColombo planetary orbiter*, Planetary and SpaceScience 58(2010), 125–143

[3] EID -A *BepiColombo*, Issue 2, Rev.1, 2009, BC-EST-RS-01140

[4] Mercury Environmental Specification (Part I), by D. Stramaccioni, ESA BC-EST-TN-00112

[5] Mercury Orbital Heat Fluxes Assessment (Worksheet version 4.0 for MPO Orbits) by D.Stramaccioni

[6] SIMBIO-SYS ISRR Thermal, Mercury Environmental Specification Complementary Information by P.Poinas, May 2007

[7] EID-C.part 6, Mercury Environmental Specification Pt.1, BepiColombo, BC-EST-RS-05055 part 6, 14th July 2008

[8] Siegel, Howell, Thermal Radiation Heat Transfer, McGraw Hill,1992

[9] Wertz, Space Mission Analysis and Design,Microcosm, 2003

[10] E.Friso, S.Debei, SIMBIO-SYS orbital thermal environment: complementary assessment, simulations and sun incidence angle evaluation, Technical Note, CISAS, University of Padova, 16 April 2010

[11] J.Vince, *Vector Analysis for Computer Graphics*, Springer-Verlag, London, 2007

[12] D.Hearn, M.P. Baker, *Computer Graphics*, 2nd Ed., Prentice Hall, Upper saddle River, NJ, 1996

[13] Didier Badouel, "*An Efficient Ray-Polygon Intersection*" in "Graphics Gems", Academic Press, San Diego, CA, 1990

[14] Simbio-Sys EID-B BepiColombo, Draft, BC-EST-RS-2523

[15] D.G.Gilmore, *Spacecraft Thermal Control Handbook, Vol. 1*, 2nd ed. , The Aerospace Press, El Segundo, CA, 2002

[16] R.D. Karam, *Satellite thermal Control for Systems Engineers*, AIAA, Reston, VA, 1998

[17] A.K. Oppenheim, *Radiation Analysis by the Network Method*, Trans. of ASME, vol.78, pp.725-735

[18] M.F.Modest, Radiative Heat Transfer, 2nd ed., Amsterdam, Academic Press, 2003

[19] J.R.Mahan, *Radiation Heat Transfer: A Statistical Approach*, J. Wiley, 2002

[20] ESATAN-TMS Thermal Engineering Manual, ITP Engines, UK, 2009

[21] ESATAN-TMS Workbench User Manual, , ITP Engines, UK, 2009

[22] G.L. Peterson, S.C. Johnson, J. Thomas, *Specular Baffles*, SPIE vol. 1753 Stray Radiation in Optical Systems II (1992)

[23] O.N.Stavroudis, L.D.Foo, *System of reflective telescope baffles*, Optical Engineering, vol. 33, no.3, pp. 675-680, 1994

[24] O.N.Stavroudis, *System of reflective telescope baffles using conic sections of revolution*, Patent Number: 5 225 931, Jul. 6, 1993

[25] Technical Note, BepiColombo, Assessment of P/L temperature results, BC-ASD-TN-00232

[26] R.Gardon, An instrument for the direct measurement of intense thermal radiation, The Review of Scientific Instruments, Vol.24, N.5, 1953